

Copyright  
by  
Benjamin Michael Goldsberry  
2019

The Dissertation Committee for Benjamin Michael Goldsberry  
certifies that this is the approved version of the following dissertation:

**Finite Element Investigation of Tunable and  
Non-reciprocal Elastic Wave Metamaterials**

Committee:

---

Michael R. Haberman, Supervisor

---

Mark F. Hamilton

---

Carolyn C. Seepersad

---

Loukas F. Kallivokas

---

Andrew N. Norris

**Finite Element Investigation of Tunable and  
Non-reciprocal Elastic Wave Metamaterials**

by

**Benjamin Michael Goldsberry**

**DISSERTATION**

Presented to the Faculty of the Graduate School of  
The University of Texas at Austin  
in Partial Fulfillment  
of the Requirements  
for the Degree of

**DOCTOR OF PHILOSOPHY**

THE UNIVERSITY OF TEXAS AT AUSTIN

May 2019

In loving memory of Evelyn Botts Wester.



# Acknowledgments

First of all, I would like to thank my advisor and mentor, Dr. Michael Haberman, for his invaluable support and guidance. I would also like to thank my wife and best friend, Candace Goldsberry, for her love, patience, and support throughout this process and for motivating me to be the best person I can be. I would also like to thank my mom and dad, as well as my mom-in-law and dad-in-law, for their constant support, love, and encouragement to continue forward in my education. A huge thank you to my brother Brian for providing me with welcome distractions, whether it was playing card games over Skype or video games.

In addition to my family, I would like to thank my friends in the UT acoustics program, both old and new, for their delightful company. Finally, I would like express my gratitude for the other members of my committee: Dr. Mark Hamilton, Dr. Carolyn Seepersad, Dr. Loukas Kallivokas, and Dr. Andrew Norris.

# **Finite Element Investigation of Tunable and Non-reciprocal Elastic Wave Metamaterials**

Publication No. \_\_\_\_\_

Benjamin Michael Goldsberry, Ph.D.  
The University of Texas at Austin, 2019

Supervisor: Michael R. Haberman

This dissertation studies elastic wave propagation in metamaterials subjected to an externally-applied static or spatiotemporally-varying pre-strain. Elastic metamaterials are media with subwavelength structure that behave as effective materials displaying atypical effective dynamic properties that are used to directly control the propagation of macroscopic waves. One major design limitation of most metamaterial structures is that the dynamic response cannot be altered once the microstructure is manufactured. However, the ability to modify, or tune, wave propagation in the metamaterial with an external pre-strain that induces geometric nonlinearity is highly desirable for numerous applications. Acoustic and elastic metamaterials with time- and space-dependent effective material properties have also recently received significant attention as a means to induce non-reciprocal wave propagation. However, the modulation of effective material properties in space and time using mechanical deformation has been unexplored. Tunable elastic metamaterials that exhibit

large effective material property changes under a varying external pre-strain are therefore strong candidates for a non-reciprocal medium.

The complex geometry present in unit cells that exhibit large geometric nonlinearity necessitates the development of a numerical technique. In this dissertation, a finite element approach is derived and implemented to study elastic wave propagation in a static pre-strained metamaterial, then generalized to include the effects of a spatiotemporally-varying pre-strain. A honeycomb structure composed of a doubly-periodic array of curved beams, known as a negative stiffness honeycomb (NSH), is analyzed as a tunable and non-reciprocal elastic metamaterial. It is shown that NSH exhibits significant tunability and a high degree of anisotropic wave behavior when a static pre-strain is imposed. This behavior can be used to guide wave energy in different directions depending on static pre-strain levels. In addition, it is shown that partial band gaps exist where only longitudinal waves propagate. The NSH therefore behaves as a meta-fluid, or pentamode metamaterial, which may be of use for applications of transformation elastodynamics such as cloaking and gradient index lens devices. A negative stiffness chain, a quasi-one-dimensional representation of NSH, is also shown as a case example of a non-reciprocal medium. It is shown in this work that this structure displays a high degree of non-reciprocity for a small amount of modulation pre-strain. The utility of the finite element approach is further demonstrated by investigating the effects of chiral geometric asymmetry to enhance the non-reciprocal behavior of elastic wave propagation in NSH.

# Table of Contents

<b>Acknowledgments</b>	<b>v</b>
<b>Abstract</b>	<b>vi</b>
<b>List of Tables</b>	<b>xi</b>
<b>List of Figures</b>	<b>xii</b>
<b>Chapter 1. Introduction</b>	<b>1</b>
1.1 Motivation . . . . .	1
1.2 Objective . . . . .	4
1.3 Overview . . . . .	6
<b>Chapter 2. Background</b>	<b>9</b>
2.1 Tunable Metamaterials . . . . .	9
2.2 Non-reciprocal Acoustics . . . . .	12
2.3 Negative Stiffness Honeycomb . . . . .	14
2.3.1 Unit Cell Selection . . . . .	18
2.3.2 Brillouin Zone . . . . .	19
<b>Chapter 3. Wave Phenomena in Modulated Continuous Meta-</b> <b>materials</b>	<b>21</b>
3.1 Introduction . . . . .	21
3.2 Space-Dependent Modulus . . . . .	24
3.2.1 Variational Statement . . . . .	26
3.2.2 Eigenvalue Accuracy . . . . .	32
3.2.3 Example: Alternating Material Layers in a Bar . . . . .	33
3.3 Time-Dependent Modulus . . . . .	36
3.3.1 Example: Hill's Equation . . . . .	40

3.4	Space- and Time-Dependent Modulus . . . . .	42
3.4.1	Example: Translating Material Layers . . . . .	45
3.4.2	Harmonic Mode Coupling . . . . .	49
3.5	Summary . . . . .	54
<b>Chapter 4. Negative Stiffness Honeycombs as Tunable Elastic Metamaterials</b>		<b>57</b>
4.1	Introduction . . . . .	57
4.2	Small-on-Large Approximation . . . . .	59
4.2.1	Deformation . . . . .	60
4.2.2	Elastic Wave Propagation . . . . .	64
4.2.2.1	Dispersion Computation . . . . .	65
4.2.2.2	Group Velocity . . . . .	68
4.3	Results . . . . .	69
4.3.1	Modal Characterization . . . . .	70
4.3.2	Dispersion . . . . .	71
4.3.3	Meta-Fluid Behavior . . . . .	77
4.4	Conclusion . . . . .	77
<b>Chapter 5. Non-reciprocal Wave Propagation in Mechanically-Modulated Continuous Elastic Metamaterials</b>		<b>82</b>
5.1	Introduction . . . . .	82
5.2	Theory . . . . .	83
5.2.1	Small-On-Large Theory Revisited . . . . .	84
5.2.2	Applied Deformation (Large Wave) . . . . .	88
5.2.3	Elastic Wave Propagation (Small Wave) . . . . .	90
5.3	Numerical Implementation . . . . .	92
5.4	Results . . . . .	95
5.4.1	Numerical Benchmark . . . . .	96
5.4.2	Negative Stiffness Chain . . . . .	100
5.4.3	Geometric Asymmetry . . . . .	108
5.5	Conclusion . . . . .	111

<b>Chapter 6. Conclusion</b>	<b>112</b>
6.1 Summary and Contributions . . . . .	112
6.2 Future Work . . . . .	117
<b>Bibliography</b>	<b>119</b>

## List of Tables

4.1	Geometric parameter values depicted in Fig. 2.4. All values are in mm. . . . .	69
4.2	Material properties of NSH . . . . .	70
5.1	Geometric parameter values depicted in Fig. 5.1. All numerical values have units of mm. . . . .	100

# List of Figures

2.1	Example tunable metamaterials in the literature. (a) Beam with periodic shunted piezoelectric patches. Adapted from [52]. (b) Acoustic membrane metamaterial with active electromagnets. Adapted from [53]. (c) Resonating units embedded in soft, deformable elastomeric matrix. Adapted from [27]. . . . .	10
2.2	The Rayleigh reciprocity theorem states that in a linear-time-invariant medium, the acoustic signal recorded at point B emitted from a source at point A (a) is identical in both magnitude and phase as the acoustic signal recorded at point A emitted from a source at point B (b). This is true even in a heterogeneous and lossy medium. . . . .	12
2.3	Negative stiffness honeycomb (NSH) metamaterial with the fundamental unit cell shaded and direct lattice vectors $\mathbf{a}_1, \mathbf{a}_2$ . . .	14
2.4	Geometric parameters of NSH. The region shaded in blue indicates the unit cell. . . . .	15
2.5	(a) Stored internal energy of the pre-curved beams as a function of external pre-strain. (b) Force response of the pre-curved beams and the resulting deformation of the beams before and after the critical point of buckling. The critical point where the stiffness changes from positive to negative is the stationary point on the force-strain curve, and the inflection point on the energy-strain curve. . . . .	16
2.6	The first Brillouin zone, defined with basis vectors $\mathbf{b}_1, \mathbf{b}_2$ . The irreducible Brillouin zone is traced in black. . . . .	19
3.1	Second order finite element shape functions defined in a mesh element. . . . .	30
3.2	(a) Finite element computation of the dispersion relation for propagating longitudinal waves in a bar with periodic alternating layers. Since the dispersion relation is periodic, the complete dispersion relation can be obtained by restricting $k$ to lie within the first Brillouin zone (black dashed lines). (b) Comparison of the finite element computation in the first Brillouin zone from (a) with the exact dispersion relation (orange lines), Eq. (3.41). . . . .	34



3.3	(a) Comparison of the frequency-wavenumber spectrum of Hill's equation using Eq. (3.61) (open circles) with the exact dispersion solution, Eq. (3.66). (b) Dispersion relation from (a) weighted by the magnitude of the fundamental plane wave component in decibels, $20 \log_{10}(\ \hat{\Phi}_0\ /\ \hat{\Phi}\ )$ . . . . .	40
3.4	(a) Finite element computation of the dispersion relation for the case of translating material layers with modulation speed $c_m = 0.159$ ( $\omega_m = 1$ ). Due to the bias in the $+x$ direction, the dispersion curves are not symmetric about $k = 0$ , i.e. reciprocity is broken. (b) The dispersion curves shown in (a) but with each point colored by the magnitude of the fundamental component in decibels, $20 \log_{10}(\ \mathbf{u}^0\ /\ \mathbf{u}\ )$ . The dashed line is the first branch of the exact dispersion relation for this case, which is obtained using Eq. (3.83) and Eq. (3.41). . . . .	46
3.5	Dispersion relations for the translating layers case as a function of the modulation speed $c_m$ . (a) No translation, $c_m = 0$ , (b) $c_m = 0.05$ , (c) $c_m = 0.1$ , (d) $c_m = 0.3$ . . . . .	48
3.6	(a) Approximate dispersion relation using Eq. (3.97) (open circles) compared to Fig. 3.4(a). (b) Zoom-in plot of the lowest directional bandgap. The dashed line represents the solution $\bar{\omega}_0$ from Eq. (3.89). . . . .	52
3.7	Ratio of the amplitude $B$ of mode $\mathbf{u}^1$ over amplitude $A$ of mode $\mathbf{u}^0$ at the lowest directional band gap. The solid line represents the direct QEP solution, and circles are from Eq. (3.98). . . .	53
4.1	Negative stiffness honeycomb (NSH) metamaterial with the fundamental unit cell shaded and direct lattice vectors $\mathbf{a}_1, \mathbf{a}_2$ (reproduced from Fig. 2.3 for convenience). . . . .	58
4.2	Computational domain, $\Omega$ , of NSH. The boundary pairs $(\Gamma_A^+, \Gamma_A^-)$ , $(\Gamma_B^+, \Gamma_B^-)$ , $(\Gamma_C^+, \Gamma_C^-)$ are the locations where periodic boundary conditions are applied to the computational domain. . . .	62
4.3	Deformation of the pre-strained lattice for $\beta = 0.05$ . . . . .	63
4.4	Total potential energy within the unit cell as a function of the pre-strain. The points represent where the wave propagation is studied and reported in Sec. 4.3. . . . .	66
4.5	Mode dispersion in the irreducible Brillouin zone for: (a) $\beta = 0$ (undeformed configuration), (b) $\beta = 0.0101$ , (c) $\beta = 0.0207$ , (d) $\beta = 0.0252$ . The shaded regions indicate frequency ranges where only unimodal longitudinal wave motion is permitted in the lattice. . . . .	72

4.6	The first Brillouin zone, defined with basis vectors $\mathbf{b}_1, \mathbf{b}_2$ . The irreducible Brillouin zone is traced in black (Reproduced from Fig. 2.6 for convenience.) . . . . .	73
4.7	Ratio of the phase speed over the phase speed of the undeformed configuration at 200 Hz for longitudinal and transverse waves as a function of the external pre-strain $\beta$ in the: (a) $X_1$ direction, (b) $X_2$ direction. . . . .	74
4.8	Slowness curves for 1100 Hz at a pre-strain of: (a) $\beta = 0$ (undeformed configuration), (b) $\beta = 0.0101$ , (c) $\beta = 0.0207$ . . . .	80
4.9	Group velocity at 1100 Hz. (a) Group velocity of the longitudinal mode for $\beta = 0$ and $\beta = 0.0101$ . The color scheme differs from the previous figures and serves to denote the two pre-strain solutions. The triangle symbol, which represents the longitudinal mode, is still preserved. (b) Group velocity of the transverse and higher order modes for $\beta = 0$ . (c) Group velocity of the transverse and higher order modes for $\beta = 0.0101$ . . . .	81
5.1	Negative stiffness element with geometric parameters. . . . .	83
5.2	(a) Supercell computational domain with displacement boundaries $\Gamma_u$ and periodic boundary pairs $(\Gamma^+, \Gamma^-)$ . (b) Nonlinear deformation of the negative stiffness chain due to the external pre-strain $\beta(x, t)$ with parameters $\beta_0 = 0.01$ and $\Delta\beta = 0.3\beta_0$ . The external pre-strain is applied as displacement boundary conditions on the faces depicted by the arrows. The applied displacement in the $y$ direction, $u_y(x, t)$ , are composed of a static displacement term denoted by the dashed line whose value is $\beta_0 L_y$ , and an oscillating component depicted by the sine wave with amplitude $\Delta\beta L_y$ (not drawn to scale). . . . .	85
5.3	(a) Computational mesh. (b) The resulting time dependence and FFT solution of the $L_{1100}$ component from a prescribed pre-strain at the node marked in (a). Note that the time solution contains more than one Fourier component. . . . .	92
5.4	Geometry of the thin plate Kirchhoff benchmark system. . . .	95
5.5	(a) Frequency-wavenumber spectrum of the transverse wave in a thin Kirchhoff plate. Open circles are the results from Trainiti et al., and filled circles are results obtained from the finite element model. (b) The finite element results presented in (a) but with each point colored by its normalized magnitude of the fundamental component in decibels, $20 \log_{10}(\ \hat{\mathbf{u}}^0\ /\ \mathbf{U}\ )$ . . . .	97

5.6	(a) Frequency-wavenumber spectrum of the negative stiffness chain with a static pre-strain of $\beta_0 = 0.01$ . The transverse mode is highlighted. (b) The transverse mode spectrum with the vertical lines and numerals indicating the supercell Brillouin zone number. The mode shape is shown in the inset image. . .	99
5.7	Frequency-wavenumber spectra of the transverse mode of the negative stiffness chain. (a) Comparison of spatial modulation (open circles) and static pre-strain only (diamonds; same data as in Fig. 5(b), but folded at the Brillouin zone boundaries). (b) Comparison of spatial modulation (open circles; same as in (a)) and spatiotemporal modulation (filled circles), where the color scale is defined in the same way as Fig. 5.5(b). . . . .	101
5.8	Comparison of the approximate dispersion relation, Eq. (3.97), (open diamonds) with the frequency-wavenumber spectrum of the transverse mode from Fig. 5.7. The red dashed line represents the reference eigenvalue branch, which is the solution to Eq. (3.89), and the orange dashed line represents the coupling branch. The two modes exhibit strong coupling at the wavenumber where the two curves are separated by $f_m$ . . . . .	103
5.9	(a) Dispersion of the negative stiffness chain with a static pre-strain of $\beta_0 = 0.01$ . A region that contains the longitudinal and a higher-order transverse mode is highlighted. (b) Zoom-in plot of the shaded region in (a), where the longitudinal and transverse modes are identified using the modal filter technique discussed in Sec. 4.3.1. The respective mode shapes are shown in the inset image. . . . .	104
5.10	Frequency-wavenumber spectrum of the region highlighted in Fig. 5.9(a). The dispersion curves of the transverse mode (blue open circles) and the longitudinal mode (red open circles) for a spatial modulation of the pre-strain are also plotted. . . . .	105
5.11	Frequency-wavenumber spectrum of the region highlighted in Fig. 5.9(a) for a modulation speed of $c_m = 0.04c_s$ . The highlighted regions and spatial-only modulation results are identical to Fig. 5.10. . . . .	107
5.12	Chiral configuration of the negative stiffness element with a beam thickness change of 10% (geometry is exaggerated for visualization purposes). . . . .	108
5.13	Transverse and longitudinal modes of the chiral negative stiffness chain with a static pre-strain of $\beta = 0.01$ . . . . .	109

5.14	(a) Frequency-wavenumber spectrum of the chiral negative stiffness chain for a modulation speed of $c_m = 0.04c_s$ . The dispersion curves of the transverse mode (blue open circles) and longitudinal mode (red open circles) for the space-only modulation of the pre-strain are also shown. (b) Zoom-in of the highlighted region in (a). The longitudinal mode directional bandgap is highlighted. . . . .	110
------	--	-----

# Chapter 1

## Introduction

### 1.1 Motivation

Mechanical metamaterials have received significant attention in a wide range of fields in science and engineering, including acoustics, elastodynamics, and materials science as a means to directly control the propagation of mechanical waves through a synthetic elastic medium. These materials are composed of an engineered microstructure which, in the limit of long wavelengths compared to length the microstructure, exhibit extraordinary effective dynamic behavior. The advancement of electromagnetic metamaterials and the first experimental demonstration of an acoustic metamaterial in 2000 [1] prompted a flood of research, which has shown that atypical effective material properties can be observed that do not exist in naturally-occurring materials, such as negative mass density [1], negative stiffness [2], or a combination of the two [3]. These unique properties have enabled, or made plausible, applications that were previously inaccessible to the acoustics community, such as negative refraction [4–6], superlensing beyond the diffraction limit [7–9], cloaking by bending propagating waves around an object [10–12], extraordinary absorption [13], and arbitrary control of the phase of waves reflected or transmitted from a surface [14–17]. Early research on metamaterials often

relied on sub-wavelength resonance structures which limits their usefulness to narrow bands of frequency and whose performance can be degraded by the presence of absorption [18–21]. Metamaterials that do not rely on resonances but lead to extreme effective material properties are therefore of significant interest for the future development of acoustic metamaterials and their use in practical applications. One particular application of interest are pentamode metamaterials, which are stiff structures with a small static and dynamic shear modulus. These metamaterials support only longitudinal wave propagation in a wide frequency band and can therefore be used for impedance matching between a fluid and solid material in acoustic cloaking and lensing applications while supporting a static load [22, 23].

One limitation of most metamaterial structures studied to date is that their dynamic material properties cannot be altered after construction, limiting the range of applications. However, there are many cases where the ability to change, or tune, dynamic effective material properties is highly desirable. For example, passive acoustic lenses cannot dynamically steer their focus and thus their use is more limited than electronically-steered multi-element arrays. Therefore, the key challenge in useful material property tunability is to design microstructures that enable sufficiently large changes in macroscopic response upon application of an external stimulus. Previous work on the topic of material property tuning has primarily focused on the use of piezoelectric elements controlled by electronic signals [24, 25]. However, it is notable that the ability to change the material properties of a medium is inherently tied to its

nonlinearity [21]. Namely, the acoustic or elastic waves that propagate in the medium will do so at a speed that depends on stiffness and density variations from the prescribed deformation. Microstructures that exhibit elastic buckling from geometric nonlinearity caused by an external pre-stain are investigated in this work as a means to introduce large changes in the effective stiffness, and thus the effective phase speed, of the medium [26–28].

Recently, research on the topic of breaking acoustic reciprocity has gained attention as a means for greater control over acoustic and elastic waves. One way to accomplish this is by modulating the material properties of a medium in time and space, which breaks parity-time symmetry and thus enables non-reciprocal acoustic and elastic wave phenomena [29–32]. By breaking acoustic reciprocity, new applications for direction-specific wave control and manipulation can be explored, including the possibility of one-way sound propagation or the construction of devices that can simultaneously transmit and receive acoustic signals in different directions [18, 30, 33, 34]. These direction-dependent acoustic devices have the potential to aid in numerous acoustical applications, such as energy harvesting, signal processing, vibration isolation, and acoustic communication. Previous research has investigated using electromagnetic effects, such as piezoelectric materials [35–37], magnetorheological elastomers [38], and phononic crystals containing electromagnets [39] to modulate the material properties in space and time. However, the manipulation of the effective material properties in space and time via mechanical deformation has been unexplored. Tunable metamaterials, which exhibit large effective

dynamic property changes under a varying external pre-strain are therefore strong candidates for the creation of nonreciprocal acoustic and elastic materials and are the subject of this work.

## 1.2 Objective

The primary goal of this dissertation is to study linear elastic wave propagation in a metamaterial undergoing external static and spatiotemporally-modulated pre-strain. The research in this dissertation is motivated by the following questions:

1. How are the bandgaps and anisotropic properties of the transverse and longitudinal waves in a metamaterial with strong geometric nonlinearity affected by an externally-applied static pre-strain?
2. What non-reciprocal effects are observed when the external pre-strain imposed on a metamaterial with strong geometric nonlinearity is modulated in space and time?

Unit cells that display the necessary amount geometric nonlinearity are typically composed of complex geometry, which prevents the use of analytical methods to study the above questions. This necessarily motivates the development of a computational technique. The finite element method (FEM) is a well-known numerical procedure that can accurately solve the equations of motion to sufficient numerical precision on arbitrary domains [40]. Recently, FEM has become a useful method to model wave propagation in pre-strained



structures [26, 27]. The adaptation of FEM to study elastic wave propagation in a metamaterial usually relies on Bloch wave theory applied on a unit cell, which numerically results in a eigenvalue problem that is then used to generate the frequency-wavenumber spectrum and the unit cell mode shapes (discussed in Chapter 3). The identification of longitudinal and transverse waves in these types of metamaterials can be hard to identify from a frequency-wavenumber spectrum, as additional modes appear in the spectrum due to the presence of extra degrees of motion in a geometrically-complex metamaterial, and modes can often exchange their shapes to different branches of the dispersion spectrum through mode veering and locking [41]. Consequently, the determination of bandgaps and the anisotropic behavior for each mode can be challenging. Therefore, the first objective of this work is to extend the finite element approach from previous works [26, 27, 42, 43] with a modal filter technique to easily identify each mode in a frequency-wavenumber spectrum, which will aid in finding modal bandgaps, as well as to compute the group velocity in all propagation directions to study the anisotropic properties for each mode of interest.

The presence of spatiotemporal modulation of the material properties introduces an additional complexity to the modeling of non-reciprocal wave propagation, as the space and time dependence of the effective material properties must be properly accounted for. As a consequence, current research has only investigated non-reciprocal wave propagation in simple mass-spring chains and one-dimensional beam structures [31, 32, 44, 45]. The second ob-

jective of this dissertation is therefore to extend the finite element approach for the static pre-strain case to accurately model time-space variations of the effective material properties from a spatiotemporally-varying pre-strain.

One concept key to the present work is the modeling of nonlinear, purely mechanical deformation, which effectively perturbs the linearized stiffness and/or mass properties of small disturbances propagating in superposition (the “small” wave). This “small-on-large” propagation behavior has been of interest for ultrasonic non-destructive testing [46, 47] and mechanical metamaterials [26, 28, 44, 48–51]. In this work, the “small-on-large” approximation is used to decompose the calculation of the total displacement in a metamaterial into two sequential steps: a nonlinear static finite element model that captures the effects of the external pre-strain, and an elastic wave finite element model that is linearized about the large deformation. In the case of non-reciprocal wave propagation, the nonlinear finite element model captures the deformation due to a spatiotemporally-varying pre-strain, which resembles a large periodic traveling wave. In this case, care is taken to not violate the assumptions of the “small-on-large” approximation by ensuring that the modulation speed is much slower than the intrinsic longitudinal and transverse wave speeds of the medium.

### 1.3 Overview

This dissertation is organized as follows. Chapter 2 provides a brief background on tunable and non-reciprocal metamaterials. In addition, the

negative stiffness honeycomb is introduced, which is the candidate metamaterial that is investigated as a tunable metamaterial in Chapter 4 and as a non-reciprocal metamaterial in Chapter 5. Chapter 3 provides an overview of wave propagation in periodically-modulated media. Solutions are restricted to one dimension in space to illustrate the computational methods and relevant wave phenomena. Three different material property modulations are considered: space-only, time-only, and space-time modulation. The weak forms, which is the starting point for the finite element method, are derived for each case and compared with particular modulations that have well-known solutions. In Chapter 4, the small-on-large approximation is used to study the elastic wave propagation in a pre-strained negative stiffness honeycomb. The finite element method presented in Chapter 3 is generalized to the two-dimensional elastodynamic equations and utilized to solve for the dispersion behavior of propagating modes as a function of the Bloch wavenumber. The anisotropic wave properties of the lattice is also studied by solving the finite element method for Bloch wavenumbers in all directions. It is shown that the lattice behaves as a meta-fluid in a broad frequency range, and that the anisotropic properties can be tuned by varying the pre-strain amount. In Chapter 5, the small-on-large approximation is revisited for pre-strains that vary in space and time. The spatiotemporal finite element approach introduced in Chapter 3 is then generalized to the elastodynamic case. It is demonstrated that the application of a spatiotemporally-varying pre-strain induces directional bandgaps for the transverse and longitudinal modes. The effect of chiral geometric asymmetry

is also investigated as a means to increase the degree of non-reciprocity. Finally, conclusions and suggestions for future research are provided in Chapter 6.

# Chapter 2

## Background

The scope of research in this dissertation encompasses elastic wave propagation in a metamaterial with tunable elastic stiffness accessed via geometric nonlinearity. That metamaterial is studied first as a medium whose properties can be tuned to vary elastic wave speeds either uniformly or through spatio-temporal modulation to generate non-reciprocal propagation. In order to unify these concepts, a negative stiffness honeycomb (NSH) is used as a representative metamaterial. This chapter introduces NSH and the relevant background pertaining to tunable metamaterials and non-reciprocal acoustics.

### 2.1 Tunable Metamaterials

The limitations of passive acoustic and elastic wave metamaterials, such as fixed narrow frequency bands of operation, prompts the study of active tunable metamaterials with enhanced performance and adjustable operating frequencies. Figure 2.1 showcases a few examples of tunable metamaterials in the literature, which includes a beam whose effective properties are changed with periodic piezoelectric patches [52], an acoustic waveguide with side-holes and membranes whose stiffness can be controlled by electromagnets, and a

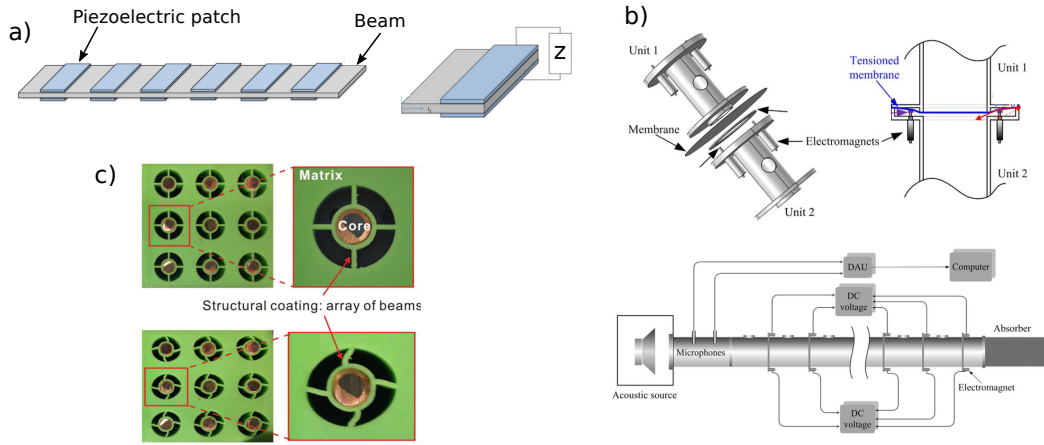


Figure 2.1: Example tunable metamaterials in the literature. (a) Beam with periodic shunted piezoelectric patches. Adapted from [52]. (b) Acoustic membrane metamaterial with active electromagnets. Adapted from [53]. (c) Resonating units embedded in soft, deformable elastomeric matrix. Adapted from [27].

metamaterial with resonating units in a soft elastomeric matrix that exhibits buckling from geometric nonlinearity [27], which is the method of interest to this work. The dynamic behavior of pre-strained periodic metamaterials has been well studied for unit cells with a buckling instability [54]. Weak and strong non-linear effects have been investigated in a one-dimensional lattice of bistable elastic elements [55, 56], and the existence of solitary waves has been theoretically and numerically verified for these types of lattices [57]. In the linear limit, the dispersion behavior of propagating modes is altered upon application of an external pre-strain that is sufficient to alter the geometry at the microscale [48, 58, 59]. In practice, an external pre-strain is applied via controlled displacements of the boundaries of the metamaterial. The large displacements of the boundaries cause the unit cells to undergo a large, geo-

metrically nonlinear deformation.

The large deformation causes two effects: *i*) the unit cell geometry changes configurations associated with geometric nonlinearity, and *ii*) the internal stored energy of the unit cell increases relative to the undeformed configuration from material nonlinearity, both of which influence the dispersion behavior of linear elastic waves propagating in the pre-strained medium [60]. The increase of the internal stored energy from material nonlinearity influences the effective macroscopic stiffness of the metamaterial. In other words, a strained lattice in the deformed configuration and an un-strained lattice with the same geometry as the deformed configuration will have different effective stiffnesses and therefore exhibit different dispersion behavior [58]. The effect of the change in the internal geometry from geometric nonlinearity has a large effect on the locations and widths of bandgaps [60]. Lattices with a macroscopic buckling instability can take on a new periodicity in a post-buckling configuration, which can switch bandgaps on and off [27, 42, 61]. In addition to tuning bandgap behavior, the anisotropy of transverse and longitudinal waves in a two-dimensional lattice can be varied upon application of an external pre-strain [48, 58, 60]. This has applications in applying transformation acoustics to cloak an object, which requires layers of metamaterials with varying anisotropy [62].

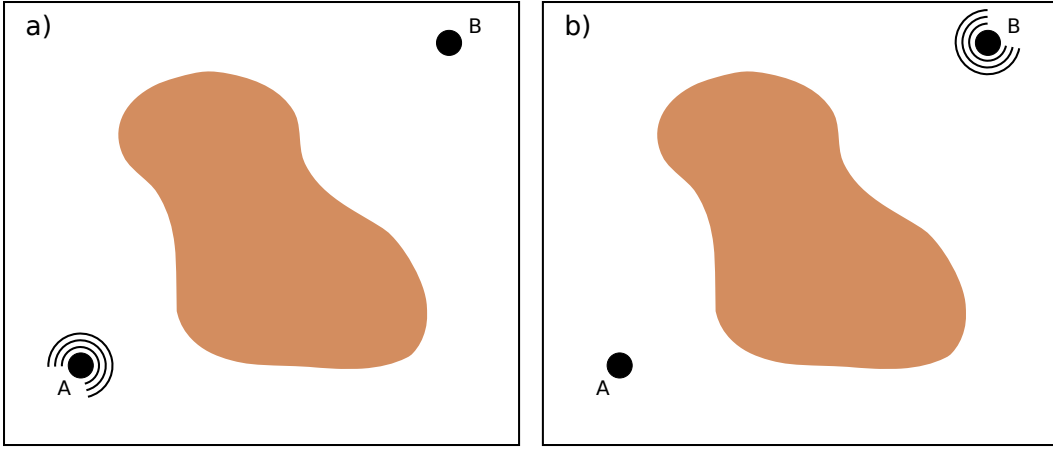


Figure 2.2: The Rayleigh reciprocity theorem states that in a linear-time-invariant medium, the acoustic signal recorded at point B emitted from a source at point A (a) is identical in both magnitude and phase as the acoustic signal recorded at point A emitted from a source at point B (b). This is true even in a heterogeneous and lossy medium.

## 2.2 Non-reciprocal Acoustics

Acoustic reciprocity is an important fundamental property that details the characteristics of wave propagation between two points. Namely, in a linear-time-invariant (LTI) medium, the propagation of elastic or acoustic waves from source to receiver will be identical if the source and receiver are interchanged [30, 63, 64]. This concept is shown schematically in Fig. 2.2. Acoustic reciprocity was first documented by Helmholtz [65] and later by Lamb [66]; but it is credited to Rayleigh for formulating the general conditions of reciprocity in his works [63]. Acoustic reciprocity holds even if the medium is heterogeneous and/or is lossy [33].

The Onsager-Casimir principle provides the symmetry conditions on



the transmission of acoustic waves between two points. This fundamental principle of physics states that  $t_{AB}(\omega, \eta, \mathbf{B}) = t_{BA}(\omega, \eta, -\mathbf{B})$ , where  $t_{AB}$  and  $t_{BA}$  are the (complex-valued) transmission coefficients for waves propagating from point A to B and B to A in the medium, respectively,  $\omega$  is the frequency,  $\eta$  is a macroscopic loss factor, and  $\mathbf{B}$  is a set of material parameters that is oddly symmetric on time reversal [18, 33]. The set  $B$  represents a generalized form of “momentum” bias, such as fluid flow [18, 33]. Reciprocity therefore only holds when  $\mathbf{B} = 0$ . The use of an external bias ( $\mathbf{B} \neq 0$ ) that is oddly symmetric on time reversal to break reciprocity has been achieved in piezophononic media [67], moving media [30, 68, 69], and gyroscopic phononic crystals [70, 71].

Other means to achieve non-reciprocity is to break the assumptions of the Onsager-Casimir principle. This includes the presence of nonlinearity, which has been used to create one-way sound propagation via harmonic generation [72–74]. The other mechanism, which is central to this work, is to break to assumption of time-invariance through modulation of the material properties in time and space [31, 45, 75–79]. Effective mechanical properties have been manipulated in past works using electromagnetic effects, for example in piezoelectric materials [35–37], magnetorheological elastomers [38], and phononic crystals containing electromagnets [39]. The generation of non-reciprocity via mechanical deformation has been studied in a one-dimensional mass-spring chain [44], but has not been investigated for continuous elastic structures. This work therefore contributes to this field by providing a finite element framework to model non-reciprocal wave propagation in a con-

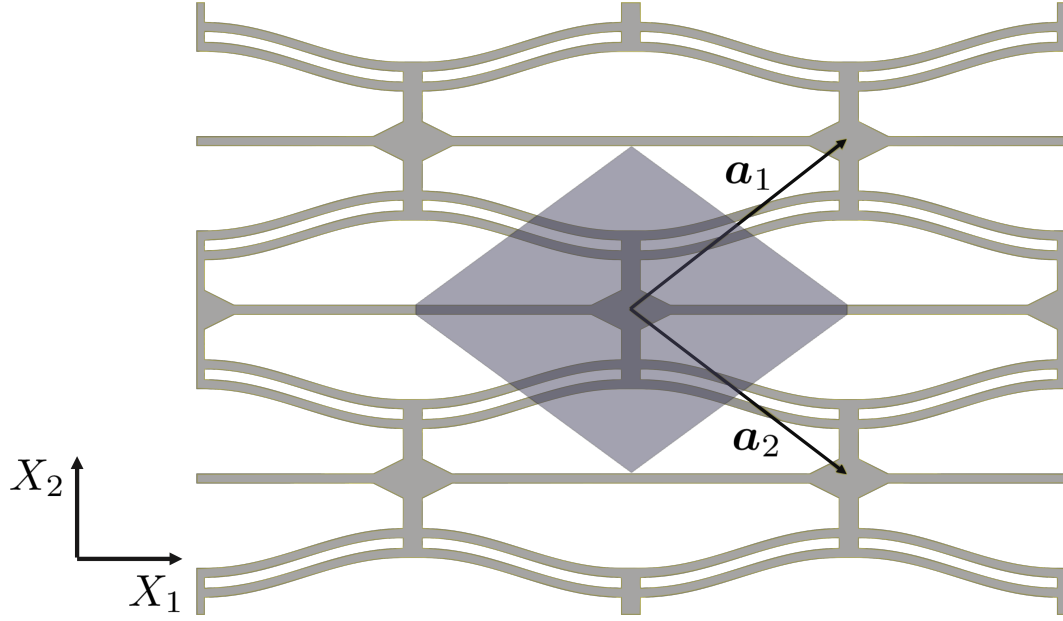


Figure 2.3: Negative stiffness honeycomb (NSH) metamaterial with the fundamental unit cell shaded and direct lattice vectors  $\mathbf{a}_1, \mathbf{a}_2$ .

tinuous elastic structure and a tunable metamaterial that can be used as a non-reciprocal medium.

## 2.3 Negative Stiffness Honeycomb

The metamaterial unit cell under investigation is the modified version of the honeycomb design in Correa *et al.* [80]. Like regular honeycombs, NSH consist of an ordered configuration of prismatic cells. NSH differ from conventional honeycomb structures in that NSH cells have been designed to permit large, recoverable deformation and thus enable the absorption of energy impacts while returning to the original shape upon removal of the mechanical

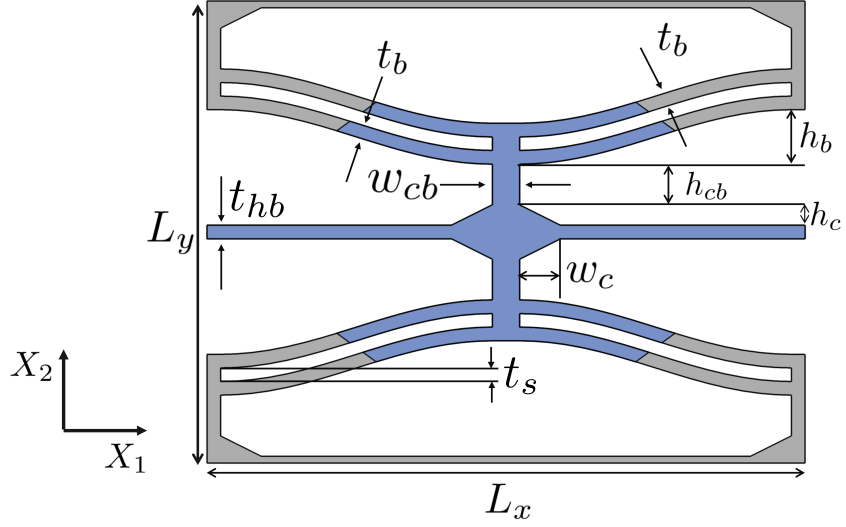


Figure 2.4: Geometric parameters of NSH. The region shaded in blue indicates the unit cell.

load. The recoverable deformation is the result of the unit cell geometry, which consists of curved beams that exhibit force-displacement behavior similar to that of bistable or snap-through structures [80–82]. Negative stiffness honeycombs are structured to generate a non-monotonic force-displacement relationship when subjected to externally applied deformations. Specifically, these materials require a decreasing level of force when one imposes an increase in the displacement field [80, 82]. This non-intuitive response is the result of structural instabilities at the unit cell level that result from geometric nonlinearity associated with large deflections of the constituent elastic elements in the structure.

A unit cell of the lattice under consideration is shown in Fig. 2.3, and the geometric parameters are shown in Fig. 2.4. The pre-curved beams are fab-

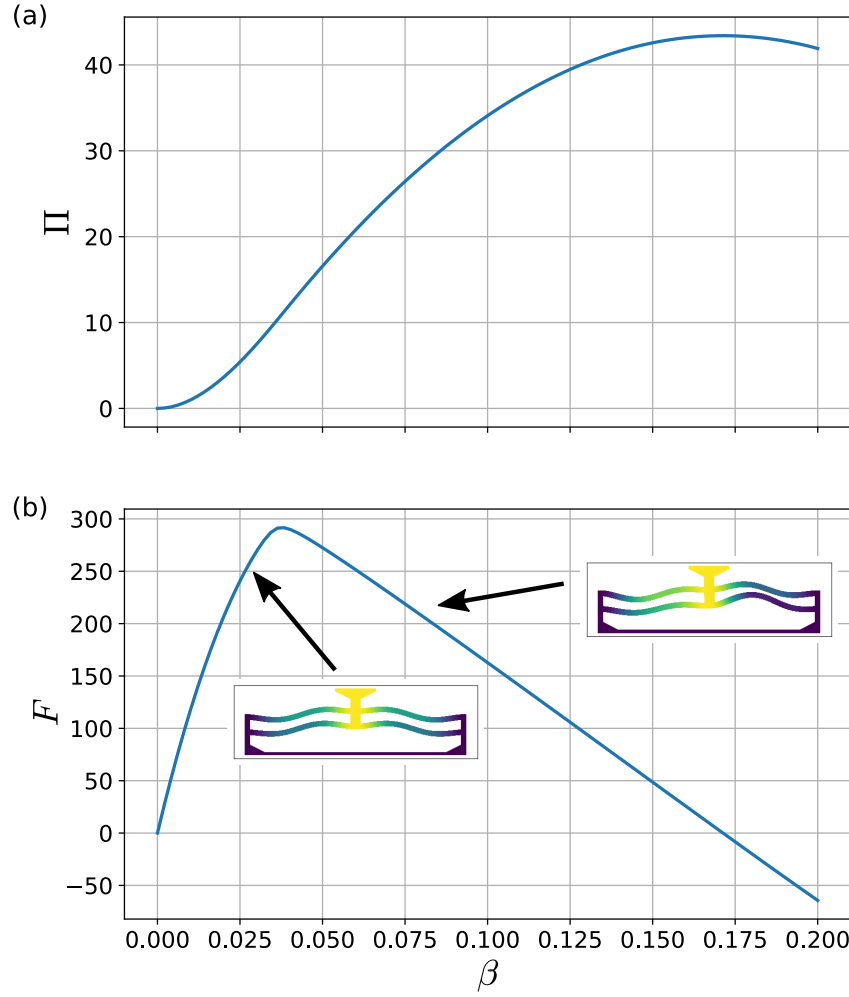


Figure 2.5: (a) Stored internal energy of the pre-curved beams as a function of external pre-strain. (b) Force response of the pre-curved beams and the resulting deformation of the beams before and after the critical point of buckling. The critical point where the stiffness changes from positive to negative is the stationary point on the force-strain curve, and the inflection point on the energy-strain curve.

ricated in the shape of a sinusoid with a spatial period  $L_x$  and an amplitude  $h_b$ , which mimics the shape of a beam buckled into its first Euler buckling mode [83]. The double pre-curved beam design as well as the vertical and horizontal elastic elements have been designed to mechanically constrain the system such that the system buckles into a pseudo-third buckling mode, which resembles a sinusoid with twice the spatial periodicity along the  $X_1$ -direction (see deformation plot in Fig. 2.5(b)), when a specified external uni-axial pre-strain in the  $X_2$  direction is attained [80]. In general, the elastic response of the NSH can be tuned through a few simple geometric parameters of the lattice, as shown in Fig. 2.4. The stored internal energy  $\Pi$  of the pre-curved beams as a function of an external pre-strain  $\beta$  is plotted in Fig. 2.5(a). For small pre-strains,  $\Pi$  is locally quadratic. At the instability of the beams, the energy curve has an inflection point and changes curvature past the instability point. The resulting normalized force is plotted in Fig. 2.5(b), and is the derivative of the energy function, Fig. 2.5(a). The beams are initially stiff, and approaches zero stiffness at the buckling instability. Beyond the instability point is a region of negative stiffness. In this work, only the range of pre-strains before the instability point are considered. The ratio  $Q = h_b/t_b$  most directly affects the elastic stored energy in the unit cell; large ratios will yield a more pronounced snapping behavior [83]. In this work, a ratio of 4 is chosen to increase tunability, while it is noted that the unit cell will be bistable when  $Q$  is greater than 2.41 [83]. Previous work has made use of the tunability of the lattice via these geometric features to produce NSH that isolate vibration and mechan-

ical impacts [81]. However, the strongly nonlinear elastic behavior of NSH materials suggest that linear wave propagation in these materials has a strong dependence on an externally imposed pre-strain. Further, because the large deformations are associated with buckling phenomena, NSH can be fabricated from high-stiffness non-lossy materials without loss of the types of tunability described in this work. This is a significant difference from most other tunable metamaterials in the literature, which make use of soft materials like silicon rubber, and consequently are very lossy [26, 27, 42]. NSH are therefore of interest as candidate structures for elastic metamaterials that can control wave propagation by tailoring the dispersive nature of wave propagation through uniaxial pre-strain.

### 2.3.1 Unit Cell Selection

The NSH shown in Fig. 2.3 can be geometrically decomposed into a fundamental unit cell with a set of basis vectors in which the whole lattice can be reconstructed through translations of this fundamental unit cell along the basis vectors [84]. The unit cell chosen for this work is the shaded region in Fig. 2.3 and Fig. 2.4, which is spanned by the direct lattice vectors  $\mathbf{a}_1, \mathbf{a}_2$ . Any spatially-varying function in these materials must also obey the unit cell periodicity

$$f(\mathbf{X} + \mathbf{R}) = f(\mathbf{X}), \quad (2.1)$$

where,

$$\mathbf{R} = p_1 \mathbf{a}_1 + p_2 \mathbf{a}_2, \quad (2.2)$$

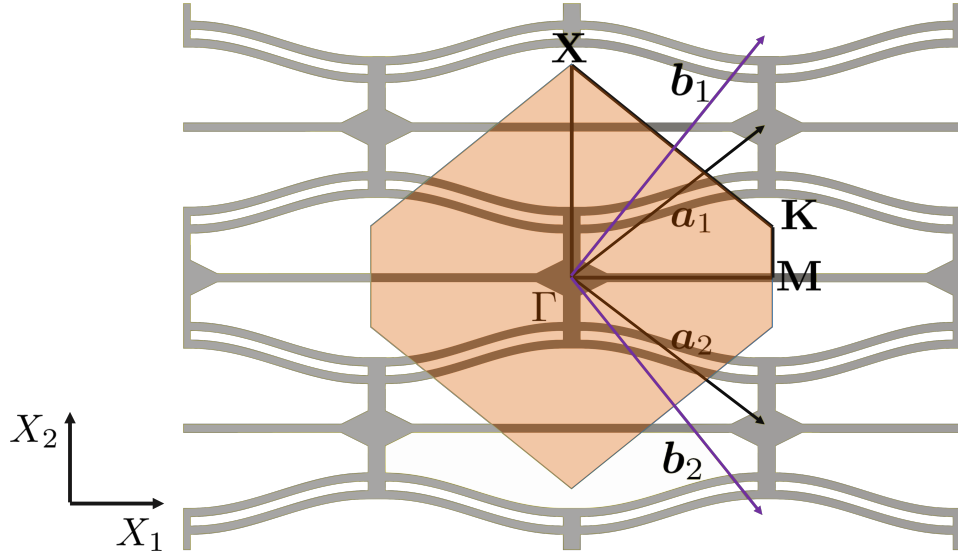


Figure 2.6: The first Brillouin zone, defined with basis vectors  $\mathbf{b}_1, \mathbf{b}_2$ . The irreducible Brillouin zone is traced in black.

and  $p_1, p_2$  are integers that represent the unit cell location relative to the fundamental unit cell located at the position defined by  $p_1, p_2 = 0$ . In Cartesian coordinates, the direct lattice vectors are

$$\mathbf{a}_1 = \frac{L_x}{2}\mathbf{e}_1 + \frac{L_y}{2}\mathbf{e}_2, \quad (2.3)$$

$$\mathbf{a}_2 = \frac{L_x}{2}\mathbf{e}_1 - \frac{L_y}{2}\mathbf{e}_2. \quad (2.4)$$

### 2.3.2 Brillouin Zone

For periodic media, all unique propagating modes lie within the first Brillouin zone [85]. Therefore the values of the Bloch wave vector  $\mathbf{K}$  are restricted to this region. The basis vectors in the reciprocal (wavenumber)

space are obtained through the following relationships

$$\mathbf{b}_1 = 2\pi \frac{\mathbf{a}_2 \times \mathbf{z}}{\|\mathbf{z}\|^2}, \quad (2.5)$$

$$\mathbf{b}_2 = 2\pi \frac{\mathbf{z} \times \mathbf{a}_1}{\|\mathbf{z}\|^2}, \quad (2.6)$$

where  $\mathbf{z} = \mathbf{a}_1 \times \mathbf{a}_2$ . From Eqns. (2.3)-(2.4), the reciprocal basis vectors are

$$\mathbf{b}_1 = \frac{2\pi}{L_x} \mathbf{e}_1 + \frac{2\pi}{L_y} \mathbf{e}_2, \quad (2.7)$$

$$\mathbf{b}_2 = \frac{2\pi}{L_x} \mathbf{e}_1 - \frac{2\pi}{L_y} \mathbf{e}_2. \quad (2.8)$$

The first Brillouin zone is then found graphically by creating a Wigner-Seitz cell with the above basis vectors, which is constructed as follows [84]:

1. Select a lattice point in the reciprocal lattice and connect it to neighboring points.
2. Draw the perpendicular bisectors of these lines. The area enclosed by these lines is the first Brillouin zone.

Figure 2.6 shows the Brillouin zone overlaid on the NSH. Due to symmetry about the  $X_1$  and  $X_2$  axes,  $\mathbf{K}$  can be reduced to vectors that lie within the irreducible Brillouin zone, traced in black. It is assumed throughout this dissertation that the Brillouin zone is constant for all deformation configurations of the lattice, which is consistent with other studies on the dispersion computation of tunable metamaterials [26, 42].



# Chapter 3

## Wave Phenomena in Modulated Continuous Metamaterials

### 3.1 Introduction

The main focus of the present work is to develop a computational approach to study elastic wave propagation in a medium whose material properties are either modulated in space or time independently or simultaneously in space and time. Modeling waves in a modulated medium presents a challenge due to the unique wave phenomena present since one commonly assumes conditions of spatial homogeneity or time-invariance in the medium of interest. In order to study wave propagation in a modulated medium, it is first important and informative to identify and characterize the wave phenomena present in a medium with space-only or time-only modulation, and determine how these concepts generalize to a spatiotemporally-modulated medium. Furthermore, the solution techniques used to solve the space-only and time-only modulation can be leveraged to handle the more general case, which is the ultimate interest of the present work. This chapter therefore endeavors to introduce and study these concepts for the one-dimensional case, which will be later applied to the general three-dimensional elastodynamic equations.

The equation of interest in this chapter is the one-dimensional wave equation of the form

$$\frac{\partial}{\partial x} \left( a(x, t) \frac{\partial u}{\partial x} \right) - b \frac{\partial^2 u}{\partial t^2} = 0, \quad -\infty < x < \infty, \quad t \geq 0, \quad (3.1)$$

which is a second-order hyperbolic partial differential equation with coefficient  $a(x, t) > 0$  that is a non-constant function of time and space, and coefficient  $b > 0$  that is assumed to be constant. Equation (3.1) can be used to represent various well-studied physical systems. For example, Eq.(3.1) can be used to model wave propagation in a string, where  $u(x, t)$  is the transverse displacement of the string, in which case  $a(x, t) = T(x, t)$  is the string tension that may vary in time and space due to external processes, and  $b = \rho_0$  is the mass per unit length. Equation (3.1) can also be used to model the longitudinal wave propagation in a thin bar, where  $u(x, t)$  is the longitudinal particle displacement of the bar,  $a(x, t) = E(x, t)$  is the Young's modulus, and  $b = \rho_0$  is the mass per unit volume of the bar. In both of these examples,  $u(x, t)$  represents a displacement about an equilibrium configuration,  $a(x, t)$  is a general descriptor of the medium associated with the potential energy changes when the system is deformed from equilibrium, and  $b$  is a general descriptor associated with the kinetic energy changes when particles of the system are in motion. The elastodynamic equations presented in the later chapters have a similar form to Eq. (3.1), though it is of higher dimensionality. Therefore, the wave physics that can be modeled with Eq. (3.1) and the solution strategies used for the simpler one-dimensional example can be generalized to the general elastodynamic case in multiple dimensions.

Conservation laws require continuity conditions on the function  $u(x, t)$  and its derivative at each point in space  $x = x_0$ . Those continuity conditions are written as

$$\lim_{x \rightarrow x_0^-} u(x, t) = \lim_{x \rightarrow x_0^+} u(x, t), \quad \forall t, \quad (3.2)$$

$$\lim_{x \rightarrow x_0^-} a(x, t) \frac{\partial u}{\partial x} = \lim_{x \rightarrow x_0^+} a(x, t) \frac{\partial u}{\partial x}, \quad \forall t. \quad (3.3)$$

In elastodynamics, Eq. (3.2) represents continuity of displacement between two neighboring points that are separated by a vanishingly small distance and Eq. (3.3) represents continuity of stress at a material point. These relations are useful when deriving boundary and interface conditions.

Equation (3.1) usually does not admit an explicit analytical solution for a general functional form  $a(x, t)$ , in which case a direct numerical simulation must be performed. However, in the context of wave propagation in metamaterials considered in this work,  $a(x, t)$  is a periodic function of space and time. In other words, it is assumed that there is a reference modulation length,  $\lambda_m$ , in which  $a(x, t)$  is periodic in space for all time,

$$a(x + \lambda_m, t) = a(x, t), \quad (3.4)$$

and a reference time  $T_m$  with angular frequency  $\omega_m = 2\pi/T_m$  in which  $a(x, t)$  is periodic in time for all locations in space

$$a(x, t + T_m) = a(x, t). \quad (3.5)$$

Therefore, Bloch-Floquet wave theory can be utilized to derive differential equations which can be solved for the allowable traveling-wave modes that can

propagate and their respective dispersion behavior, or frequency-wavenumber spectrum [86]. Solution procedures for Eq. (3.1) with space-only, time-only, and space-time modulation of  $a(x, t)$  are now derived that are computationally feasible and yield accurate calculations of the Bloch wave modes and dispersion relations.

### 3.2 Space-Dependent Modulus

Consider a modulus which is a function of space only,  $a(x, t) \rightarrow a(x)$ . This case physically represents a periodic heterogeneous medium, which is a common acoustic metamaterial structure and is frequently referred to as a phononic crystal [87, 88]. Equation (3.1) then becomes

$$\frac{\partial}{\partial x} \left( a(x) \frac{\partial u}{\partial x} \right) - b \frac{\partial^2 u}{\partial t^2} = 0. \quad (3.6)$$

Despite having non-constant coefficients, the separation of variables method can be utilized, which assumes a product solution of the form  $u(x, t) = X(x)T(t)$  to relation Eq. (3.6). The assumed solution form is substituted into Eq. (3.6), which yields the expression

$$T (a(x)X')' - bXT'' = 0, \quad (3.7)$$

where the explicit dependence on  $x$  and  $t$  for functions  $X(x)$  and  $T(t)$  has been removed for simplicity. After division by  $XT$ , Eq. (3.7) becomes

$$\frac{(a(x)X')'}{X} = b \frac{T''}{T}, \quad (3.8)$$

where the left-hand side is a function of space and the right-hand side is a function of time. The only way for the equality to hold is for both sides to equal the separation constant,

$$\frac{(a(x)X')'}{bX} = \frac{T''}{T} = -\omega^2, \quad (3.9)$$

where  $\omega$  is the angular frequency. The time-dependent part of the total solution is then found by solving the ordinary differential equation

$$T'' + \omega^2 T = 0, \quad (3.10)$$

which has the general solution of the form

$$T = A_1 e^{i\omega t} + A_2 e^{-i\omega t}, \quad (3.11)$$

where  $A_1$  and  $A_2$  are arbitrary constants that depend on initial conditions. The time convention  $-i\omega t$  is assumed in this work, therefore  $A_1 = 0$  is assumed without loss of generality. The space-dependent portion of the total solution reduces to the following ordinary differential equation with non-constant coefficients,

$$(a(x)X')' + b\omega^2 X = 0. \quad (3.12)$$

Since  $a(x)$  is assumed to be a periodic function, Bloch-Floquet theory states that the general solution has the form

$$X = B_1 \hat{u}(x) e^{ikx} + B_2 \hat{u}^*(x) e^{-ikx}, \quad (3.13)$$

where  $\hat{u}$  is the Bloch mode and is a periodic function with period  $\lambda_m$ ,  $k$  is the Bloch wavenumber [86], and the superscript  $*$  denotes complex-conjugation.

Since a traveling-wave mode solution is desired,  $B_2 = 0$  and the sign of  $k$  represents the propagation direction in accordance with the assumed time convention. In the  $e^{-i\omega t}$  time convention, positive  $k$  values correspond to Bloch modes that propagate in the  $+x$  direction, and negative  $k$  values correspond to Bloch modes that propagate in the  $-x$  direction. The solution for  $u(x, t)$  is then

$$u(x, t) = C\hat{u}(x)e^{i(kx-\omega t)}, \quad (3.14)$$

where  $C$  is the amplitude constant. However, the Bloch mode  $\hat{u}$  and the dispersion relation  $\omega(k)$  must be determined from this general solution and the PDE provided in Eq. (3.6). Substitution of Eq. (3.14) into Eq. (3.6) yields the following ordinary differential equation for  $\hat{u}$  that is valid within the unit cell length  $L = \lambda_m$  centered at  $x = 0$ ,

$$\frac{d}{dx} \left[ a(x) \left( \frac{d\hat{u}}{dx} + ik\hat{u} \right) \right] + ik a(x) \frac{d\hat{u}}{dx} - k^2 a(x) \hat{u} + b\omega^2 \hat{u} = 0, \quad -\frac{L}{2} \leq x \leq \frac{L}{2}. \quad (3.15)$$

The periodic boundary conditions necessary to uniquely determine  $\hat{u}$  are derived using Eqns. (3.2)-(3.3) to yield

$$\hat{u}(-L/2) = \hat{u}(L/2), \quad (3.16)$$

$$\lim_{x \rightarrow L/2^-} a(x) \left( \frac{d\hat{u}}{dx} + ik\hat{u} \right) = \lim_{x \rightarrow -L/2^+} a(x) \left( \frac{d\hat{u}}{dx} + ik\hat{u} \right). \quad (3.17)$$

### 3.2.1 Variational Statement

A variational statement is an integral formulation of a PDE that is useful for finding solutions of boundary-value problems. A solution is sought

that satisfies the PDE in the sense of “weighted averages” of a suitable class of weight, or test, functions [89]. This particular solution technique has two advantages for this work: *i*) variational statements can be used to find solutions of PDEs with boundary conditions on arbitrary domains, *ii*) the coefficient  $a(x, t)$  is allowed to be non-smooth and even contain discontinuities. A variational approach can be utilized to obtain accurate approximations of the dispersion relation and the Bloch mode [90, 91]. This is derived by multiplying Eq. (3.15) by an arbitrary test function  $\hat{v}^*$  and integrating over the periodic interval  $[-L/2, L/2]$  to yield the following integral equation,

$$\begin{aligned} \int_{-L/2}^{L/2} \frac{d}{dx} \left[ a(x) \left( \frac{d\hat{u}}{dx} + ik\hat{u} \right) \right] \hat{v}^* dx + ik \int_{-L/2}^{L/2} a(x) \frac{d\hat{u}}{dx} \hat{v}^* dx \\ - k^2 \int_{-L/2}^{L/2} a(x) \hat{u} \hat{v}^* dx + b\omega^2 \int_{-L/2}^{L/2} \hat{u} \hat{v}^* dx = 0. \end{aligned} \quad (3.18)$$

Integration by parts is applied on the first integral to yield

$$\begin{aligned} \left[ a(x) \left( \frac{d\hat{u}}{dx} + ik\hat{u} \right) \right] \hat{v}^* \Big|_{-L/2}^{L/2} - \int_{-L/2}^{L/2} a(x) \frac{d\hat{v}^*}{dx} \frac{d\hat{u}}{dx} dx \\ + ik \int_{-L/2}^{L/2} a(x) \left( \frac{d\hat{u}}{dx} \hat{v}^* - \frac{d\hat{v}^*}{dx} \hat{u} \right) dx - k^2 \int_{-L/2}^{L/2} a(x) \hat{u} \hat{v}^* dx \\ + b\omega^2 \int_{-L/2}^{L/2} \hat{u} \hat{v}^* dx = 0. \end{aligned} \quad (3.19)$$

A symmetric variational statement, in which  $\hat{u}$  and  $\hat{v}$  can be interchanged without modifying the variational statement, is obtained if the functions  $\hat{v}$  are chosen such that they exist in the same function space as the solution  $\hat{u}$  [89]. In other words,  $\hat{v}$  has the same functional form as the solution with identical parameters to be determined and satisfies the periodic boundary condition

provided in Eqn. (3.16). Therefore, the first term on the LHS of Eq. (3.19), which is a boundary term, is identically zero, which yields the symmetric variational statement, or *weak form*, which is written as

$$\begin{aligned} \int_{-L/2}^{L/2} a(x) \frac{d\hat{v}^*}{dx} \frac{d\hat{u}}{dx} dx - ik \int_{-L/2}^{L/2} a(x) \left( \frac{d\hat{u}}{dx} \hat{v}^* - \frac{d\hat{v}^*}{dx} \hat{u} \right) dx \\ + k^2 \int_{-L/2}^{L/2} a(x) \hat{u} \hat{v}^* dx = b\omega^2 \int_{-L/2}^{L/2} \hat{u} \hat{v}^* dx. \end{aligned} \quad (3.20)$$

The solution is approximated using Galerkin's method by expanding the trial solution  $\hat{u}$  in a complete set of  $N$  basis functions  $\phi_i$  with coefficients  $c_i$  that satisfy periodic boundary conditions [89],

$$\hat{u} = \sum_{i=0}^N c_i \phi_i(x). \quad (3.21)$$

Likewise, the test function  $\hat{v}$  is expanded with the same set of basis functions with coefficients  $\beta_j$

$$\hat{v} = \sum_{j=0}^N \beta_j \phi_j(x). \quad (3.22)$$

Substitution of the above expansions for  $\hat{u}$  and  $\hat{v}$  into the weak form Eq. (3.20) yields

$$\sum_{i=0}^N \sum_{j=0}^N \beta_i^* [K_{ij} - \omega^2 M_{ij}] c_j = 0, \quad (3.23)$$

where

$$\begin{aligned} K_{ij} = \int_{-L/2}^{L/2} a(x) \frac{d\phi_i}{dx} \frac{d\phi_j}{dx} dx - ik \int_{-L/2}^{L/2} a(x) \left( \frac{d\phi_j}{dx} \phi_i - \frac{d\phi_i}{dx} \phi_j \right) dx \\ + k^2 \int_{-L/2}^{L/2} a(x) \phi_i \phi_j dx, \end{aligned} \quad (3.24)$$



and is termed the stiffness matrix, and

$$M_{ij} = \int_{-L/2}^{L/2} b\phi_i\phi_j dx, \quad (3.25)$$

and is termed the mass matrix. For Eq. (3.23) to hold for any set of coefficients  $\beta_i$ , the equations in the brackets must be zero, or

$$[K_{ij} - \omega^2 M_{ij}] c_j = 0. \quad (3.26)$$

This is a generalized eigenvalue problem which can be solved numerically for the coefficients  $c_j$  and angular frequency  $\omega^2$ . Since  $\mathbf{K}$  is a Hermitian matrix as a result of the symmetric variational statement, the eigenvalues are real-valued, and the eigenvectors are orthogonal. In other words, if  $\hat{u}_i$  is the eigenfunction with eigenvalue  $\omega_i$ , and  $\hat{u}_j$  is the eigenfunction with distinct eigenvalue  $\omega_j$ , then

$$\int_{-L/2}^{L/2} b\hat{u}_i^* \hat{u}_j dx = 0, \quad i \neq j. \quad (3.27)$$

Due to linearity of the PDE in Eq. (3.6), the eigenfunction  $\hat{u}$  is known up to a multiplicative constant. Therefore, it is standard procedure to normalize the eigenfunctions such that they satisfy the following integral statement

$$\int_{-L/2}^{L/2} b\hat{u}_i^* \hat{u}_i dx = 1. \quad (3.28)$$

While the variational statement and the Galerkin approximation provides an elegant framework for solving boundary-value problems, the choice of basis functions seems arbitrary and problem-dependent [89]. For example, since  $\hat{u}$  is a periodic function,  $\hat{u}, \hat{v}$  can be expanded as a Fourier series

$$\hat{u} = \sum_{n=-\infty}^{\infty} c_n e^{in(2\pi/L)x}. \quad (3.29)$$

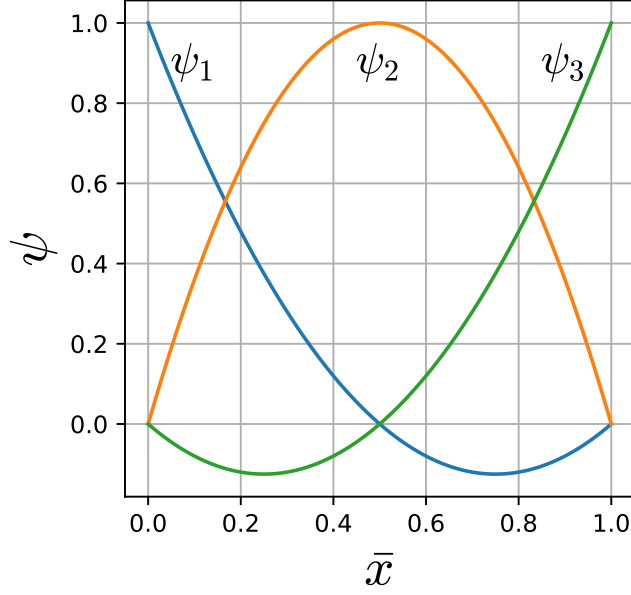


Figure 3.1: Second order finite element shape functions defined in a mesh element.

If this basis set is chosen, the mass matrix,  $\mathbf{M}$ , becomes a diagonal matrix due to the orthogonality of the Fourier series. However, depending on the regularity of  $a(x)$  convergence may be quite poor, i.e. many terms may be necessary to accurately represent  $\hat{u}$ . Consequently, the stiffness matrix,  $\mathbf{K}$ , will be fully-populated, which can significantly increase computational time if many terms are necessary. Moreover, in multiple dimensions this choice in basis functions is not ideal to fit boundary conditions on complex geometric domains and can lead to ill-conditioned matrices [89]. A more common approach is to subdivide the interval of  $x \in [-L/2, L/2]$  into  $N$  subdivisions, termed the computational mesh, where each subdivision is an element of the mesh with nodes  $x_j$ ,  $j = 0, 2, \dots, N$ . Each basis function is then constructed by

defining piecewise polynomials on each element. In this work, the basis functions are generated by using second-order polynomials. This is accomplished by including an additional node  $x_{j+1/2}$  at the midpoint of each element. Then, basis functions are chosen that satisfy the following at each node, or degree of freedom,

$$\phi_i(x_j) = \begin{cases} 1 & \text{if } i = j, \\ 0 & \text{if } i \neq j, \end{cases}, \quad i, j = 0, \frac{1}{2}, 1, \dots, N. \quad (3.30)$$

Basis functions that satisfy Eq. (3.30) can be generated at an element level using second-order Lagrange polynomials as shape functions defined over a mesh element

$$\psi_1(\bar{x}_j) = 2(\bar{x}_j - 0.5)(\bar{x}_j - 1), \quad (3.31)$$

$$\psi_2(\bar{x}_j) = -4\bar{x}_j(\bar{x}_j - 1), \quad (3.32)$$

$$\psi_3(\bar{x}_j) = 2\bar{x}_j(\bar{x}_j - \frac{1}{2}), \quad (3.33)$$

where

$$\bar{x}_j = \frac{x - x_j}{x_{j+1} - x_j}, \quad x_j \leq x \leq x_{j+1}. \quad (3.34)$$

These shape functions are plotted in Fig. 3.1. Finally, the basis functions can be defined from the following relation

$$\phi_j(x) = \begin{cases} \psi_1(\bar{x}_j), & x_j \leq x \leq x_{j+1} \text{ and } j \in [0, 1, 2, \dots, N], \\ \psi_3(\bar{x}_{j-1}), & x_{j-1} \leq x \leq x_j \text{ and } j \in [0, 1, 2, \dots, N], \\ \psi_2(\bar{x}_j), & x_j \leq x \leq x_{j+1} \text{ and } j \in [0, \frac{1}{2}, 1, \dots, N - \frac{1}{2}], \\ 0, & \text{otherwise.} \end{cases} \quad (3.35)$$

This method is the basis of the finite element method [40, 89] and has two main benefits. First, this choice in basis functions makes the mass and stiffness matrix sparse, which increases computational efficiency. Second, the coefficients

of the basis functions  $c_i$  in Eq. (3.21) are the values of the function  $\hat{u}$  at the nodes of the mesh. Therefore, better approximations to  $\hat{u}$  can be obtained by subdividing the interval into smaller partitions.

### 3.2.2 Eigenvalue Accuracy

In the previous subsection, it was shown that the variational statement leads to an eigenvalue problem which can be solved numerically for the Bloch mode and the eigenfrequency for a specified Bloch wavenumber,  $k$ . However, since the Bloch mode is approximated by a finite set of basis functions, the computed eigenfrequency is also approximate. This section therefore seeks to quantify the error of the computed eigenvalue with respect to the error of the Bloch mode.

Let  $\mathcal{L}(\hat{v}, \hat{u})$  and  $\mathcal{M}(\hat{v}, \hat{u})$  be the integral operators on the left-hand and right-hand side of Eq. (3.20), respectively. Since  $\hat{v}$  is in the same function space as the solution  $\hat{u}$ , let  $\hat{v} = \hat{u}$ . Equation (3.20) then becomes

$$\omega^2 \mathcal{M}(\hat{u}, \hat{u}) = \mathcal{L}(\hat{u}, \hat{u}). \quad (3.36)$$

Assume that the computed solution is close to the exact solution,  $\hat{u}_E$ , with a small error,  $\hat{u}(x) = \hat{u}_E(x) + \epsilon e(x)$ , where  $e(x)$  is residual error between the computed and exact solution at the point  $x$ , and  $\epsilon$  is the magnitude of the error. Substitution of this expansion into Eq. (3.36) yields

$$\begin{aligned} \omega^2 [\mathcal{M}(\hat{u}_E, \hat{u}_E) + \epsilon \mathcal{M}(e, \hat{u}_E) + \epsilon \mathcal{M}(\hat{u}_E, e) + \epsilon^2 \mathcal{M}(e, e)] \\ = \mathcal{L}(\hat{u}_E, \hat{u}_E) + \epsilon \mathcal{L}(e, \hat{u}_E) + \epsilon \mathcal{L}(\hat{u}_E, e) + \epsilon^2 \mathcal{L}(e, e). \end{aligned} \quad (3.37)$$

The variation of the eigenfrequency about the exact eigenvalue is found by taking the derivative of Eq. (3.37) with respect to  $\epsilon$  at  $\epsilon = 0$ . Using the fact that  $\mathcal{M}$  is symmetric, i.e.  $\mathcal{M}(\hat{v}, \hat{u}) = \mathcal{M}(\hat{u}, \hat{v})$ , and  $\mathcal{L}$  is Hermitian, i.e.  $\mathcal{L}(\hat{v}, \hat{u}) = \mathcal{L}^*(\hat{u}, \hat{v})$ , the eigenvalue derivative is given by the following

$$\left. \frac{d\omega^2}{d\epsilon} \right|_{\epsilon=0} = 2\Re \left( \mathcal{L}(e, \hat{u}_E) - \omega_E^2 \mathcal{M}(e, \hat{u}_E) \right). \quad (3.38)$$

Since  $(\omega_E, \hat{u}_E)$  is the exact eigenvalue-eigenvector pair to Eq. (3.20), then  $d\omega^2/d\epsilon = 0$ . This means that the estimate of the eigenvalue is second-order accurate with respect to the eigenvector error  $\epsilon$ ,

$$\omega^2 = \omega_E^2 + \mathcal{O}(\epsilon^2). \quad (3.39)$$

### 3.2.3 Example: Alternating Material Layers in a Bar

As an example case, consider longitudinal wave propagation in a bar composed of two periodically-alternating material layers with identical density  $b = \rho_0$ . The first layer has Young's modulus  $E_1$  and thickness  $L_1$ , and the second layer has Young's modulus  $E_2$  and thickness  $L_2$ . The periodic interval has length  $L = L_1 + L_2 = \lambda_m$  and unit cell defined at  $-L/2 \leq x \leq L/2$ . Assume, without loss of generality of the method, that the two layers have the same thickness,  $L_1 = L_2$ . The modulus  $a(x) = E(x)$  is therefore defined as the piecewise function

$$E(x) = \begin{cases} E_1, & \text{if } -\frac{L}{2} \leq x < 0, \\ E_2, & \text{if } 0 \leq x < \frac{L}{2}. \end{cases} \quad (3.40)$$

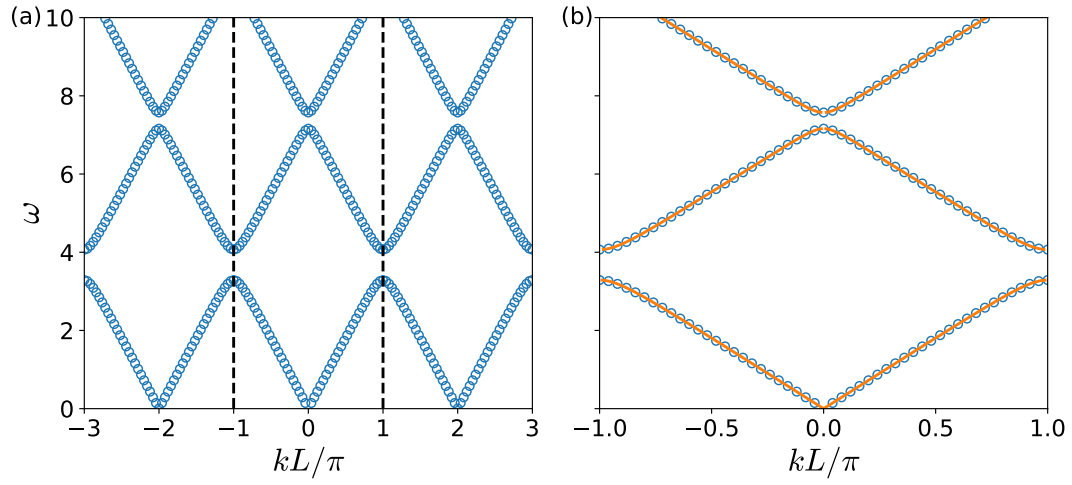


Figure 3.2: (a) Finite element computation of the dispersion relation for propagating longitudinal waves in a bar with periodic alternating layers. Since the dispersion relation is periodic, the complete dispersion relation can be obtained by restricting  $k$  to lie within the first Brillouin zone (black dashed lines). (b) Comparison of the finite element computation in the first Brillouin zone from (a) with the exact dispersion relation (orange lines), Eq. (3.41).

The exact dispersion relation in this case is the equation

$$\cos(kL) = \cos\left(\frac{\omega}{c_1}L_1\right)\cos\left(\frac{\omega}{c_2}L_2\right) - \frac{1}{2}\left(\frac{z_1}{z_2} + \frac{z_2}{z_1}\right)\sin\left(\frac{\omega}{c_1}L_1\right)\sin\left(\frac{\omega}{c_2}L_2\right), \quad (3.41)$$

where  $c_{1,2} = \sqrt{E_{1,2}/\rho_0}$  is the sound speed in each layer, and  $z_{1,2} = \rho_0 c_{1,2}$  is the impedance of each layer. The dispersion relation can also be calculated numerically using the variational statement described above. This is accomplished by assigning the value for the Bloch wavenumber  $k$  and solving Eq. (3.26) for the eigenfrequencies and Bloch modes. Second-order Lagrange polynomials are used as the finite element basis functions, and  $N = 20$  is sufficient for all of the plotted eigenfrequencies to converge. Figure 3.2(a) shows the resulting eigenfrequencies from the finite element calculation using the properties  $E_1 = 1$ ,  $E_2 = 2$ ,  $\rho_0 = 1$ ,  $L = 1$ , and Fig. 3.2(b) compares the finite element results with the exact dispersion relation provided by Eq. (3.41). Excellent agreement is attained between the exact dispersion relation and the finite element simulation. As a consequence of the Bloch-Floquet theory, the dispersion relation is also periodic with wavenumber periodicity  $\omega(k + k_L) = \omega(k)$ , where  $k_L = 2\pi/L$ . The complete dispersion curve can therefore be obtained by limiting  $k$  to the first Brillouin zone, which is the range  $k \in [-\pi/L, \pi/L]$  and is denoted by the vertical dashed lines in Fig. 3.2(a) [86]. In addition, the periodicity of the layers gives rise to Bragg scattering, in which the scattered waves caused by the impedance mismatch between the layers destructively interferes with the traveling wave at certain frequency bands [92, 93]. This interference creates bandgaps in the dispersion relation, which prohibits traveling waves

with frequencies within the gap. The widths of the bandgaps are a function of the contrast of the material moduli  $\Delta E = E_2 - E_1$ .

### 3.3 Time-Dependent Modulus

Now consider the case where the modulus is a periodic function of time,  $a(x, t) \rightarrow a(t)$ . For this case, Eq. (3.1) reduces to

$$a(t) \frac{\partial^2 u}{\partial x^2} - b \frac{\partial^2 u}{\partial t^2} = 0, \quad (3.42)$$

which can be rewritten as

$$\frac{\partial^2 u}{\partial x^2} - \frac{1}{c^2(t)} \frac{\partial^2 u}{\partial t^2} = 0, \quad (3.43)$$

where  $c^2(t) = a(t)/b$  is the time-varying sound speed. As with the case of a spatially-varying modulus, the separation of variables approach can be utilized, which assumes a product solution  $u(x, t) = X(x)T(t)$  for the PDE provided in Eq. (3.43). The assumed solution form is substituted into Eq. (3.43), yielding

$$X''T - \frac{1}{c^2(t)} T''X = 0, \quad (3.44)$$

or, after division by  $XT$ ,

$$\frac{X''}{X} = \frac{T''}{c^2(t)T}. \quad (3.45)$$

Since the left-hand side is a function of space and the right-hand side is a function of time, the only way for the equality to hold is if each side is equal to a separation constant

$$\frac{X''}{X} = \frac{T''}{c^2(t)T} = -k^2, \quad (3.46)$$



where  $k$  is identified as the wavenumber. The spatial ordinary differential equation is the Helmholtz equation

$$X'' + k^2 X = 0, \quad (3.47)$$

which has the general solution

$$X = A_1 e^{ikx} + A_2 e^{-ikx}. \quad (3.48)$$

The time-dependent ordinary differential equation is

$$T'' + k^2 c^2(t) T = 0, \quad (3.49)$$

which can be rewritten as

$$T'' + \frac{k^2}{b} a(t) T = 0. \quad (3.50)$$

Since  $a(t)$  is assumed to be periodic with frequency  $\omega_m = 2\pi/T_m$ ,  $a(t)$  can be written as a Fourier series

$$a(t) = \sum_{n=-\infty}^{\infty} \hat{a}_n e^{-in\omega_m t}, \quad (3.51)$$

whose coefficients  $\hat{a}_n$  are determined by the Fourier integral

$$\hat{a}_n = \frac{\omega_m}{2\pi} \int_{-\pi/\omega_m}^{\pi/\omega_m} a(t) e^{in\omega_m t} dt. \quad (3.52)$$

Since  $a(t)$  is a real-valued function, the negative index coefficients are complex-conjugates of the positive index coefficients, i.e.  $\hat{a}_{-m} = \hat{a}_m^*$ . Substitution of the Fourier series for  $a(t)$  into Eq. (3.50) yields the Hill differential equation

$$T'' + \frac{k^2}{b} \left( \sum_{n=-\infty}^{\infty} \hat{a}_n e^{-in\omega_m t} \right) T = 0. \quad (3.53)$$

Due to the periodicity of  $a(t)$ , Floquet's theorem can be utilized, which states that the general solution to Eq. (3.53) has the form

$$T = B_1 \Phi(t) e^{i\omega t} + B_2 \Phi^*(t) e^{-i\omega t}, \quad (3.54)$$

where  $\Phi(t)$  is a periodic function with period  $T_m$ .

The  $-\omega t$  time convention is assumed in this work, and therefore  $B_1 = 0$  without loss of generality. Since a traveling wave solution is desired,  $A_2 = 0$  in accordance with the assumed time convention. Therefore, the total solution  $u(x, t)$  has the form

$$u(x, t) = C \Phi(t) e^{i(kx - \omega t)}, \quad (3.55)$$

where positive  $k$  waves correspond to waves propagating in the  $+x$  direction, and negative  $k$  values correspond to waves propagating in the  $-x$  direction. Note that Eq. (3.55) has the same form as Eq. (3.14), except the Bloch function in Eq. (3.55) is now a periodic function of time. The Bloch function  $\Phi(t)$  and the dispersion relation  $\omega(k)$  can be determined by substituting Eq. (3.55) into Eq. (3.43) to yield the following differential equation for  $\Phi(t)$ ,

$$\Phi'' + 2i\omega\Phi' - \omega^2\Phi + \frac{k^2}{b} \left( \sum_{n=-\infty}^{\infty} \hat{a}_n e^{-in\omega_m t} \right) \Phi = 0. \quad (3.56)$$

Due to the periodicity of  $\Phi(t)$ , it can also be expanded as a Fourier series,

$$\Phi(t) = \sum_{m=-\infty}^{\infty} \hat{\Phi}_m e^{-im\omega_m t}, \quad (3.57)$$

and thus Eq. (3.56) yields the following

$$\sum_{m=-\infty}^{\infty} (\omega + m\omega_m)^2 \hat{\Phi}_m e^{im\omega_m t} = \frac{k^2}{b} \left( \sum_{n=-\infty}^{\infty} \hat{a}_n e^{-in\omega_m t} \right) \left( \sum_{q=-\infty}^{\infty} \hat{\Phi}_q e^{-iq\omega_m t} \right). \quad (3.58)$$

The Cauchy product of two series can be utilized on the right-hand side to yield

$$\sum_{m=-\infty}^{\infty} (\omega + m\omega_m)^2 \hat{\Phi}_m e^{-im\omega_m t} = \frac{k^2}{b} \sum_{n=-\infty}^{\infty} \sum_{q=-\infty}^{\infty} \hat{a}_{n-q} \hat{\Phi}_q e^{-in\omega_m t}. \quad (3.59)$$

By utilizing the orthogonality of the Fourier series, the above equation can be written by the following infinite system of algebraic equations

$$(\omega + p\omega_m)^2 \hat{\Phi}_p = \frac{k^2}{b} \sum_{m=-\infty}^{\infty} \hat{a}_{p-m} \hat{\Phi}_m, \quad p \in [-\infty, \infty]. \quad (3.60)$$

It is assumed that  $a(t)$  can be well represented with  $2P + 1$  terms and therefore the number of solution harmonics  $\hat{\Phi}_m$  and the sum in Eq. (3.60) can be truncated, i.e.  $p, m \in [-P, P]$ . Finally, expanding the term  $(\omega + p\omega_m)^2$  yields the quadratic eigenvalue problem [94]

$$\omega^2 \mathbf{M} \hat{\Phi} + \omega \mathbf{C} \hat{\Phi} + \mathbf{K} \hat{\Phi} = 0, \quad (3.61)$$

where  $\hat{\Phi} = [\hat{\Phi}_{-P}, \hat{\Phi}_{-P+1}, \dots, \hat{\Phi}_P]^T$ ,  $\mathbf{M}$  is the identity matrix,  $\mathbf{C}$  depends on  $\omega_m$ , and  $\mathbf{K}$  depends on  $\hat{a}$ ,  $\omega_m$ , and  $k$ . The solution  $u(x, t)$  can therefore be written using Eq. (3.55) as

$$u(x, t) = e^{i(kx - \omega t)} \sum_{p=-P}^P \hat{\Phi}_p e^{-ip\omega_m t}, \quad (3.62)$$

which can be rewritten as

$$u(x, t) = e^{ikx} \sum_{p=-P}^P \hat{\Phi}_p e^{-i(\omega + p\omega_m)t}. \quad (3.63)$$

Equation (3.63) is very important to observations of time-modulated and spatiotemporally-modulated media. Specifically, one can interpret the effect

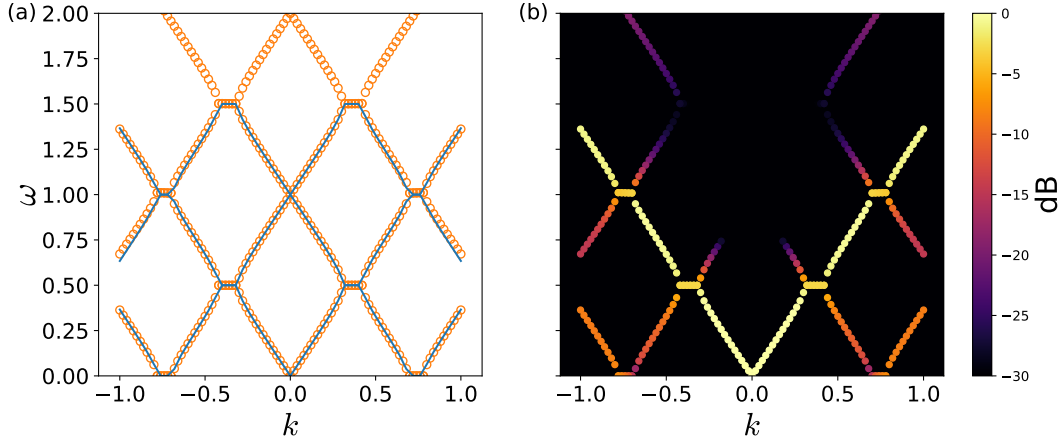


Figure 3.3: (a) Comparison of the frequency-wavenumber spectrum of Hill's equation using Eq. (3.61) (open circles) with the exact dispersion solution, Eq. (3.66). (b) Dispersion relation from (a) weighted by the magnitude of the fundamental plane wave component in decibels,  $20 \log_{10}(\|\hat{\Phi}_0\|/\|\hat{\Phi}\|)$ .

of temporal modulation of the modulus as a perturbation to the medium that excites plane waves with wavenumber  $k$  at frequencies  $(\omega + p\omega_m)$  having amplitudes  $\hat{\Phi}_p$ . Note that the wavelength of each plane wave is the same; however, each plane wave propagates with the speed  $(\omega + p\omega_m)/k$ . Further, the amplitude of each plane wave is dependent on the magnitude of the harmonics of  $a(t)$ .

### 3.3.1 Example: Hill's Equation

As an example, consider the propagation of longitudinal waves in a bar with constant density  $b = \rho_0$  and a time-varying Young's modulus  $a(t) \rightarrow E(t)$  that varies as a square wave with minimum value  $E_1$  and maximum value  $E_2$ ,

which is written as

$$E(t) = E_1 + \Delta E H[\cos(\omega_m t)], \quad (3.64)$$

where  $H$  is the Heaviside function, and  $\Delta E = E_2 - E_1$ . The Fourier coefficients in Eq. (3.51) are then

$$\hat{E}_n = E_2 \delta_{n0} - \frac{\Delta E}{2} \text{sinc}\left(\frac{n\pi}{2}\right), \quad (3.65)$$

where  $\text{sinc}(x) = \sin(x)/x$  and  $\delta_{n0}$  is the Kronecker delta. The exact dispersion relation in this case is the equation

$$\begin{aligned} \cos(\omega T) &= \cos(kc_1 T_1) \cos(kc_2 T_2) \\ &\quad - \frac{1}{2} \left( \frac{c_1 T_1}{c_2 T_2} + \frac{c_2 T_2}{c_1 T_1} \right) \sin(kc_1 T_1) \sin(kc_2 T_2), \end{aligned} \quad (3.66)$$

where  $T_1 = T_2 = \pi/\omega_m$ ,  $T = T_1 + T_2$ , and  $c_{1,2} = \sqrt{E_{1,2}/\rho_0}$  [86]. This particular case has a similar dispersion form to the space-only dispersion relation, Eq. (3.41). Figure 3.3(a) compares the dispersion relation computed using Eq. (3.61) with parameters  $P = 5$ ,  $\omega_m = 1$ ,  $E_1 = 1$ ,  $E_2 = 3$ ,  $\rho_0 = 1$  and two branches of the exact dispersion relation, Eq.(3.66). Note that the dispersion curves in Fig. 3.3(a) are periodic in frequency, which is the analogue to wavenumber periodicity in the case of a spatially-varying modulus. The computed dispersion relation using Eq. (3.61) agrees well with the exact dispersion curves, and better agreement is obtained, particularly in the higher frequencies, by retaining more terms in the sum in Eq. (3.60). It is observed from Fig. 3.3(a) that this system exhibits wavenumber gaps, which is the analog of bandgaps in frequency for the the case of a spatially-varying modulus.

However, propagating waves within the wavenumber bandgaps are unstable and exhibit infinite growth in amplitude in the lossless case [95]. While this result is relevant to applications using modulated media, it is noted that in the case where the modulus is a general function of space and time, it is assumed that the modulation frequency is much smaller than the frequencies of the propagating waves. Therefore, wavenumber bandgaps will not be present in the frequency-wavenumber spectrum.

The elements from the computed eigenvector  $\hat{\Phi}$  are the amplitudes of the plane waves in Eq. (3.63). One also notes that the total energy of the propagating waves, which is related to the squared magnitude of the plane wave amplitudes, are not evenly distributed across each frequency. This can be represented on a frequency-wavenumber spectrum by weighting each curve by the magnitude of the fundamental plane wave amplitude  $||\hat{\Phi}_0||^2$ . Figure 3.3(b) depicts the same results as Fig. 3.3(a), but each curve is now assigned a color that represents the normalized magnitude of the fundamental ( $p = 0$ ) plane wave component in decibels, specifically  $20 \log_{10}(||\hat{\Phi}_0||/||\hat{\Phi}||)$ . The main dispersion branch is now easily identifiable, as well as the branches that interact with the main branch near the wavenumber gaps.

### 3.4 Space- and Time-Dependent Modulus

Finally, consider the case where now  $a(x, t)$  is a periodic function of time and space. Unfortunately, separation of variables does not apply to this particular problem. However, the solution techniques discussed for the time-

only and space-only modulus cases can be leveraged. First,  $a(x, t)$  is expanded as a Fourier series in time

$$a(x, t) = \sum_{n=-\infty}^{\infty} \hat{a}_n(x) e^{-in\omega_m t} \quad (3.67)$$

where  $\hat{a}_n(x)$  are the harmonic amplitudes and are periodic functions of space. As in the previous sections, a Bloch wave solution is assumed, where the Bloch mode  $U(x, t)$  is now a periodic function of time and space

$$u(x, t) = e^{i(kx - \omega t)} U(x, t). \quad (3.68)$$

Therefore,  $U(x, t)$  can also be expanded as a Fourier series in time with harmonic amplitudes that are a function of space

$$U(x, t) = \sum_{m=-\infty}^{\infty} \hat{u}_m(x) e^{-im\omega_m t}. \quad (3.69)$$

Equations (3.67) and (3.69) are substituted into Eq. (3.1) to yield the differential equation for the harmonic amplitudes  $\hat{u}_m$

$$\sum_{p=-\infty}^{\infty} \sum_{m=-\infty}^{\infty} \left[ \frac{d}{dx} \left( \hat{a}_{p-m} \left( \frac{d\hat{u}_m}{dx} + ik\hat{u}_m \right) \right) + ik\hat{a}_{p-m} \frac{d\hat{u}_m}{dx} - k^2 \hat{a}_{p-n} \hat{u}_m + b(\omega + p\omega_m)^2 \hat{u}_m \right] e^{i(\omega + p\omega_m)t} = 0. \quad (3.70)$$

Utilizing harmonic balance from the orthogonality of the Fourier series yields the infinite system of coupled differential equations

$$\sum_{m=-\infty}^{\infty} \frac{d}{dx} \left[ \hat{a}_{p-m} \left( \frac{d\hat{u}_m}{dx} + ik\hat{u}_m \right) \right] + ik\hat{a}_{p-m} \frac{d\hat{u}_m}{dx} - k^2 \hat{a}_{p-n} \hat{u}_m + b(\omega + p\omega_m)^2 \hat{u}_p = 0, \quad p \in [-\infty, \infty]. \quad (3.71)$$

Equation (3.71) implies that the one must solve a set of ODEs for each Fourier amplitude associated with the time solution. Therefore, a variational approach similar to the space-only modulus approach can be used by multiplying each equation in Eq. (3.71) by its respective test function,  $\hat{v}_p$ , and integrating over the periodic interval,  $x \in [-\lambda_m/2, \lambda_m/2]$ . Integration by parts is used on the bracketed terms in Eq. (3.71) to yield the symmetric weak form

$$\begin{aligned} & \sum_{p=-\infty}^{p=\infty} \sum_{m=-\infty}^{\infty} \left[ \int_{-\lambda_m/2}^{\lambda_m/2} \hat{a}_{p-m} \frac{d\hat{u}_m}{dx} \frac{d\hat{v}_p}{dx} dx + k^2 \int_{-\lambda_m/2}^{\lambda_m/2} \hat{a}_{p-m} \hat{u}_m \hat{v}_p dx \right. \\ & \left. - ik \int_{-\lambda_m/2}^{\lambda_m/2} a_{p-m} \left( \hat{u}_m \frac{d\hat{v}_p}{dx} - \frac{d\hat{u}_m}{dx} \hat{v}_p \right) dx - b(\omega + p\omega_m)^2 \int_{-\lambda_m/2}^{\lambda_m/2} \hat{u}_p \hat{v}_p dx \right] = 0. \end{aligned} \quad (3.72)$$

The integration domain  $x \in [-\lambda_m/2, \lambda_m/2]$  is subdivided into  $N$  intervals and  $\hat{u}_m, \hat{v}_m$  are expanded in the usual manner as piecewise Lagrange polynomials

$$\hat{u}_m = \sum_{j=0}^N \hat{u}_j^m \phi_j(x), \quad (3.73)$$

$$\hat{v}_m = \sum_{i=0}^N \hat{v}_i^m \phi_i(x), \quad (3.74)$$

where  $\hat{u}_j^m$  is the value of  $\hat{u}_m$  at node  $j$ . Substitution of the above basis expansions for  $\hat{u}^m, \hat{v}^m$  yields the following set of equations for any suitable test function  $\hat{v}_m$

$$\omega^2 \mathbf{M} \mathbf{u}^p + \omega 2\omega_m p \mathbf{M} \mathbf{u}^p + (\omega_m p)^2 \mathbf{M} \mathbf{u}^p + \sum_{m=-P}^P \mathbf{K}^{p-m} \mathbf{u}^m = 0, \quad p \in [-P, P], \quad (3.75)$$

where  $\mathbf{u}^p = [\hat{u}_0^p, \dots, \hat{u}_N^p]^T$  and



$$M_{ij} = b \int_{-L/2}^{L/2} \phi_i \phi_j dx, \quad (3.76)$$

$$K_{ij}^n = \int_{-L/2}^{L/2} \left( -\hat{a}_n \frac{d\phi_i}{dx} \frac{d\phi_j}{dx} + ik\hat{a}_n \left( \phi_i \frac{d\phi_j}{dx} - \frac{d\phi_j}{dx} \phi_i \right) - k^2 \hat{a}_n \phi_i \phi_j \right) dx. \quad (3.77)$$

Equation (3.75) can be assembled as a global system

$$\omega^2 \bar{\mathbf{M}} \mathbf{u} + \omega \bar{\mathbf{C}} \mathbf{u} + \bar{\mathbf{K}} \mathbf{u} = 0 \quad (3.78)$$

where  $\mathbf{u} = [\hat{u}_0^{-P}, \dots, \hat{u}_N^{-P}, \hat{u}_0^{-P+1}, \dots, \hat{u}_N^{-P+1}, \dots, \hat{u}_0^P, \dots, \hat{u}_N^P]^T$ ,  $\bar{\mathbf{M}}$  is the global assembly of the first term,  $\bar{\mathbf{C}}$  is the global assembly of the second term, and  $\bar{\mathbf{K}}$  is the global assembly of the third and fourth terms of Eq. (3.75), respectively.

### 3.4.1 Example: Translating Material Layers

As an example, consider the case of longitudinal wave propagation in a bar with constant density  $b = \rho_0$  composed of periodic alternating layers from Sec. 3.2.3 now translating in the  $+x$  direction at speed  $c_m = \omega_m/k_m$ , where  $k_m = 2\pi/\lambda_m$  is the modulation wavenumber. Therefore, the Young's modulus  $a(x, t) \rightarrow E(x, t)$  has the following functional form, which was recently studied using a different approach by Trainiti and Ruzzene [31]

$$E(x, t) = E_1 + \Delta E H [\cos(k_m x - \omega_m t)], \quad (3.79)$$

which is a generalization of the time-varying Young's modulus, Eq. (3.64).

The Fourier coefficients in Eq. (3.67) are thus given by [31]

$$\hat{E}_n = \left( E_2 \delta_{n0} - \frac{\Delta E}{2} \text{sinc} \left[ \frac{\pi n}{2} \right] \right) e^{in k_m x}. \quad (3.80)$$

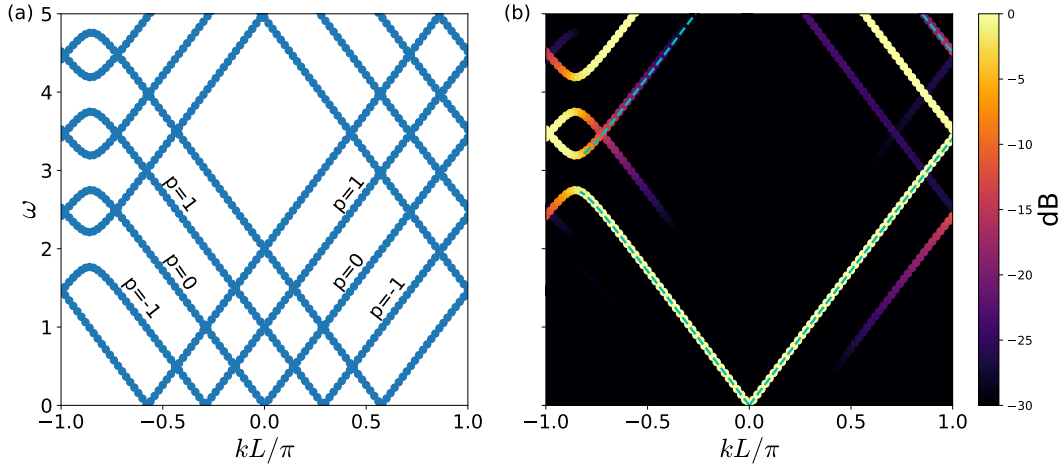


Figure 3.4: (a) Finite element computation of the dispersion relation for the case of translating material layers with modulation speed  $c_m = 0.159$  ( $\omega_m = 1$ ). Due to the bias in the  $+x$  direction, the dispersion curves are not symmetric about  $k = 0$ , i.e. reciprocity is broken. (b) The dispersion curves shown in (a) but with each point colored by the magnitude of the fundamental component in decibels,  $20 \log_{10}(\|\mathbf{u}^0\|/\|\mathbf{u}\|)$ . The dashed line is the first branch of the exact dispersion relation for this case, which is obtained using Eq. (3.83) and Eq. (3.41).

The exact dispersion relation in this case can be obtained by shearing the dispersion relation for the case of spatial variation of the Young's modulus, Eq. (3.41). This is accomplished by replacing  $k$  with  $\hat{k}$ ,  $\omega$  with  $\hat{\omega}$ , and  $c_1, c_2$  with  $\hat{c}_1, \hat{c}_2$ , where

$$\hat{c}_1 = c_1 - \frac{c_m^2}{c_1}, \quad (3.81)$$

$$\hat{c}_2 = c_2 - \frac{c_m^2}{c_2}. \quad (3.82)$$

and solving Eq. (3.41) with these transformed variables [96]. The variables  $(\hat{k}, \hat{\omega})$  can be transformed back to  $(k, \omega)$  with the following transformation

$$k = \hat{k} + \frac{\hat{\omega}c_m L_1}{L(c_1^2 - c_m^2)} + \frac{\hat{\omega}c_m L_2}{L(c_2^2 - c_m^2)}, \quad (3.83)$$

$$\omega = \hat{\omega} + c_m \hat{k} + \frac{\hat{\omega}c_m^2 L_1}{L(c_1^2 - c_m^2)} + \frac{\hat{\omega}c_m^2 L_2}{L(c_2^2 - c_m^2)}. \quad (3.84)$$

Figure 3.4(a) shows the dispersion calculation from the finite element model using the parameters  $E_1 = 1$ ,  $E_2 = 1.5$ ,  $\rho_0 = 1$ ,  $L = 1$ ,  $P = 2$ , and  $\omega_m = 1$ . As in the time-only modulation case, the entire frequency spectrum can be generated by translating the fundamental ( $p = 0$ ) branch by  $\pm p\omega_m$ . A bias in space-time has now been introduced in the  $+x$  direction which breaks time-reversal symmetry, and the dispersion relation is no longer symmetric about the  $k = 0$  axis. Therefore, reciprocity is broken. Figure 3.4(b) shows the same dispersion curves as in Fig. 3.4(a), but with each point assigned a color determined by the magnitude of the fundamental component in decibels, specifically  $20 \log_{10}(\|\mathbf{u}^0\|/\|\mathbf{u}\|)$ . As in the time-only modulation case, it is evident from this plot that the harmonic amplitudes for each plane wave

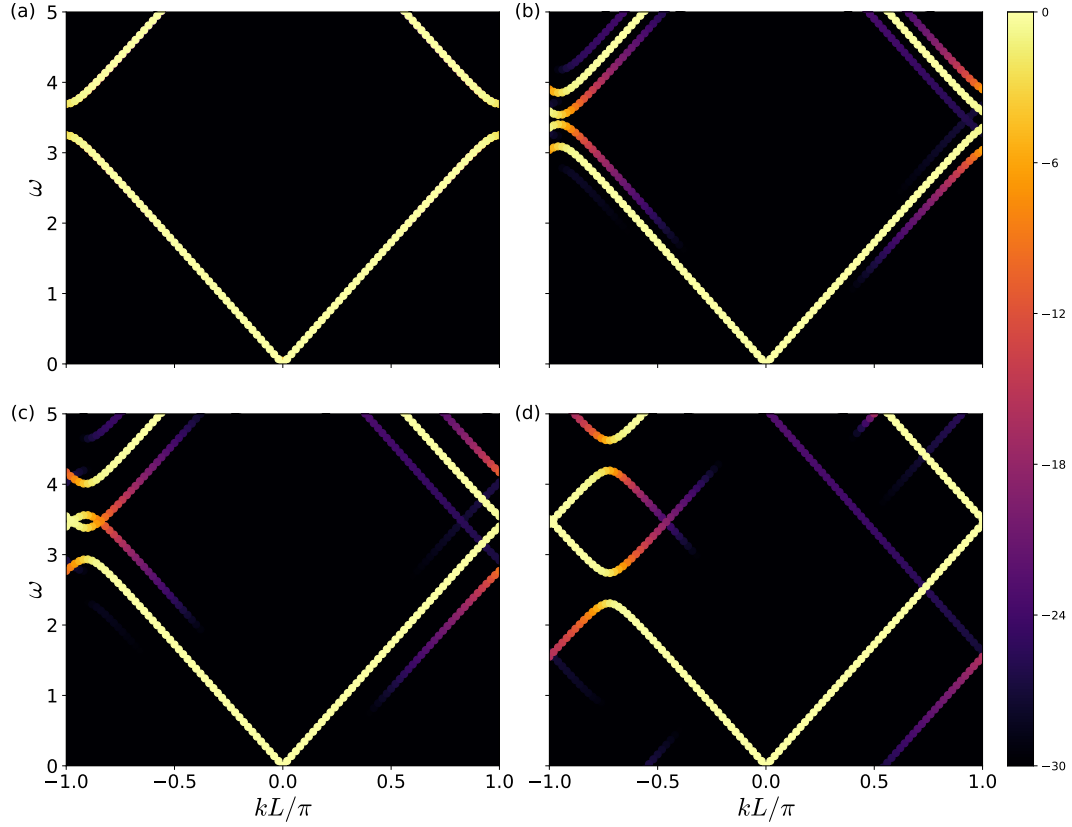


Figure 3.5: Dispersion relations for the translating layers case as a function of the modulation speed  $c_m$ . (a) No translation,  $c_m = 0$ , (b)  $c_m = 0.05$ , (c)  $c_m = 0.1$ , (d)  $c_m = 0.3$ .

in Eq. (3.69) are not equal. This representation now shows what appears to be directional bandgaps in the  $-x$  direction that do not exist in the  $+x$  direction. These bandgaps are not identical to bandgaps in a system with only a spatially-varying modulus, since modes with small amplitudes do exist within the bandgap. It can be seen from Fig. 3.4(b) that the fundamental branch ( $p = 0$ ) agrees with the exact dispersion relation computed using the transformed variables, Eq. (3.83), and Eq. (3.41).

The frequency ranges of the directional bandgaps can be tuned with the speed of the modulation,  $c_m$ . Figure 3.5 depicts the changes in the dispersion relation as  $c_m$  is increased. For low modulation speed, mode splitting occurs and the spatial-only dispersion solution splits into the  $\pm\omega_m$  curves [97]. For a modulation speed of  $c_m = 0.1$ , the band gap in the  $+x$  direction closes, and the band gap in the  $-x$  direction splits into two directional band gaps, where the lowest directional band gap translates down as the modulation speed is increased, and the higher directional band gap translates up in frequency as the modulation speed is increased. The width of the band gap can be tuned in the same way as the spatial-only modulation case, by increasing the contrast ( $\Delta E$ ) between layers.

### 3.4.2 Harmonic Mode Coupling

Though the full numerical solution in Eq. (3.78) provides a means to calculate the frequency-wavenumber spectrum for arbitrary time and space modulation of the modulus, it does not offer any clear insight into the coupling strength between two modes and the width of the directional bandgap. It is therefore informative to find approximate relationships to calculate the frequency-wavenumber spectrum. The coupling between two modes and the resulting directional bandgap created from their interaction is now investigated.

In a spatiotemporally-modulated medium, the modes are no longer orthogonal as in the spatial-only case, which implies that the modes can interact

and couple to each other. Previous work has shown that directional bandgaps occur when two or more modes interact [31, 32]. This is illustrated by rewriting Eq. (3.75) in the following form

$$(\mathbf{K}^0 - (\omega + p\omega_m)^2 \mathbf{M}) \mathbf{u}^p = - \sum_{\substack{n=-P \\ n \neq p}}^P \mathbf{K}^{p-n} \mathbf{u}^n, \quad p \in [-P, P], \quad (3.85)$$

which mathematically states that each mode  $p$  with natural frequency  $(\omega + p\omega_m)$  is being driven by the other modes, in which the magnitude of the coupling strength between mode  $p$  and another mode  $n$  is related to the norm of the matrix  $\mathbf{K}^{p-n}$ . Without loss of generality, consider the interaction of the  $p = 0$  and  $p = 1$  modes

$$(\mathbf{K}^0 - \omega^2 \mathbf{M}) A \mathbf{u}^0 = -\mathbf{K}^{-1} B \mathbf{u}^1, \quad (3.86)$$

$$(\mathbf{K}^0 - (\omega + \omega_m)^2 \mathbf{M}) B \mathbf{u}^1 = -\mathbf{K}^1 A \mathbf{u}^0, \quad (3.87)$$

where  $A$  and  $B$  are the amplitudes of the modes  $\mathbf{u}^0, \mathbf{u}^1$ , respectively. The eigenvalue is expanded as the following

$$\omega = \bar{\omega}_i + \delta\omega, \quad (3.88)$$

where  $\bar{\omega}_i$  is an eigenvalue to the right-hand side of Eq. (3.86),

$$(\mathbf{K}^0 - \bar{\omega}_i^2 \mathbf{M}) \bar{\mathbf{u}}_i = 0, \quad (3.89)$$

with eigenvector  $\bar{\mathbf{u}}_i$ . Assume without loss of generality that  $\bar{\omega}_0$  is the eigenfrequency of the mode of interest,  $\bar{\mathbf{u}}_0$ , and that the mode  $\bar{\mathbf{u}}_1$  lies on the dispersion

branch which contains  $(\bar{\omega}_0 + \omega_m)$ . Substitution of Eq. (3.88) into Eqns. (3.86)-(3.87) yields the coupled system

$$(\mathbf{K}^0 - \bar{\omega}_0^2 \mathbf{M}) A \mathbf{u}^0 = (2\bar{\omega}_0 \delta\omega + \delta\omega^2) \mathbf{M} A \mathbf{u}^0 - \mathbf{K}^{-1} B \mathbf{u}^1, \quad (3.90)$$

$$(\mathbf{K}^0 - (\bar{\omega}_0 + \omega_m)^2 \mathbf{M}) B \mathbf{u}^1 = (2\delta\omega(\bar{\omega}_0 + \omega_m) + \delta\omega^2) \mathbf{M} B \mathbf{u}^1 - \mathbf{K}^1 A \mathbf{u}^0. \quad (3.91)$$

Taking the inner product of Eq. (3.90) with  $\bar{\mathbf{u}}_0$  and the Eq. (3.91) with  $\bar{\mathbf{u}}_1$  yields

$$-(2\bar{\omega}_0 \delta\omega + \delta\omega^2) \bar{\mathbf{u}}_0^H \mathbf{M} \mathbf{u}^0 A - \bar{\mathbf{u}}_0^H \mathbf{K}^{-1} \mathbf{u}^1 B = 0, \quad (3.92)$$

$$-\bar{\mathbf{u}}_1^H \mathbf{K}^1 \mathbf{u}^0 A + [(2\delta\omega(\bar{\omega}_0 + \omega_m) + \delta\omega^2) \bar{\mathbf{u}}_1^H \mathbf{M} \mathbf{u}^1 - Q] B = 0, \quad (3.93)$$

where

$$Q = \bar{\mathbf{u}}_1^H (\mathbf{K}^0 - (\bar{\omega}_0 + \omega_m)^2 \mathbf{M}) \mathbf{u}^1, \quad (3.94)$$

and it was made use of the fact that  $\bar{\mathbf{u}}_0$  is also the left eigenvector of Eq. (3.88),

$$\bar{\mathbf{u}}_0^H (\mathbf{K}^0 - \bar{\omega}_0^2 \mathbf{M}) = 0, \quad (3.95)$$

where the superscript H denotes Hermitian transpose. In order to solve Eqns. (3.92)-(3.93), the modes  $\mathbf{u}^0$ ,  $\mathbf{u}^1$  need to be determined. However, they can be approximated as

$$\mathbf{u}^0 \approx \bar{\mathbf{u}}_0, \quad \mathbf{u}^1 \approx \bar{\mathbf{u}}_1. \quad (3.96)$$

The determinant of Eqns. (3.92)-(3.93) is set to zero, which yields the equation for  $\delta\omega$

$$\begin{aligned} \delta\omega^4 + (4\bar{\omega}_0 + \omega_m) \delta\omega^3 + (4\bar{\omega}_0^2 + \bar{\omega}_0 \omega_m - Q) \delta\omega^2 - 2\bar{\omega}_0 Q \delta\omega \\ = (\bar{\mathbf{u}}_1^H \mathbf{K}^1 \bar{\mathbf{u}}_0) (\bar{\mathbf{u}}_0^H \mathbf{K}^{-1} \bar{\mathbf{u}}_1). \end{aligned} \quad (3.97)$$

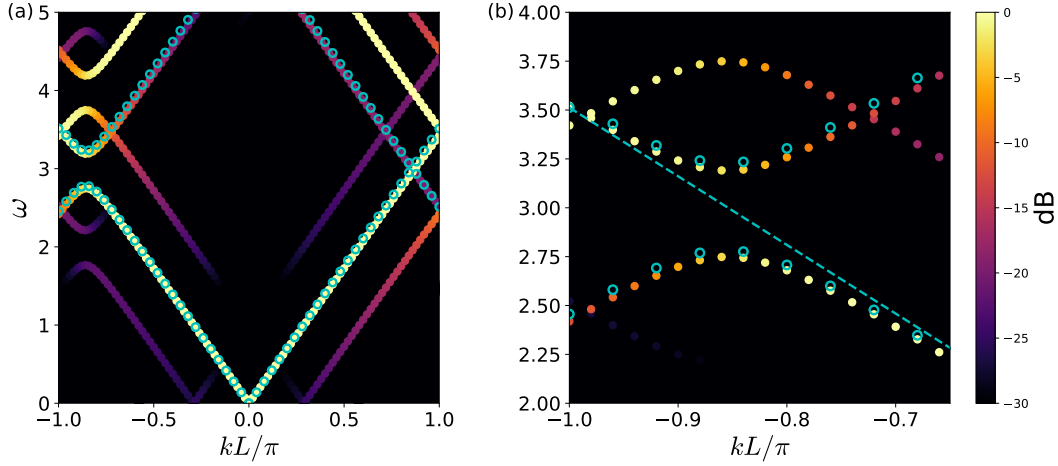


Figure 3.6: (a) Approximate dispersion relation using Eq. (3.97) (open circles) compared to Fig. 3.4(a). (b) Zoom-in plot of the lowest directional bandgap. The dashed line represents the solution  $\bar{\omega}_0$  from Eq. (3.89).

The roots of the above quartic equation can be solved using a numerical polynomial root-finding algorithm. The mode amplitude ratio  $B/A$  can then be determined from Eq. (3.92)

$$\frac{B}{A} = \frac{2\bar{\omega}_0\delta\omega + \delta\omega^2}{\bar{\mathbf{u}}_0^H \mathbf{K}^{-1} \bar{\mathbf{u}}_1}. \quad (3.98)$$

Figure 3.6(a) shows the results of using Eq. (3.97) to calculate the approximate dispersion relation on the first branch, and Fig. 3.6(b) shows the approximate dispersion relation at the first directional bandgap. The root with the smallest magnitude in Eq. (3.97) captures the fundamental dispersion branch and the directional bandgap, while the other roots capture the features further away from the fundamental dispersion branch. The approximate dispersion relation agrees well with the full solution, Eq. (3.78). Figure



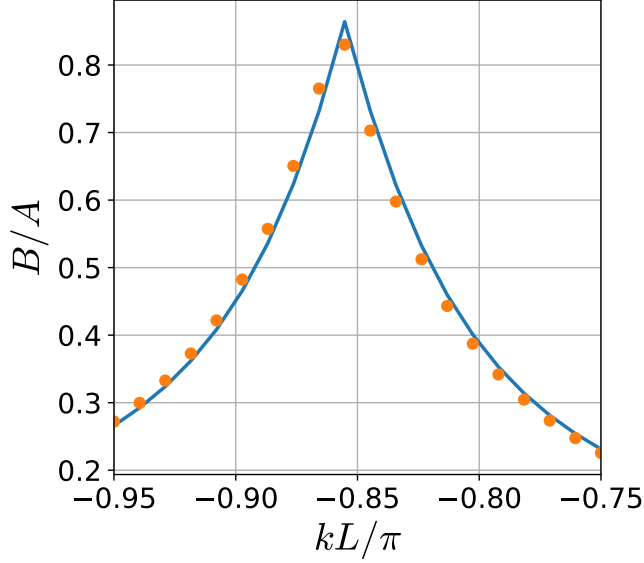


Figure 3.7: Ratio of the amplitude  $B$  of mode  $\mathbf{u}^1$  over amplitude  $A$  of mode  $\mathbf{u}^0$  at the lowest directional band gap. The solid line represents the direct QEP solution, and circles are from Eq. (3.98).

3.7 compares the modal amplitudes of mode  $\mathbf{u}^0$  and  $\mathbf{u}^1$  from the full solution, Eq. (3.78), and the approximate solution, Eq. (3.98), at the lowest bandgap. Note that even with the mode approximations made (Eq. (3.96)) the amplitude ratios are in good agreement.

The main advantage of this approximate method is that the frequency-wavenumber spectrum can be generated by solving the generalized eigenvalue problem Eq. (3.89), which is computationally less demanding than solving the full quadratic eigenvalue problem, Eq. (3.78). The computational savings is even more noticeable for larger degree-of-freedom systems, such as the negative stiffness honeycomb case in Chapter 5. However, Eq. (3.78) is more useful when generating the frequency-wavenumber spectrum over a

large frequency band, as each branch must be constructed individually using Eq. (3.97) by considering each possible mode coupling combination. The quadratic eigenvalue solver that is used to compute solutions to Eq. (3.78) can also take advantage of distributed parallel computing (discussed in Sec. 5.3) for large problems, which significantly reduces computation runtime. Therefore, it is recommended to use Eq. (3.78) when exploring directional bandgaps in spatiotemporally-modulated systems, and Eq. (3.97) when optimizing particular directional bandgap widths of interest in a design setting for applications.

### 3.5 Summary

In this chapter, wave phenomena in a one-dimensional medium were studied for space-only, time-only, and spatiotemporal modulations of the material modulus. The spatial modulation of the material modulus was first investigated. A variational approach was utilized to determine the Bloch mode and dispersion relation, and the finite element method was chosen to numerically discretize the resulting integrals, which led to a generalized eigenvalue problem for the Bloch modes and eigenfrequencies. It was shown with an example problem that considered longitudinal wave propagation in a bar with periodic layers that frequency bandgaps exist, which prohibits traveling waves with frequencies within the gap.

The time modulation of the material modulus was then analyzed. A Fourier series expansion was utilized to reduce the differential equations into a coupled set of algebraic expressions, which resulted in a quadratic eigenvalue

problem. It was shown with an example problem concerning periodic time variations of the material modulus that wavenumber gaps exist, which is the analogue to frequency bandgaps in the case of spatial-only modulation of the material modulus.

Finally, the spatiotemporally-modulated material modulus case was investigated. The solution technique utilized the Fourier transform method presented for the time-only modulation case and the variational technique used in the space-only modulation case, which resulted in a quadratic eigenvalue problem for the Bloch wave modes and eigenfrequencies. The case of propagating longitudinal waves in a bar with translating material layers was then analyzed. Due to the bias of the modulation in the  $+x$  direction, the dispersion relation was no longer symmetric about the  $k = 0$  axis and reciprocity is therefore broken. Approximate relations for the dispersion relation and the modal amplitudes were derived by considering the interaction of two coupled modes. This approximate method agreed well with the full quadratic eigenvalue computation and can be used to generate guesses on directional bandgaps of interest.

The solution techniques discussed in this chapter will be utilized in Chapters 4 and 5 to model elastic wave propagation in two dimensions. The variational technique has the added benefit that it can be used on a domain with arbitrary shape. The computational methods described in this chapter are therefore well-suited for studying elastic wave propagation in a metamaterial composed of unit cells with complex geometry, such as the negative

stiffness honeycomb.

## Chapter 4

# Negative Stiffness Honeycombs as Tunable Elastic Metamaterials<sup>1</sup>

### 4.1 Introduction

The finite element method introduced in Chapter 3 is now generalized and employed to solve the equations of motion in a pre-strained negative stiffness honeycomb (NSH), which is reproduced for convenience in Fig. 4.1. This chapter introduces the small-on-large approximation, which is used to separate the calculation of the total displacement into a nonlinear model which accounts for the large deformation from an applied pre-strain, and a linear elastic wave model linearized about the prescribed deformation. The dispersion curves are then calculated using the Bloch wave formulation introduced in Chapter 3. All calculations are performed on the unit cell (shaded region in Fig. 4.1), by making use of periodic boundary conditions. The longitudinal and shear modes are identified using a modal filter technique, and the modal bandgaps and anisotropic propagation properties are studied as a function of the applied pre-strain.

---

<sup>1</sup>Reproduced from B. M. Goldsberry and M. R. Haberman, “Negative stiffness honeycombs as tunable elastic metamaterials,” *J. Appl. Phys.*, vol. 123, no. 9, p. 091711, 2018, with the permission of AIP publishing. The present author derived and implemented the presented methods and created all figures.

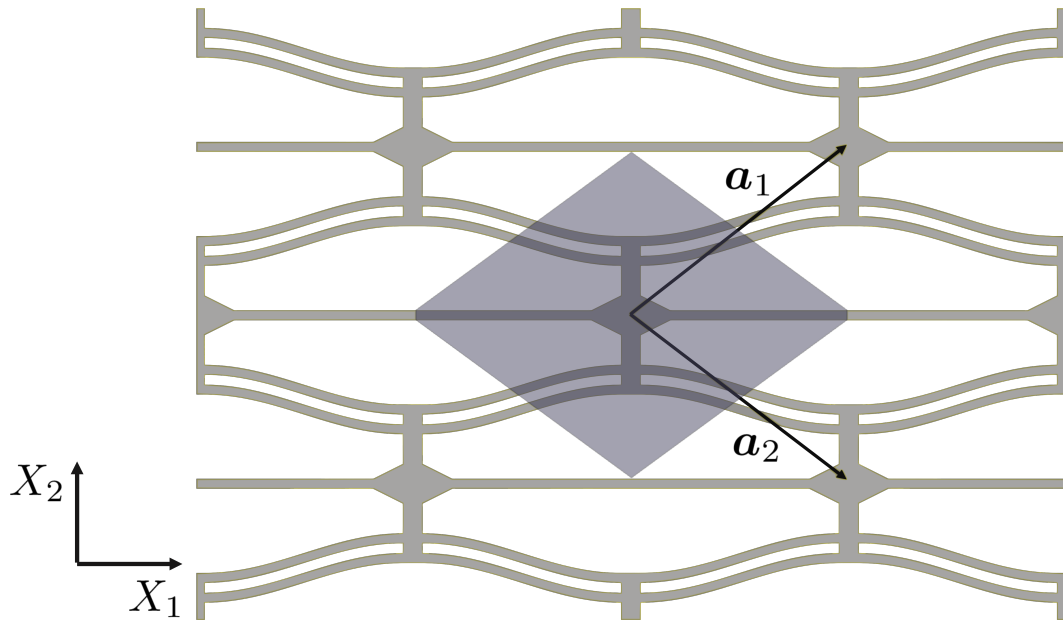


Figure 4.1: Negative stiffness honeycomb (NSH) metamaterial with the fundamental unit cell shaded and direct lattice vectors  $\mathbf{a}_1, \mathbf{a}_2$  (reproduced from Fig. 2.3 for convenience).

This chapter is organized as follows. The small-on-large approximation is introduced in Sec. 4.2, and the resulting nonlinear deformation model and elastic wave propagation model is derived. Finite element formulations for the dispersion curve computation and group velocity are presented. Section 4.3 shows the resulting dispersion curves in the irreducible Brillouin zone as a function of an applied external pre-strain, which uses a modal filter technique to identify modes on each dispersion branch. The tunability of the modal bandgaps and anisotropic properties are discussed, and it is shown that NSH exhibits metafluid behavior in a large frequency range.

## 4.2 Small-on-Large Approximation

The total displacement field  $\mathbf{u}_t$  in the NSH is assumed to be of the form

$$\mathbf{u}_t = \mathbf{u}_d + \mathbf{u}_a, \quad (4.1)$$

where  $\mathbf{u}_d$  is the displacement due to the pre-strain, and  $\mathbf{u}_a$  is the propagating acoustic wave, which is assumed to consist of small perturbations about the pre-strained displacement field, i.e.  $\|\mathbf{u}_a\|/\|\mathbf{u}_d\| \ll 1$ . This is the so-called “small-on-large” approximation, which allows for the computation of  $\mathbf{u}_d$  and  $\mathbf{u}_a$  in two sequential steps. First,  $\mathbf{u}_d$  is found by solving the nonlinear static equation for a given pre-strain applied to the lattice. Then,  $\mathbf{u}_a$  is computed using a linearized dynamic equation about the statically deformed state. A Lagrangian formulation is adopted in order use the same computational mesh for both modeling steps. Due to the periodicity of the lattice, only the dis-

placements within a unit cell need to be computed for both problems, which greatly reduces the computational complexity.

The theory described in Secs. 4.2.1, 4.2.2 is exact for pre-strain levels up to the point of instability [43]. Due to the geometric complexity, a finite element method is utilized for both the deformation and wave propagation studies. In this work, the open source code FEniCS is used to numerically perform the finite element algorithm [98,99]. To the present authors knowledge, current commercial finite element software do not have the ability to study Bloch wave problems in a pre-strained medium. FEniCS translates weak forms provided by the user into discrete matrices for linear algebra routines. Therefore, most of the theory in this section is dedicated to deriving the appropriate weak forms. The plane-strain approximation is used, reducing the computational domain to a two-dimensional surface.

#### 4.2.1 Deformation

Let  $\Omega \subset R^2$  be the material domain of a representative unit cell in the undeformed configuration with coordinate  $X$  and boundary  $\Gamma = \Gamma_p \cup \Gamma_i$ , where  $\Gamma_p$  are the shared boundaries between  $\Omega$  and the unit cell region in Fig. 2.3 and consists of the boundaries  $\Gamma_A^+$ ,  $\Gamma_A^-$ ,  $\Gamma_B^+$ ,  $\Gamma_B^-$ ,  $\Gamma_C^+$ ,  $\Gamma_C^-$  shown in Fig. 4.2, and  $\Gamma_i$  are the inner boundaries. Then, let  $\varphi(\mathbf{X})$  be the deformation mapping, such that the displacement field is defined as

$$\mathbf{u} = \varphi(\mathbf{X}) - \mathbf{X}. \quad (4.2)$$



The deformation gradient  $\mathbf{F}$  is then defined as

$$F_{ij} = \frac{\partial \varphi_i}{\partial X_j}. \quad (4.3)$$

An affine, uni-axial strain is applied to the NSH in the  $X_2$  direction by application of a macroscopic deformation gradient  $\bar{\mathbf{F}}$ , defined in matrix notation as [58]

$$\bar{F}_{ij} = \begin{bmatrix} 1 & 0 \\ 0 & 1 - \beta \end{bmatrix}, \quad (4.4)$$

where  $\beta$  is the macroscopic engineering pre-strain, and the macroscopic strain  $\bar{\mathbf{E}} = \bar{\mathbf{F}}^T \bar{\mathbf{F}} - \mathbf{I} = \beta^2/2 - \beta$  for  $\beta < 0$ . The microscopic deformation field is then given by the linear combination of the homogeneous deformation and a non-homogeneous deformation field  $\mathbf{w}(\mathbf{X})$  [43]

$$\boldsymbol{\varphi}(\mathbf{X}) = \bar{\mathbf{F}}\mathbf{X} + \mathbf{w}(\mathbf{X}). \quad (4.5)$$

The microscopic deformation gradient is therefore given by

$$\mathbf{F}(\mathbf{X}) = \bar{\mathbf{F}} + \nabla \mathbf{w}(\mathbf{X}). \quad (4.6)$$

The micro- to macroscopic mapping of the deformation gradient leads to a constraint on  $\mathbf{w}$  [43]

$$\int_{\Gamma_p} \mathbf{w} \otimes \mathbf{n} d\Gamma_p = 0, \quad (4.7)$$

where  $\mathbf{n}$  is the normal vector on the unit cell surface  $\Gamma_p$ . This constraint can be satisfied by requiring that  $\mathbf{w}$  satisfy periodic boundary conditions on the unit cell surfaces

$$\mathbf{w}(\mathbf{X}) \Big|_{\Gamma_r^+} = \mathbf{w}(\mathbf{X}) \Big|_{\Gamma_r^-}, \quad (4.8)$$

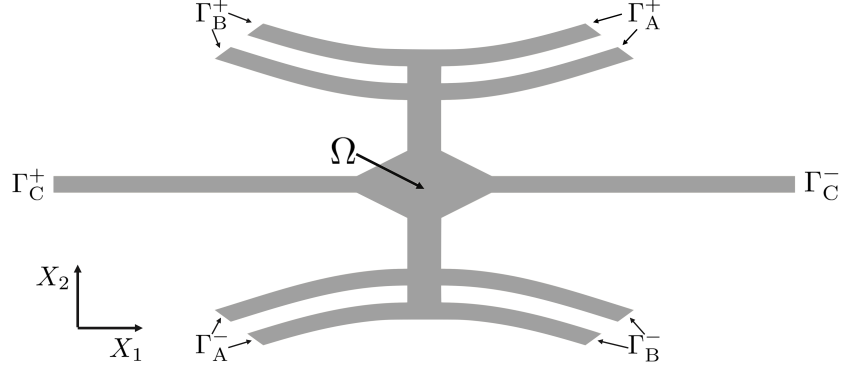


Figure 4.2: Computational domain,  $\Omega$ , of NSH. The boundary pairs  $(\Gamma_A^+, \Gamma_A^-)$ ,  $(\Gamma_B^+, \Gamma_B^-)$ ,  $(\Gamma_C^+, \Gamma_C^-)$  are the locations where periodic boundary conditions are applied to the computational domain.

where  $r = A, B, C$  and the surfaces are specified in Fig. 4.2.

A variational formulation suited for a finite element algorithm is then needed to solve for  $\mathbf{w}$ , which is derived using the principle of stationary potential energy, written in integral form as [100]

$$\Pi = \int_{\Omega} W(\mathbf{F}) d\Omega - \int_{\Gamma} \mathbf{t} \cdot \boldsymbol{\varphi} d\Gamma, \quad (4.9)$$

where  $\Pi$  is the total potential energy,  $W(\mathbf{F})$  is the strain energy density, and  $\mathbf{t}$  is the traction vector on the boundary. The interior boundaries  $\Gamma_i$  are assumed to be stress-free, and  $\mathbf{t}$  is assumed to be anti-periodic on  $\Gamma_p$ . Therefore, the boundary integral in Eq. (4.9) vanishes, leaving only the domain integral. The particular strain energy density function chosen in this work is the Saint Venant-Kirchhoff model, which takes into account the finite displacement but

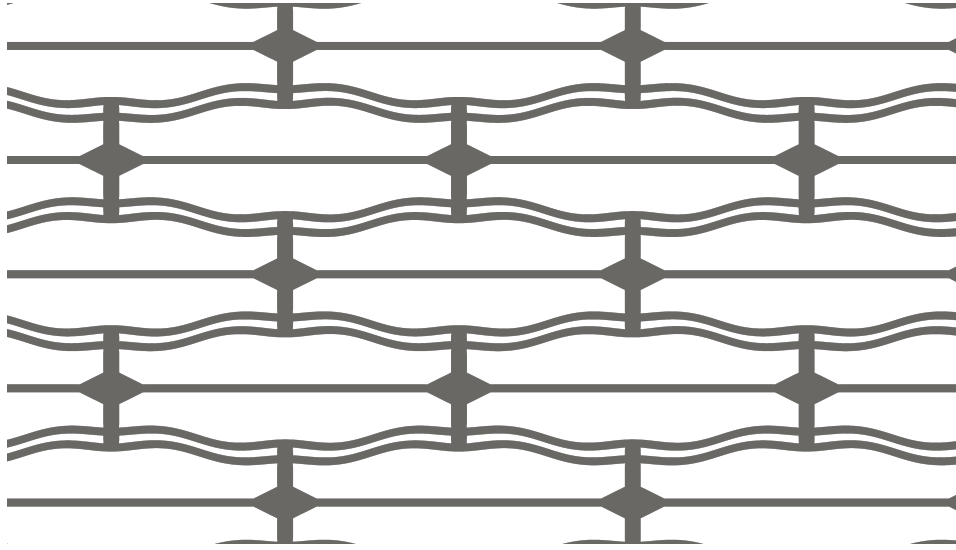


Figure 4.3: Deformation of the pre-strained lattice for  $\beta = 0.05$ .

assumes small local strain values, and is written as [101]

$$W = \frac{\lambda}{2} \text{tr}(\mathbf{E})^2 + \mu \text{tr}(\mathbf{E}^2), \quad (4.10)$$

$$\mathbf{E} = \frac{1}{2} (\mathbf{F}^T \mathbf{F} - \mathbf{I}), \quad (4.11)$$

where  $\lambda$  and  $\mu$  are the first and second Lamé parameters, respectively,  $\mathbf{E}$  is the Green strain tensor, and  $\mathbf{I}$  is the identity tensor. The use of this strain energy density function is acceptable for these lattices given the fact that NSH have been designed to undergo elastic buckling and repeatable large deformation behavior of these systems has been experimentally demonstrated [80, 82].

The equilibrium position is found by finding  $\mathbf{w}$  that minimizes Eq. (4.9). The minimum of  $\Pi$  can be found by defining a functional  $L$  that is equal to the directional derivative of  $\Pi$  with respect to an arbitrary vector  $\mathbf{v}$ , the so-called

test vector in finite elements, and finding the root:

$$L(\mathbf{w}; \mathbf{v}) = \left. \frac{d}{d\eta} \Pi(\mathbf{w} + \eta \mathbf{v}) \right|_{\eta=0} = 0, \quad \forall \mathbf{v} \in V, \quad (4.12)$$

where  $V$  is a suitable vector space with periodicity enforced. Equation (4.12) is discretized into a system of algebraic equations using FEniCS and Newton's method is used to find the root. This requires the Jacobian,  $J$ , which is defined as

$$J(\mathbf{w}; \delta \mathbf{w}, \mathbf{v}) = \left. \frac{d}{d\epsilon} L(\mathbf{w} + \epsilon \delta \mathbf{w}; \mathbf{v}) \right|_{\epsilon=0}, \quad (4.13)$$

where  $\delta \mathbf{w}$  is a virtual displacement vector. Figure 4.3 shows the displacement in the lattice for  $\beta = 0.05$ , which was solved using the approach described above.

#### 4.2.2 Elastic Wave Propagation

Once the displacement field  $\mathbf{u}_d$  is determined from the variational principles discussed above, the acoustic displacement  $\mathbf{u}_a$  is found by linearizing the nonlinear equations of motion about  $\mathbf{u}_d$ . One way of accomplishing this is the use of Lyapunov's indirect method, which results in a linear wave equation with non-constant coefficients [100]

$$(L_{ijkl} u_{k,l})_{,j} = \rho \frac{\partial^2 u_i}{\partial t^2}, \quad (4.14)$$

$$L_{ijkl} = \left. \frac{\partial^2 W}{\partial F_{ij} \partial F_{kl}} \right|_{\mathbf{u}=\mathbf{u}_d}, \quad (4.15)$$

where  $\mathbf{L}$  is a spatially-varying tensor known as the tangent modulus tensor, and  $\rho$  is the mass density, which is assumed to be uniform in the medium. Due

to the periodicity of the geometry and the coefficients  $\mathbf{L}$ , the Floquet theorem is utilized to restrict the computational domain to the representative unit cell [26]. The assumed form of the solution is thus given by

$$\mathbf{u}_a(\mathbf{X}) = \mathbf{U}(\mathbf{X})e^{i\mathbf{K}\cdot\mathbf{X}}, \quad (4.16)$$

where  $\mathbf{U}(\mathbf{X})$  is a periodic function of the unit cell, and  $e^{i\mathbf{K}\cdot\mathbf{X}}$  accounts for the phase change across each unit cell [26]. The weak form of Eq. (4.14) is derived by taking the Hermitian inner product of the left- and right- hand sides with a test vector  $\mathbf{v}$ , written as

$$\mathbf{v} = V^*(\mathbf{X})e^{-i\mathbf{K}\cdot\mathbf{X}}, \quad (4.17)$$

Application of Green's first identity then yields the following integral equation

$$\begin{aligned} \int_{\Omega} [L_{ijkl} (U_{k,l} V_{i,j}^* + K_l K_j U_k V_i^*)] d\Omega + i \int_{\Omega} [L_{ijkl} (U_k K_l V_{i,j}^* - U_{k,l} K_j V_i^*)] d\Omega \\ = \rho\omega^2 \int_{\Omega} U_i V_i^* d\Omega. \end{aligned} \quad (4.18)$$

#### 4.2.2.1 Dispersion Computation

Modes propagating in the NSH is then determined by discretizing Eqn. (4.18) into a system of equations, resulting in the matrix system

$$\mathbf{A}(\mathbf{K})\mathbf{U} = \omega^2\mathbf{B}\mathbf{U}, \quad (4.19)$$

where the stiffness matrix  $\mathbf{A}$  is a Hermitian matrix that is a function of the wavenumber  $\mathbf{K}$ , and the mass matrix  $\mathbf{B}$  is positive-definite. Iso-frequency surfaces  $\omega(k_x, k_y)$  are generated by treating Eq. (4.19) as a generalized eigenvalue

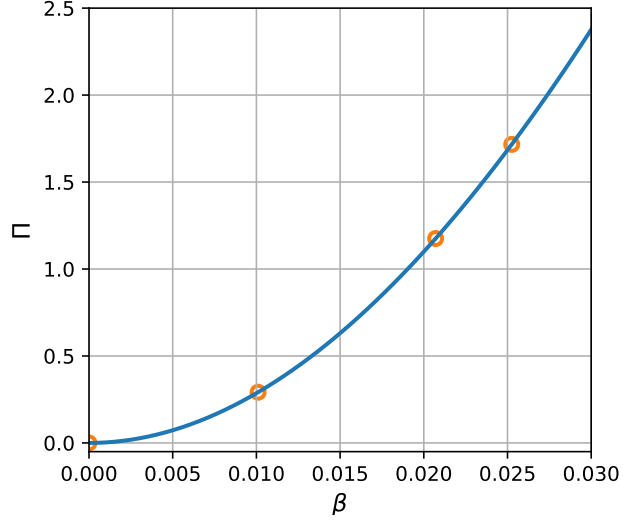


Figure 4.4: Total potential energy within the unit cell as a function of the pre-strain. The points represent where the wave propagation is studied and reported in Sec. 4.3.

problem, where  $\omega_n^2$  and  $\mathbf{U}_n$  are the eigenvalues and eigenvectors, respectively. For slowness and group velocity calculations, it is more useful to specify the frequency  $\omega$  and calculate all wave vectors that exist as is shown in the following paragraph.

Let the wavenumber be expressed in polar form

$$\mathbf{K} = \|\mathbf{K}\|[\cos(\theta) \sin(\theta)]^T, \quad (4.20)$$

where  $\theta$  is the direction of propagation and  $\|\mathbf{K}\|$  is the wavenumber magnitude.

Equation (4.19) can then be rewritten as:

$$q^2\mathbf{M}\mathbf{U} + q\mathbf{C}\mathbf{U} + \mathbf{K}\mathbf{U} = 0, \quad (4.21)$$

where  $q = i\|\mathbf{K}\|$ , and

$$\begin{aligned} \mathbf{M} = & \cos^2(\theta) \int_{\Omega} L_{i0k0} U_k V_i^* d\Omega + \sin^2(\theta) \int_{\Omega} L_{i1k1} U_k V_i^* d\Omega \\ & + \sin(\theta) \cos(\theta) \left[ \int_{\Omega} L_{i0k1} U_k V_i^* d\Omega + \int_{\Omega} L_{i1k0} U_k V_i^* d\Omega \right], \quad (4.22) \end{aligned}$$

$$\begin{aligned} \mathbf{C} = & \cos(\theta) \int_{\Omega} [L_{ijk0} U_k V_{i,j}^* - L_{i0kl} U_{k,l} V_i^*] d\Omega \\ & + \sin(\theta) \int_{\Omega} [L_{ijk1} U_k V_{i,j}^* - L_{i1kl} U_{k,l} V_i^*] d\Omega, \quad (4.23) \end{aligned}$$

$$\mathbf{K} = - \int_{\Omega} L_{ijkl} U_{k,l} V_{i,j}^* d\Omega + \rho\omega^2 \int_{\Omega} U_i V_i^* d\Omega. \quad (4.24)$$

The 0 and 1 subscripts in the above equations are to separate the  $k_x$  and  $k_y$  components of the sum in Eq. (4.18). Equation (4.21) is a quadratic eigenvalue problem for  $q$ , and can be solved by specifying  $\omega$  and  $\theta$ . The matrices in Eq. (4.19) and Eq. (4.21) are large and sparse. Therefore, it is not practical to solve for all eigenfrequencies and eigenvectors. The software library SLEPc [102] (the Scalable Library for Eigenvalue Problem Computations) is used to perform the calculations, where a Krylov-schur method is used to calculate the eigenfrequencies and eigenvectors of Eq. (4.19), and a two-level orthogonal Arnoldi (TOAR) algorithm is used to calculate the eigenfrequencies and eigenvectors of Eq. (4.21). For both methods, a shift-and-invert transformation is used to extract eigenfrequencies near a target magnitude value.

#### 4.2.2.2 Group Velocity

Once  $\omega_n$  and  $\mathbf{U}_n$  are obtained by solving Eq. (4.19), the group velocity vector  $\mathbf{c}_g$ , with components

$$\mathbf{c}_{g,x} = \frac{\partial \omega}{\partial k_x}, \quad (4.25)$$

$$\mathbf{c}_{g,y} = \frac{\partial \omega}{\partial k_y}, \quad (4.26)$$

can be computed by taking the derivative of Eq. (4.14) with respect to  $k_x$  and  $k_y$ . The group velocity components are then given by [103]

$$\mathbf{c}_{g,x} = \frac{\mathbf{U}_n^H \mathbf{A}_{,k_x} \mathbf{U}_n}{2\omega_n}, \quad (4.27)$$

$$\mathbf{c}_{g,y} = \frac{\mathbf{U}_n^H \mathbf{A}_{,k_y} \mathbf{U}_n}{2\omega_n}, \quad (4.28)$$

where  $\mathbf{A}_{,k_x}$  and  $\mathbf{A}_{,k_y}$  are the derivatives of the stiffness matrix with respect to the components of the wavenumber, which are given by

$$\begin{aligned} \mathbf{A}_{,k_x} = & 2k_x \int_{\Omega} L_{i0k0} U_k V_i^* d\Omega \\ & + k_y \left[ \int_{\Omega} L_{i0k1} U_k V_i^* d\Omega + \int_{\Omega} L_{i1k0} U_k V_i^* d\Omega \right] \\ & + i \int_{\Omega} [L_{ijk0} U_k V_{i,j}^* - L_{i0kl} U_{k,l} V_i^*] d\Omega, \quad (4.29) \end{aligned}$$



Parameter	Description	Value
$L_x$	Horizontal length	55.88
$L_y$	Vertical length	43.18
$t_b$	Beam thickness	1.27
$t_s$	Beam separation	1.27
$h_b$	Beam apex height	5.08
$h_c$	Center height	1.90
$w_c$	Center width	3.8
$h_{cb}$	Center beam height	3.8
$w_{cb}$	Center beam width	2.54
$t_{hb}$	Horizontal beam thickness	1.27

Table 4.1: Geometric parameter values depicted in Fig. 2.4. All values are in mm.

and

$$\begin{aligned}
\mathbf{A}_{,k_y} = & 2k_y \int_{\Omega} L_{i1k1} U_k V_i^* d\Omega \\
& + k_x \left[ \int_{\Omega} L_{i0k1} U_k V_i^* d\Omega + \int_{\Omega} L_{i1k0} U_k V_i^* d\Omega \right] \\
& + i \int_{\Omega} [L_{ijk1} U_k V_{i,j}^* - L_{i1kl} U_{k,l} V_i^*] d\Omega. \quad (4.30)
\end{aligned}$$

### 4.3 Results

In this work, a NSH with geometric parameters given in Table 4.1 is investigated. The NSH is made of Nylon 11, with material properties shown in Table 4.2 [80]. Bloch wave solutions are found for four pre-strain values,  $\beta = 0.0, 0.0101, 0.0207, 0.0252$ , which are illustrated in Fig. 4.4. These pre-

Property	Value	Unit
Density	1040	kg/m <sup>3</sup>
Poisson's ratio	0.33	-
Young's modulus	1582	MPa

Table 4.2: Material properties of NSH

strains were chosen such that the elastic wave propagation was stable for all wavenumbers. For higher pre-strain values, wave propagation may be unstable for one or more wavenumbers and thus is not considered. For each pre-strain, the tangent modulus tensor in Eq. (4.15) is computed, and the Bloch modes and natural frequencies are found by specifying the wave vector  $\mathbf{K}$  in the irreducible Brillouin zone and solving Eq. (4.19). To give insight on the physical vibration of the lattice, the modes are categorized into either a longitudinal, transverse, or higher order mode (H.O.M.). Once categorized, the modes can be tracked as a function of pre-strain, giving insight into the tunability of the phase speed of each mode, the allowable directions of wave propagation, and the direction of the propagation of energy carried by each mode.

### 4.3.1 Modal Characterization

The modes in the low wavenumber regime (near the  $\Gamma$  point) represent propagating plane waves whose wavelengths are very large when compared to the dimensions of the lattice. At the unit cell level, these modes correspond to the bulk motion of the unit cell moving either parallel to the wave front (longitudinal), perpendicular to the wavefront (transverse), or out-of-phase

with neighboring unit cells (higher order modes). For a wave vector in this regime with a propagation angle of  $\theta$  and a small but finite magnitude  $\delta k$ , these modes form a complete mass-orthogonal set  $[\mathbf{U}_{\Gamma,0}(\theta) \mathbf{U}_{\Gamma,1}(\theta) \cdots \mathbf{U}_{\Gamma,N}(\theta)]$ , where the subscript  $\Gamma$  corresponds to modes near  $\Gamma$ , and are a function of the propagation direction, and  $N$  is the total number of degrees of freedom in the finite element model. In this work,  $\delta k = 0.01$  is chosen to ensure good separation of the longitudinal and transverse modes. Any mode  $\phi$  at a larger wavenumber in the first Brillouin zone in the direction  $\theta$  can be decomposed into a sum of  $\Gamma$ -point modes

$$\phi = \sum_{i=0}^N c_i \mathbf{U}_{\Gamma,i}, \quad (4.31)$$

where  $c_i$  are the modal coefficients. These coefficients are determined using the mass-orthogonality of the  $\Gamma$ -point modes using the relation

$$c_i = \mathbf{U}_{\Gamma,i}^T \mathbf{M} \phi. \quad (4.32)$$

For the results presented below, the classification of  $\phi$  is made using the  $\Gamma$  mode with the highest modal coefficient.

### 4.3.2 Dispersion

Figure 4.5(a) shows the dispersion branches on the outline of the irreducible Brillouin zone in Fig. 2.6 (repeated here in Fig. 4.6 for convenience) for the undeformed configuration ( $\beta = 0$ ). The mode on each branch is categorized using the modal decomposition technique discussed in Sec. 4.3.1. From Fig. 4.5(a) it is evident that the mode categorization is not constant on a

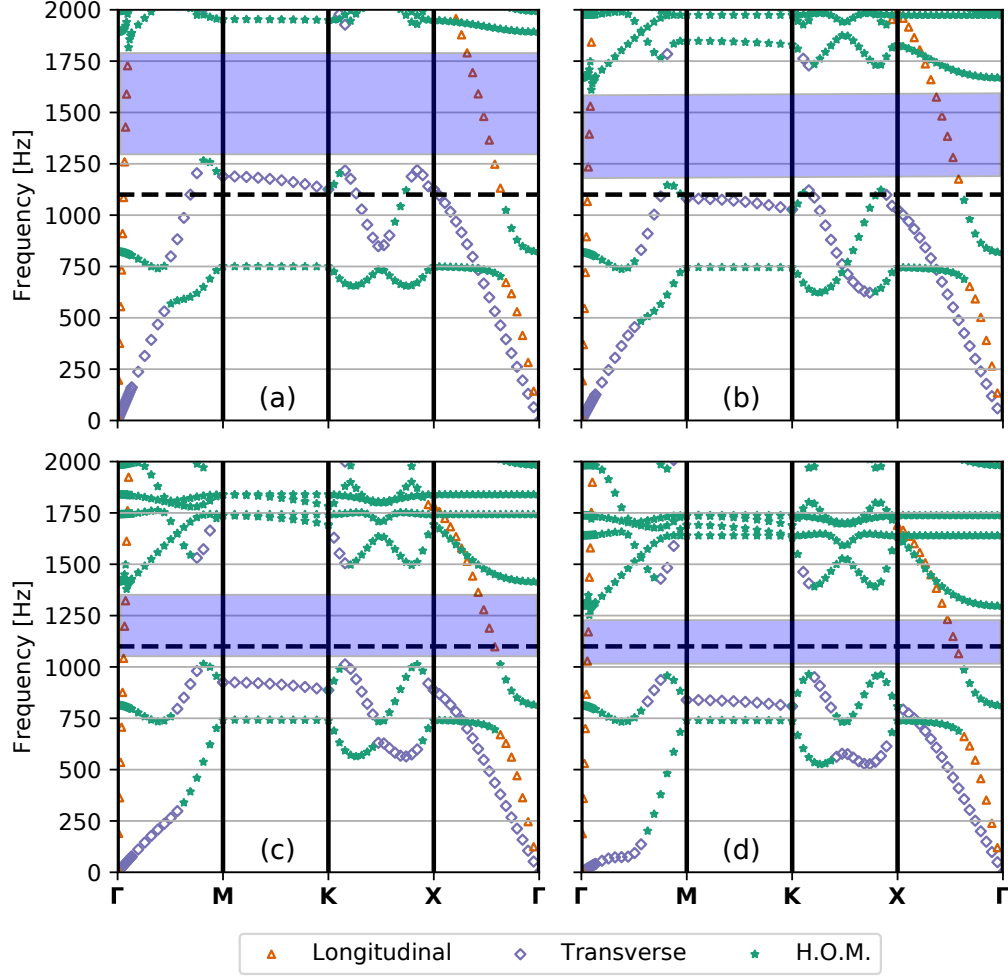


Figure 4.5: Mode dispersion in the irreducible Brillouin zone for: (a)  $\beta = 0$  (undeformed configuration), (b)  $\beta = 0.0101$ , (c)  $\beta = 0.0207$ , (d)  $\beta = 0.0252$ . The shaded regions indicate frequency ranges where only unimodal longitudinal wave motion is permitted in the lattice.

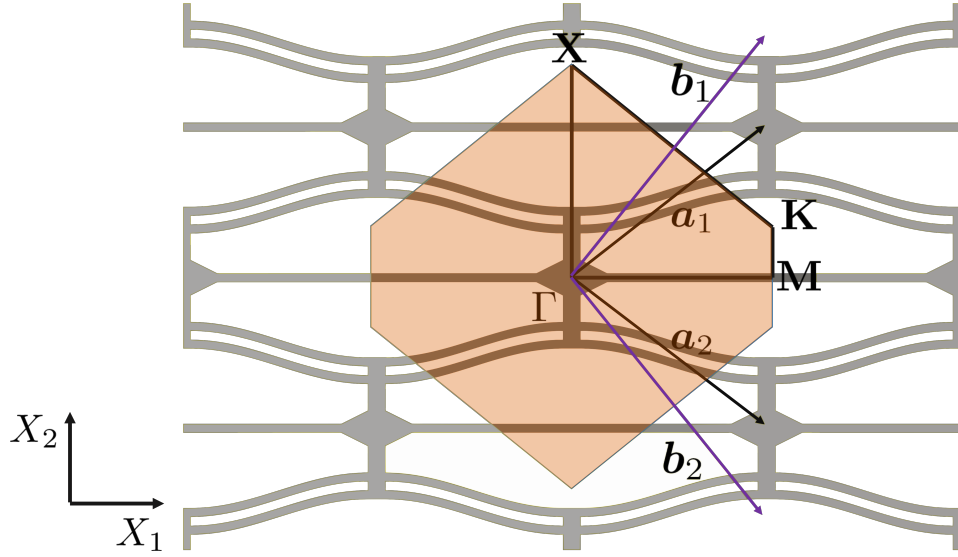


Figure 4.6: The first Brillouin zone, defined with basis vectors  $\mathbf{b}_1, \mathbf{b}_2$ . The irreducible Brillouin zone is traced in black (Reproduced from Fig. 2.6 for convenience.)

branch. This is due to mode coupling when two branches interact, which is common in an anisotropic media with high wavenumbers [104]. Figures 4.5(b)-4.5(d) show the evolution of the dispersion curves as the pre-strain is increased. Overall, all branches decrease in frequency which is indicative of a strain-softening material, which is expected for NSH materials based on both models and experimental observations. The result is that the effective phase speeds of each mode is reduced for increasing pre-strain. The most apparent changes are the decrease of the high-frequency higher order mode branches to a lower frequency range. The modes whose motion is parallel to the pre-strain loading direction are the most sensitive to the pre-strain, due to the decrease in the effective stiffness of the transversely-loaded beam-like elements. This

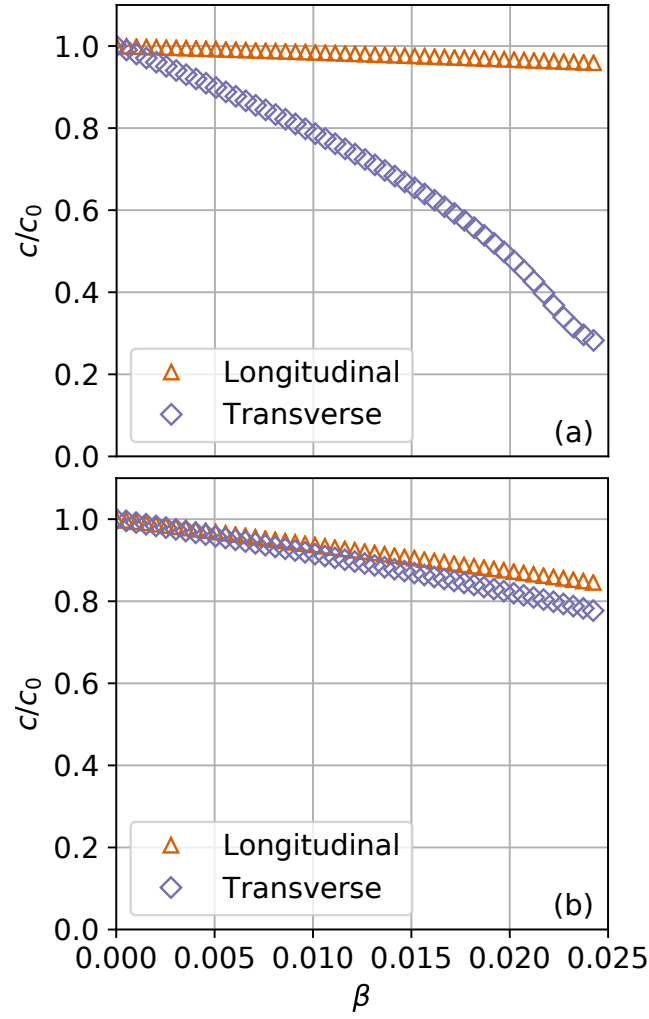


Figure 4.7: Ratio of the phase speed over the phase speed of the undeformed configuration at 200 Hz for longitudinal and transverse waves as a function of the external pre-strain  $\beta$  in the: (a)  $X_1$  direction, (b)  $X_2$  direction.

behavior is most noticeable with the transverse mode in the  $X_1$  direction, whose displacement is parallel to the pre-strain loading. In addition, the longitudinal mode in the  $X_2$  direction (whose displacement is also parallel to the pre-strain) is more sensitive to the pre-strain than the longitudinal mode in the  $X_1$  direction. This can be seen by examining the ratio of the modal phase speed at a pre-strain level over the phase speed in the undeformed configuration at a set frequency. Figure 4.7(a) shows this in the  $X_1$  direction at a frequency of 200 Hz, and Fig. 4.7(b) shows this with the same frequency in the  $X_2$  direction. Indeed, the transverse wave phase speed in the  $X_1$  direction changes by about 80% from the undeformed state to a pre-strain of 0.025, while the longitudinal wave only changes 4% over the same pre-strain range. The modal phase speeds in the  $X_2$  direction exhibit a change of approximately 20% for the same range of pre-strains. Note that the transverse mode in the  $X_2$  direction is also sensitive to the pre-strain, even though the motion is perpendicular to the loading direction. It is interesting to note that the longitudinal mode in the  $X_1$  direction is the least sensitive of all modes. Also of significant interest is that for certain frequency ranges only unimodal longitudinal wave motion is permitted in the lattice. For these frequency ranges, the lattice acts as a pentamode elastic material, or meta-fluid [22]. The frequency range where this meta-fluid behavior occurs changes with pre-strain as discussed in Sec. 4.3.3. The evolution of NSH anisotropy can be examined by investigating the slowness contours at a set frequency, which is calculated from the following

relationships

$$c_x^{-1} = \frac{k_x}{\omega}, \quad (4.33)$$

$$c_y^{-1} = \frac{k_y}{\omega}. \quad (4.34)$$

Figure 4.8(a) shows the slowness contours for the first three propagating modes in the first Brillouin zone for the undeformed configuration at a frequency of 1100 Hz. A horizontal dashed line at that frequency is provided for reference in Fig. 4.5. The undeformed configuration exhibits directional wave propagation at this frequency, namely the higher order branches are confined to propagate in directions nearly parallel to the  $X_2$  direction while the transverse modes propagate at all angles except approximately  $[32^\circ 78^\circ]$ ,  $[102^\circ 148^\circ]$ ,  $[212^\circ 258^\circ]$ , and  $[282^\circ 328^\circ]$ . As the pre-strain is increased to  $\beta = 0.0101$ , shown in Fig. 4.8(b), the higher order modes can propagate in the  $X_1$  direction, while the transverse mode can no longer propagate in the  $X_2$  direction. Note that in Fig. 4.8, the longitudinal mode is very insensitive to pre-strain. The normal vector to these slowness curves specifies the magnitude and direction of the group velocity, which is the direction of energy propagation, and is shown in Fig. 4.9. Figure 4.9(a) shows that pre-strain has little effect on the energy propagation of the longitudinal modes as pre-strain is increased. However, the group velocity does become slower in the  $X_2$  direction. Figure 4.9(b) is the transverse and higher order modes for the undeformed configuration. For this frequency, the shear waves carry energy in all directions, while higher order modes only carry energy near the  $X_2$  direction. When a pre-strain of



$\beta = 0.0101$  is applied, the higher order modes can now carry energy in the  $X_1$  direction, while the transverse mode can no longer carry energy in the  $X_2$  direction.

### 4.3.3 Meta-Fluid Behavior

The mode that is least sensitive to the pre-strain is the longitudinal mode. Because of this, the lattice can act as a meta-fluid for a specific range of frequencies and pre-strains in all directions. In the undeformed state, a meta-fluid region exists between approximately 1250 to 1750 Hz, shown in Fig. 4.5(a). As pre-strain is applied, the center frequency and bandwidth of this region decreases, as shown in Figs. 4.5(b)-(d). The existence of meta-fluid behavior at all directions is confirmed by the slowness curve in Fig. 4.8(c). Pre-strained NSH can therefore mimic pentamode metamaterials, which are of interest for application of concepts from transformation acoustics such as acoustic cloaking [10] and impedance-match gradient index lenses [22]. In addition, the frequencies where this occurs as well as the degree of anisotropy can be tuned through the design of the unit cell and the pre-strain level, which will be reserved for future research.

## 4.4 Conclusion

In this chapter, a negative stiffness honeycomb is investigated as a potential elastic wave metamaterial that can be tuned through mechanical deformation. A small-on-large formulation is employed to model the total

displacement in the NSH, which requires the solution of two sequential problems. First, the unit cell deformation due to an applied uni-axial pre-strain is computed. Once the new equilibrium configuration is found, a linearized wave equation about this equilibrium point is solved using a Bloch wave formulation, which yields the modes and frequencies of propagation. Due to the geometric complexity of the unit cell, a finite element method using the FEniCS code was utilized for both solution steps.

This lattice was shown to exhibit a large degree of tunability without requiring large pre-strains or strains that approach buckling instability configurations. The high-frequency higher order modes and the transverse mode in the  $X_1$  direction were the most sensitive to the pre-strain. However, the longitudinal and transverse modes in the  $X_2$  direction did exhibit a change of phase speeds of around 20%. In addition to the modal phase speeds, the direction of propagation for each mode was analyzed by investigating the slowness contours at a frequency of interest. The direction of energy propagation was inspected at the same frequency by calculating the group velocity. It was shown that the transverse and optical modes were highly directional, and their direction of propagation can be tuned by changing the pre-strain amount. In contrast, the longitudinal modes propagated at all angles and was not sensitive to the applied pre-strain. One of the most interesting aspects of this NSH is its ability to act as a meta-fluid, supporting only longitudinal wave motion at all angles of propagation within a frequency band, which can be tuned with the pre-strain amount. NSH can therefore mimic pentamode metamaterials

in select frequency bands, which can be used in applications where an elastic material must be efficiently impedance-matched to an exterior fluid, such as an acoustic cloak or an elastic gradient index lens. The ability to tailor the geometric parameters and pre-strain amount, as well as its ability to recover to the initial configuration when unloaded, makes NSH a versatile metamaterial that can be used in numerous applications.

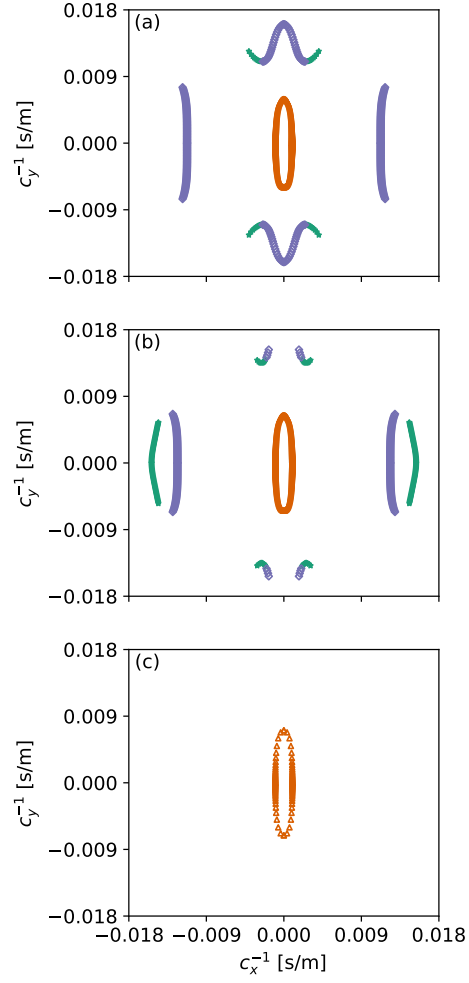


Figure 4.8: Slowness curves for 1100 Hz at a pre-strain of: (a)  $\beta = 0$  (undeformed configuration), (b)  $\beta = 0.0101$ , (c)  $\beta = 0.0207$ .

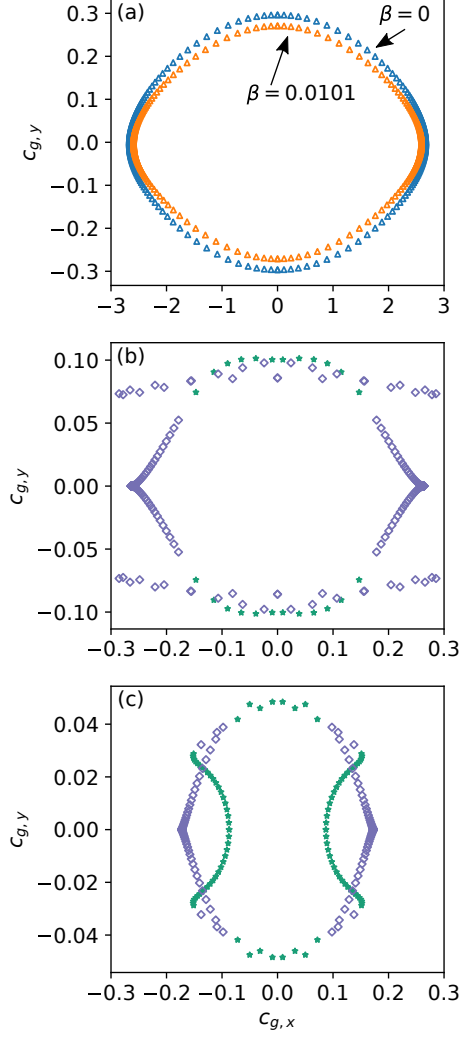


Figure 4.9: Group velocity at 1100 Hz. (a) Group velocity of the longitudinal mode for  $\beta = 0$  and  $\beta = 0.0101$ . The color scheme differs from the previous figures and serves to denote the two pre-strain solutions. The triangle symbol, which represents the longitudinal mode, is still preserved. (b) Group velocity of the transverse and higher order modes for  $\beta = 0$ . (c) Group velocity of the transverse and higher order modes for  $\beta = 0.0101$ .

## Chapter 5

# Non-reciprocal Wave Propagation in Mechanically-Modulated Continuous Elastic Metamaterials

### 5.1 Introduction

In this chapter, the finite element approach from Chapter 4 is generalized to study non-reciprocal wave propagation in NSH. The “small-on-large” approximation is rederived from Chapter 4 to include the effects of a spatiotemporally-varying pre-strain. The generalized Bloch wave solution form discussed in Sec. 3.4 is then applied to the resulting linear elastic wave equation to obtain the frequency-wavenumber spectrum for modes of interest and compared with prior works. The generality of the finite element approach is then demonstrated by investigating the changes in the frequency-wavenumber spectrum when geometric asymmetry is introduced. This method provides a framework for modeling non-reciprocal waves in spatiotemporally modulated media when simple, analytical models are not feasible.

This chapter is organized as follows. The small-on-large approximation is revisited in Sec. 4.2 to include the effects of a spatiotemporally-varying pre-strain. The conditions for which this approximation holds is then detailed. The weak forms necessary for the implementation of the finite element method are

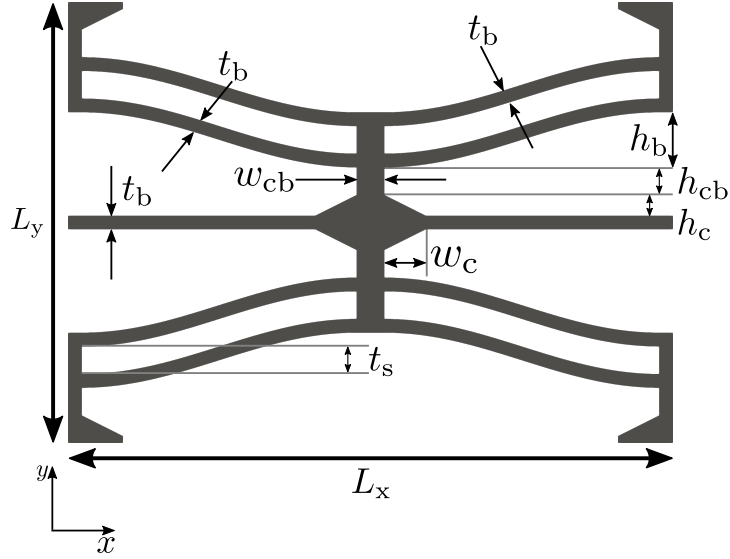


Figure 5.1: Negative stiffness element with geometric parameters.

then derived in Sec. 5.3 using the techniques outlined in Chapter 3. In Sec. 5.4, the derived finite element approach is benchmarked with known solutions to a thin Kirchhoff plate, and the degree of non-reciprocity for longitudinal and transverse waves in a negative stiffness chain, a quasi-one-dimensional chain composed of negative stiffness elements, is investigated. The effects of geometric asymmetry on the degree of non-reciprocity of the longitudinal and transverse modes are then explored. This chapter then concludes in Sec. 5.5 with final remarks.

## 5.2 Theory

In this section, the small-on-large approximation is rederived from Chapter 4 for elastic waves in a general time-varying pre-strained medium

[105]. As in Chapter 4, the plane-strain approximation is assumed, reducing the material dynamics to two dimensions. To simplify the computational modeling and to easily observe non-reciprocity, a quasi-one-dimensional chain of negative stiffness elements (termed negative stiffness chain hereafter) is considered, whose unit cell is the rectangular unit cell depicted in Fig. 2.4 and is reproduced for convenience in Fig. 5.1. In order to capture the spatially varying pre-strain, a supercell must be modeled, which is constructed by repeating the unit cell in Fig. 5.1 along the  $x$  direction, as shown in Fig. 5.2(a). While the negative stiffness chain is considered here as a case example, this method can be applied to any material structure of interest using the methods developed in this chapter.

### 5.2.1 Small-On-Large Theory Revisited

The following equations of motion and tensor definitions are repeated here for convenience. Let  $\Omega \in \mathcal{R}^2$  be the material domain of a representative supercell in the undeformed configuration with coordinate  $\mathbf{X} = [x, y]^T$ . The equations of motion with respect to the reference configuration for the elastic medium are

$$\text{Div } \mathbf{S} = \rho_0 \frac{\partial^2 \mathbf{u}}{\partial t^2}, \quad (5.1)$$

where  $\mathbf{u}$  is the displacement,  $\rho_0$  is the density, and  $\mathbf{S}$  is the first Piola-Kirchhoff stress tensor.  $\mathbf{S}$  is related to the strain energy density function,  $W$ , by

$$\mathbf{S} = \frac{\partial W}{\partial \mathbf{F}}, \quad (5.2)$$



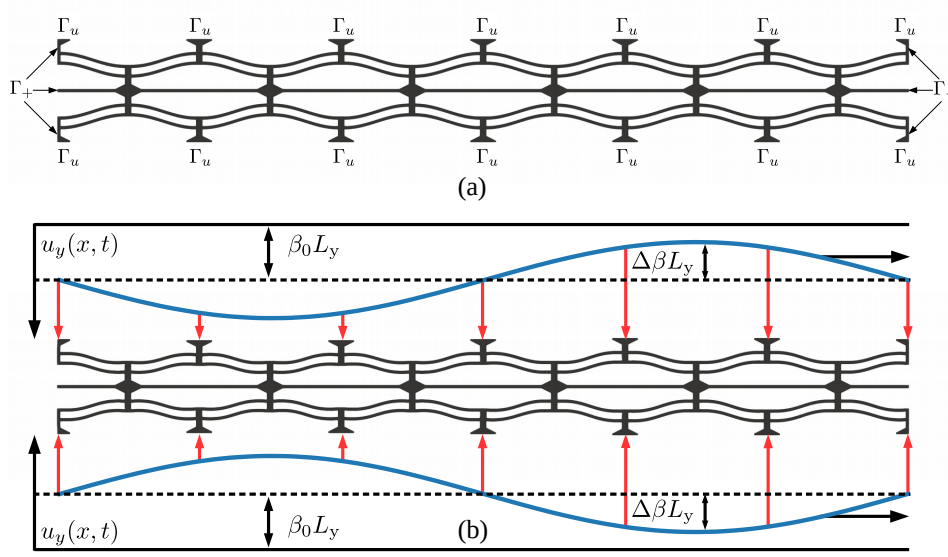


Figure 5.2: (a) Supercell computational domain with displacement boundaries  $\Gamma_u$  and periodic boundary pairs  $(\Gamma^+, \Gamma^-)$ . (b) Nonlinear deformation of the negative stiffness chain due to the external pre-strain  $\beta(x, t)$  with parameters  $\beta_0 = 0.01$  and  $\Delta\beta = 0.3\beta_0$ . The external pre-strain is applied as displacement boundary conditions on the faces depicted by the arrows. The applied displacement in the  $y$  direction,  $u_y(x, t)$ , are composed of a static displacement term denoted by the dashed line whose value is  $\beta_0 L_y$ , and an oscillating component depicted by the sine wave with amplitude  $\Delta\beta L_y$  (not drawn to scale).

where  $\mathbf{F}$  is the deformation gradient, which is defined in relation to the displacement as

$$\mathbf{F} = \frac{\partial \mathbf{u}}{\partial \mathbf{X}} + \mathbf{I}, \quad (5.3)$$

where  $\mathbf{I}$  is the identity tensor. As in Ch .4, the particular strain energy density function is chosen to be the St. Venant-Kirchhoff model, which accounts for finite displacements but assumes small local strain values, and is written as [101]

$$W = \frac{\lambda}{2} \text{tr}(\mathbf{E})^2 + \mu \text{tr}(\mathbf{E}^2), \quad (5.4)$$

$$\mathbf{E} = \mathbf{F}^T \mathbf{F} - \mathbf{I}, \quad (5.5)$$

where  $\lambda$  and  $\mu$  are the first and second Lamé parameters of the elastic medium, respectively, and  $\mathbf{E}$  is the Green-Lagrangian strain tensor.

The total displacement  $\mathbf{u}$  is assumed to be of the form

$$\mathbf{u}(\mathbf{X}, t) = \mathbf{u}_d(\mathbf{X}, t) + \mathbf{u}_a(\mathbf{X}, t), \quad (5.6)$$

where  $\mathbf{u}_d$  is the displacement due to the external pre-strain, and  $\mathbf{u}_a$  is the displacement field associated with the propagating elastic wave, which can be thought of as a perturbation, or incremental motion, about  $\mathbf{u}_d$ . The deformation gradient can thus be decomposed by substituting Eq.(5.6) into Eq.(5.3), which yields

$$\mathbf{F} = \mathbf{F}_d + \mathbf{F}_a, \quad (5.7)$$

where  $\mathbf{F}_d$  is the geometrically nonlinear deformation gradient due to the external pre-strain and is written as

$$\mathbf{F}_d = \frac{\partial \mathbf{u}_d}{\partial \mathbf{X}} + \mathbf{I}, \quad (5.8)$$

and  $\mathbf{F}_a$  is the deformation gradient due to the elastic wave motion, which is found to be

$$\mathbf{F}_a = \frac{\partial \mathbf{u}_a}{\partial \mathbf{X}}. \quad (5.9)$$

The first Piola-Kirchhoff stress tensor can be approximated as a Taylor series expansion about the pre-strained state

$$\mathbf{S} \approx \mathbf{S}_d + \mathbf{S}_a, \quad (5.10)$$

where  $\mathbf{S}_d = \mathbf{S}(\mathbf{F}_d)$  is the stress due to the external pre-strain, and the incremental stress  $\mathbf{S}_a$  can be written in index notation as

$$(S_a)_{ij} = L_{ijkl}(F_a)_{kl}, \quad (5.11)$$

where  $L_{ijkl}$  is the fourth-order tangent modulus tensor, which is defined for any given value of initial deformation as

$$L_{ijkl} = \left. \frac{\partial^2 W}{\partial F_{ij} \partial F_{kl}} \right|_{\mathbf{u}=\mathbf{u}_d}. \quad (5.12)$$

Equation (5.1) can therefore be decomposed into the deformation and incremental terms using Eqns. (5.6) and (5.10) to yield a set of differential equations for the nonlinear deformation due to an external pre-strain,

$$\text{Div } \mathbf{S}_d = \rho_0 \frac{\partial^2 \mathbf{u}_d}{\partial t^2}, \quad (5.13)$$

and for the linear elastic wave propagation

$$\text{Div}(\mathbf{L}\nabla\mathbf{u}_a) = \rho_0 \frac{\partial^2 \mathbf{u}_a}{\partial t^2}. \quad (5.14)$$

In the presence of spatiotemporally-modulated pre-strain, Eq. (5.14) is a wave equation with non-constant coefficients that are functions of space and time. The deformation due to an external pre-strain therefore acts as an effective stiffness change relative to the reference configuration that can be tuned by selection of the lattice geometry and the externally imposed initial deformation.

### 5.2.2 Applied Deformation (Large Wave)

The displacement field due to an applied pre-strain is modeled using Eq. (5.13). The applied pre-strain,  $\beta$ , is assumed to have the following periodic traveling wave form

$$\beta(x, t) = \Delta\beta \sin(k_m x - \omega_m t) + \beta_0, \quad (5.15)$$

where  $\beta_0$  is the static pre-strain,  $\Delta\beta$  is the amplitude of the strain modulation,  $k_m = 2\pi/\lambda_m$  is the modulation wavenumber with wavelength  $\lambda_m$ , and  $\omega_m$  is the modulation angular frequency. For computational simplicity, the modulation wavelength  $\lambda_m$  is restricted to be equal to an integer number of unit cells. In this work, a supercell composed of six unit cells is considered, such that the supercell length and modulation wavelength are  $\lambda_m = 6L_X$ . This restriction limits the Bloch wavelengths to be  $\geq 6L_X$  in the acoustic branches within the first Brillouin zone. The computational geometry is shown in Fig. 5.2(a), with

boundaries  $\Gamma_u$  indicating where the external pre-strain is applied via displacement boundary conditions, and the boundary pairs  $(\Gamma_+, \Gamma_-)$  indicating where periodic boundary conditions are applied. The displacements on the top and bottom faces are  $\mathbf{u}_d = (0, -L_y\beta)$  and  $\mathbf{u}_d = (0, L_y\beta)$ , respectively. The resulting deformation of the lattice due to the applied pre-strain with parameters  $\beta_0 = 0.01$  and  $\Delta\beta = 0.3\beta_0$  at one instant in time is shown in Fig. 5.2(b). Note that the static pre-strain value has been chosen to place the elements of the negative stiffness chain into a strain state where small perturbations will lead to sufficiently significant variations in the local tangent modulus without approaching the point of instability. Further, the magnitude of the traveling modulation strain is small, 0.3% strain relative to the un-deformed configuration, and thus the effects on reciprocity reported here are associated with a small mechanical modulation leading to observable asymmetry of elastic wave propagation. The sine wave depicted in Fig. 5.2(b) represents Eq. (5.15), and the arrows indicate where the displacements are applied. The external pre-strain then translates with time in the positive  $x$  direction according to the imposed modulation speed  $c_m = \omega_m/k_m$ .

The numerical modeling is greatly simplified and the displacement solutions are guaranteed to be periodic in time and space by requiring that there is significant separation of time scales [44]. This is achieved by requiring the pre-strain modulation speed,  $c_m$ , to be slow with respect to the slowest material sound speed in the medium (shear wave speed). To investigate the consequences of a slow modulation, it is illustrative to rewrite Eq. (5.13)

as a non-dimensional equation. By choosing the normalization  $\bar{\mathbf{X}} = k_m \mathbf{X}$ ,  $\bar{\mathbf{u}}_d = \mathbf{u}_d/U$ ,  $\bar{\mathbf{S}}_d = \mathbf{S}_d/(\mu U k_m)$ ,  $\bar{t} = \omega_m t$ , Eq. (5.13) is rewritten as

$$\text{Div } \bar{\mathbf{S}}_d = \gamma \frac{\partial^2 \bar{\mathbf{u}}_d}{\partial \bar{t}^2}, \quad (5.16)$$

where  $U = \beta_0 L_y$  is a reference displacement,  $\gamma = c_m^2/c_s^2$  provides a measure of the modulation speed to the shear wave speed in the bulk material from which the negative stiffness chain is fabricated, and  $c_s = \sqrt{\mu/\rho_0}$  is the shear wave speed of the material. If the modulation speed is much slower than the shear wave speed ( $\gamma \ll 1$ ), the inertial term can be discarded and Eq. (5.13) simplifies to

$$\text{Div } \mathbf{S}_d = 0. \quad (5.17)$$

Solutions for  $\mathbf{u}_d(\mathbf{X}, t)$  are constructed by discretizing  $t$  and incrementally solving Eq. (5.17) by updating the displacement boundary conditions. Consequently, nonlinear propagation effects such as harmonic generation or shock formation are absent in the limit of  $\gamma \ll 1$ .

### 5.2.3 Elastic Wave Propagation (Small Wave)

Once the displacements  $\mathbf{u}_d$  are found, the tensor  $\mathbf{L}$  is constructed for each material point and time increment using Eq. (5.12). Each element of  $\mathbf{L}$  can then be written as a Fourier series in time,

$$L_{ijkl}(\mathbf{X}, t) = \sum_{n=-\infty}^{\infty} \hat{L}_{ijkl}^n(\mathbf{X}) e^{-in\omega_m t}, \quad (5.18)$$

where the Fourier components,  $\hat{L}_{ijkl}^n(\mathbf{X})$ , are determined from the set of solutions to Eq. (5.17) for all time increments of the modulation, using

$$\hat{L}_{ijkl}^n(\mathbf{X}) = \frac{\omega_m}{2\pi} \int_{-\pi/\omega_m}^{\pi/\omega_m} L_{ijkl}(\mathbf{X}, t) e^{in\omega_m t} dt. \quad (5.19)$$

The Bloch wave procedure from Chapter 3 is utilized to find the periodic traveling wave solutions of Eq. (5.14) using the ansatz

$$u_i = e^{i(\mathbf{K} \cdot \mathbf{X} - \omega t)} \sum_{p=-\infty}^{\infty} \hat{u}_i^p(\mathbf{X}) e^{-ip\omega_m t}, \quad (5.20)$$

where  $\mathbf{K} = [k_x, k_y]^T$  is the Bloch wavenumber, and the Bloch wave mode is written as a Fourier series in time. Physically speaking, the fundamental mode and frequency  $(\hat{\mathbf{u}}^0, \omega)$  is interpreted as an incident mode propagating in the medium, and the harmonics with mode and frequency  $(\hat{\mathbf{u}}^p, \omega + p\omega_m)$  are modes scattered by the modulation in the forward ( $p > 0$ ) and backward ( $p < 0$ ) direction [32].

The series in Eqns. (5.18) and (5.20) are truncated to  $2P + 1$  terms, and substituted into Eq. (5.14). The orthogonality of the Fourier series is then utilized to eliminate one of the summations, yielding a system of differential equations for the harmonic amplitudes  $\hat{\mathbf{u}}^p$ , which is written in index notation as

$$\begin{aligned} \sum_{n=-P}^P \left[ \left( \hat{L}_{ijkl}^{p-n} \hat{u}_{k,l}^n + i \hat{L}_{ijkl}^{p-n} K_l \hat{u}_k^n \right)_{,j} \right. \\ \left. + i \hat{L}_{ijkl}^{p-n} \hat{u}_{k,l}^n K_j - \hat{L}_{ijkl}^{p-n} \hat{u}_k^n K_l K_j \right] \\ = -\rho_0 (\omega + p\omega_m)^2 \hat{u}_i^p, \quad p \in [-P, P]. \quad (5.21) \end{aligned}$$

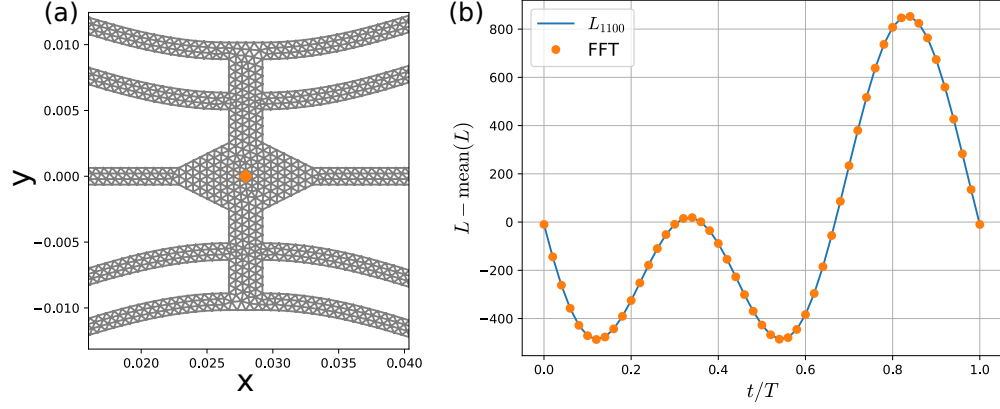


Figure 5.3: (a) Computational mesh. (b) The resulting time dependence and FFT solution of the  $L_{1100}$  component from a prescribed pre-strain at the node marked in (a). Note that the time solution contains more than one Fourier component.

This set of equations is then solved subject to homogeneous Dirichlet boundary conditions on the faces where the external pre-strain was applied,

$$\hat{\mathbf{u}}^p(X \in \Gamma_u) = 0, \quad (5.22)$$

periodic boundary conditions on the left and right edges as indicated in Fig. 5.2(a),

$$\hat{\mathbf{u}}^p(X \in \Gamma_+) = \hat{\mathbf{u}}^p(X \in \Gamma_-), \quad (5.23)$$

and stress-free boundary conditions on the remaining faces.

### 5.3 Numerical Implementation

The finite element method is used to solve both the nonlinear deformation and elastic wave equations derived in Sec. 5.2 by implementing the finite



element method using the open source software FEniCS [99]. The modulation deformation problem for each time step is solved using the nonlinear finite element model derived in 4.2.1. The following steps are demonstrated with an example shown in Fig. 5.3. Once  $\mathbf{u}_d$  is computed, the tangent modulus tensor  $\mathbf{L}$  is created using an automatic differentiation algorithm available in FEniCS. The Fourier components  $\hat{L}_{ijkl}$  are then found by taking the time solution of  $L_{ijkl}$  at each node in the mesh (diamond marker in Fig. 5.3(a)), performing a numerical Fast Fourier Transform (FFT) in time (Fig. 5.3(b)), and reconstructing the harmonic results of the FFT into a set of tensors  $\{\hat{\mathbf{L}}^{-P}, \hat{\mathbf{L}}^{-P+1}, \dots, \hat{\mathbf{L}}^P\}$ .

In order to implement Eq. (5.21) in a finite element algorithm, the appropriate weak forms must be derived. This is accomplished in the same manner as described in Chapter 3 for the general case of a 1D medium with space- and time-dependent modulus. First, one takes the Hermitian inner product over the supercell domain  $\Omega$  of the left- and right- hand sides of Eq. (5.21) with the respective harmonic test vector  $\hat{\mathbf{v}}^p$ . Application of Green's identity on the divergence term and summing the equations yields the integral equation

$$\sum_{p,n=-P}^P \left[ - \int_{\Omega} \hat{L}_{ijkl}^{p-n} (\hat{u}_{k,l}^n \hat{v}_{i,j}^p + K_l K_j \hat{u}_k^n \hat{v}_i^p) d\Omega \right. \\ \left. - i \int_{\Omega} \hat{L}_{ijkl}^{p-n} (\hat{u}_k^n K_l \hat{v}_{i,j}^p - \hat{u}_{k,l}^n K_j \hat{v}_i^p) d\Omega \right. \\ \left. + \rho_0 (\omega + p\omega_m)^2 \int_{\Omega} \hat{u}_i^p \hat{v}_i^p d\Omega \right] = 0, \quad (5.24)$$

which is discretized following standard finite element procedures [40] to yield a quadratic eigenvalue problem

$$\omega^2 \mathbf{M} \mathbf{U} + \omega \mathbf{C} \mathbf{U} + \mathbf{K}(\mathbf{K}) \mathbf{U} = 0, \quad (5.25)$$

where  $\mathbf{U} = [\mathbf{u}^{-P}, \mathbf{u}^{-P+1}, \dots, \mathbf{u}^P]^\text{T}$ . The frequency-wavenumber spectrum is generated by assigning a value of  $\mathbf{K}$  and solving the quadratic eigenvalue problem provided by Eq. (5.25) for the frequency and harmonic amplitudes. In this work, the Bloch wavenumber  $\mathbf{K} = [k_x, 0]^\text{T}$  is restricted to be a vector pointing in the  $x$  direction and are thus concerned with a quasi-one-dimensional problem. Due to the periodicity of the supercell,  $k_x$  is restricted to the first Brillouin zone of the supercell  $k_x \in [-\pi/(6L_x), \pi/(6L_x)]$ . Positive values of  $k_x$  refer to waves that propagate in the positive  $x$  direction (in the direction of pre-strain modulation), and negative values of  $k_x$  refer to waves that propagate in the negative  $x$  direction (in the opposite direction of the pre-strain modulation).

The matrices resulting from the finite element discretization are large and sparse. Specifically, the total matrix size is  $\text{DOF}_{\text{SC}}(2P+1) \times \text{DOF}_{\text{SC}}(2P+1)$ , where  $\text{DOF}_{\text{SC}}$  is the number of degrees of freedom of the supercell with boundary conditions applied. For example, a typical supercell mesh in this work contained on the order of  $\text{DOF}_{\text{SC}} = 100,000$ . Therefore, it is not practical to solve for all eigenfrequencies and eigenvectors. The computational challenges associated with this problem are addressed by using the software library SLEPc [102] (the Scalable Library for Eigenvalue Problem Computations) to

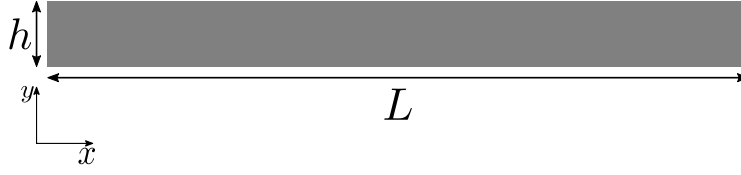


Figure 5.4: Geometry of the thin plate Kirchhoff benchmark system.

solve Eq. (5.25), which takes advantage of distributed-memory parallelization and can be executed on a computer cluster. Further, a two-level orthogonal Arnoldi (TOAR) algorithm is used in combination with a shift-and-invert transformation to extract eigenfrequencies near a target magnitude value.

## 5.4 Results

The finite element approach described in Sec. 5.3 can be used to compute the frequency-wavenumber spectrum for any geometry of interest, which is the primary contribution of the present work. Before solving the negative stiffness chain problem, the accuracy of the finite element model is first assessed by comparing the frequency-wavenumber spectrum calculated with this technique to flexural wave propagation in a thin Kirchhoff plate with a spatiotemporally-modulated Young's modulus [31], which is different than the longitudinal wave problems investigated in Chapter 3. Note that while the flexural wave mode is compared, the finite element model captures both the flexural and longitudinal waves in a thin Kirchhoff plate. The use of the finite element model is then demonstrated by investigating transverse and longitudinal wave propagation in the negative stiffness chain with a spatiotemporally-

modulated external pre-strain.

#### 5.4.1 Numerical Benchmark

To verify the implementation of the finite element model presented in Sec. 5.3, elastic wave dispersion is investigated in a thin Kirchhoff plate with a spatiotemporally-modulated Young's modulus and compared with the model presented in Trainiti et al. [31] The geometry is shown in Fig. 5.4, where  $h/L = 0.01$ . The plate is assigned the material properties of static Young's modulus  $E_0 = 1$  GPa, density  $\rho_0 = 7700$  kg/m<sup>3</sup>, and Poisson's ratio  $\nu = 0.1$ . These values are chosen such that Kirchhoff plate theory remains valid for all wavenumbers of interest. The Young's modulus is modulated with the form

$$E(x, t) = E_0 + E_m \cos(\omega_m t - k_m x). \quad (5.26)$$

For this case, the tangent modulus tensor in Eq. (5.12) simplifies to the stiffness tensor since no geometric nonlinearity is present and the material is assumed isotropic *a priori*

$$L_{ijkl} = \lambda \delta_{ij} \delta_{kl} + \mu (\delta_{ik} \delta_{jl} + \delta_{il} \delta_{jk}), \quad (5.27)$$

where  $\delta_{ij}$  is the Kronecker delta function, and  $\lambda, \mu$  are the first and second Lamé parameters of the plate material, respectively. Recall that the Lamé parameters are related to the Young's modulus and Poisson's ratio through the relations

$$\lambda = \frac{E\nu}{(1+\nu)(1-2\nu)}, \quad \mu = \frac{E}{2(1+\nu)}. \quad (5.28)$$

The modulation parameters are chosen to be  $E_m = 0.4E_0$  and  $\omega_m/k_m = c_m = 0.002$ . The transverse mode branch with  $P = 1$  is shown in Fig. 5.5(a), where

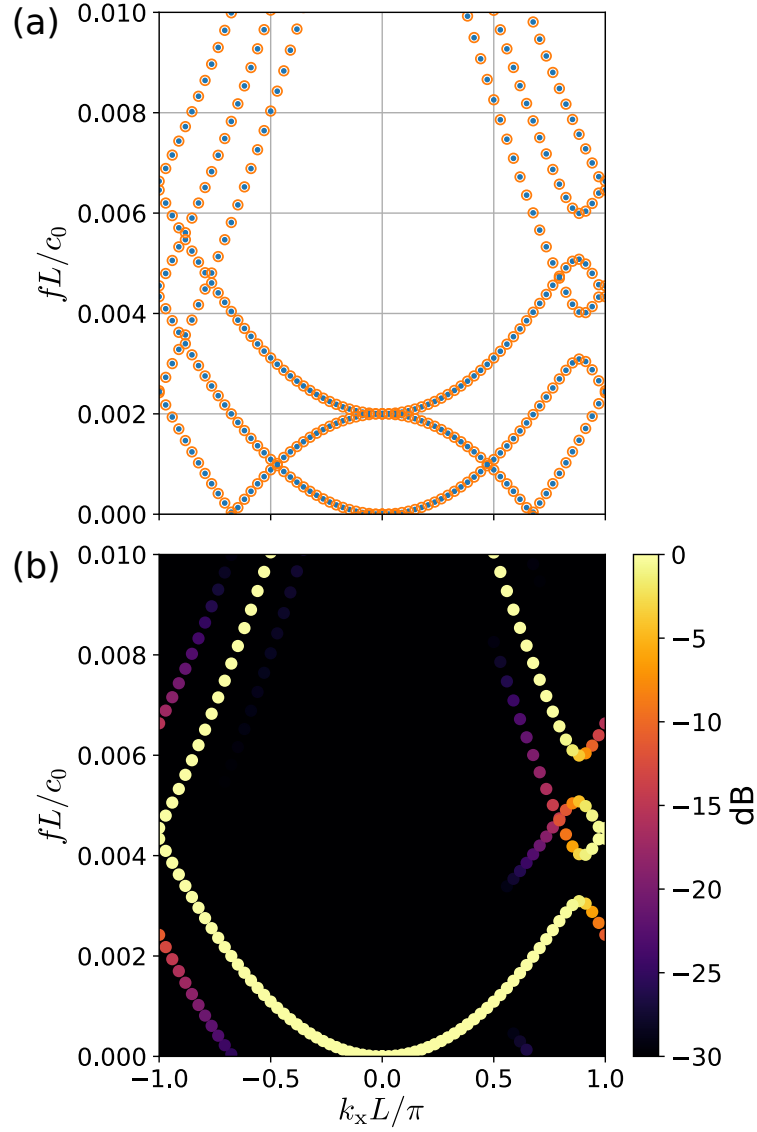


Figure 5.5: (a) Frequency-wavenumber spectrum of the transverse wave in a thin Kirchhoff plate. Open circles are the results from Trainiti et al., and filled circles are results obtained from the finite element model. (b) The finite element results presented in (a) but with each point colored by its normalized magnitude of the fundamental component in decibels,  $20 \log_{10}(\|\hat{\mathbf{u}}^0\|/\|\mathbf{U}\|)$ .

$c_0 = \sqrt{E_0/\rho}$  is the longitudinal wave speed of the plate. As seen in Fig. 5.5(a), the finite element model shows excellent agreement with the model presented in Trainiti et al. [31] and thus the numerical approach has been appropriately benchmarked.

This system is non-reciprocal since the frequency- wavenumber spectrum is not symmetric about  $k_x = 0$ . However, band gaps do not occur in the same way as a stationary periodic medium, where  $k_x$  becomes purely imaginary in certain frequency regions. Rather, due to the existence of harmonics in a spatiotemporal medium, all frequencies are associated with least one real-valued  $k_x$  that represents a propagating mode. However, the amplitudes of the harmonic modes ( $p \neq 0$  in Eq. (5.20)) may be significantly less in magnitude than the fundamental mode ( $p = 0$  term). The amplitude differences are indicated in Fig. 5.5(b), where the finite element results in Fig. 5.5(a) are plotted and assigned a color that is determined by the magnitude of the fundamental component of the Bloch wave solution in decibels, specifically  $20 \log_{10}(\|\hat{\mathbf{u}}^0\|/\|\mathbf{U}\|)$ . In the example case considered here, the fundamental mode couples to the harmonic modes in the frequency range  $fL/c_0 \in [0.003, 0.006]$ . However, this coupling is direction-dependent, creating directional band gaps. The amplitudes of the harmonic modes within the fundamental mode band gaps are significantly lower in magnitude than the amplitude of the fundamental mode propagating in the  $-x$  direction.

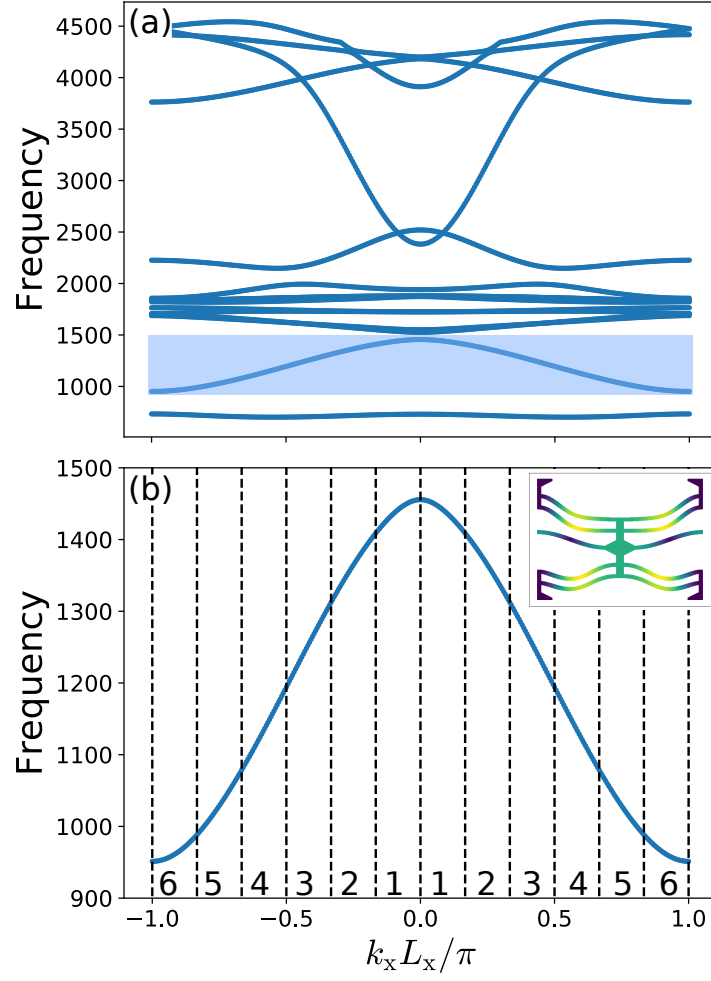


Figure 5.6: (a) Frequency-wavenumber spectrum of the negative stiffness chain with a static pre-strain of  $\beta_0 = 0.01$ . The transverse mode is highlighted. (b) The transverse mode spectrum with the vertical lines and numerals indicating the supercell Brillouin zone number. The mode shape is shown in the inset image.

Table 5.1: Geometric parameter values depicted in Fig. 5.1. All numerical values have units of mm.

Parameter	Description	Value
$L_x$	Horizontal length	55.88
$L_y$	Vertical length	40.64
$t_b$	Beam thickness	1.27
$t_s$	Beam separation	3.81
$h_b$	Beam apex height	5.08
$h_c$	Center height	1.90
$w_c$	Center width	3.8
$h_{cb}$	Center beam height	2.54
$w_{cb}$	Center beam width	2.54
$t_{hb}$	Horizontal beam thickness	1.27

#### 5.4.2 Negative Stiffness Chain

The negative stiffness chain depicted in Fig. 5.2(a) is now investigated in order to demonstrate the generality of the finite element method and to investigate mechanical modulation as a means to generate non-reciprocal wave phenomena. The values assigned to the geometric parameters shown in Fig. 5.1 are provided in Table 5.1, which is identical to Table 4.1 except the beam separation parameter  $t_s$  is chosen to be 3.81 mm, rather than 1.27 mm which was the case for the NSH studied in Chapter 4. The negative stiffness chain is assumed to be fabricated from laser sintered Nylon 11 with material properties  $\rho_0 = 1040 \text{ kg/m}^3$ , Poisson's ratio of 0.33, and Young's modulus of 1582 MPa. The frequency-wavenumber spectrum of the negative stiffness element depicted in Fig. 5.1 is first studied using the finite element approach in Chapter 4 with a static pre-strain of  $\beta_0 = 0.01$ . The dispersion curves for the unit cell



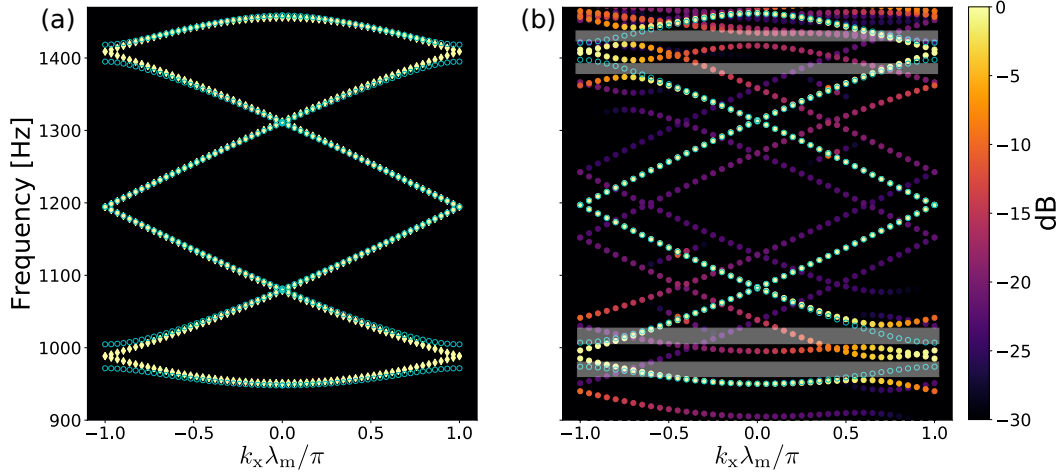


Figure 5.7: Frequency-wavenumber spectra of the transverse mode of the negative stiffness chain. (a) Comparison of spatial modulation (open circles) and static pre-strain only (diamonds; same data as in Fig. 5(b), but folded at the Brillouin zone boundaries). (b) Comparison of spatial modulation (open circles; same as in (a)) and spatiotemporal modulation (filled circles), where the color scale is defined in the same way as Fig. 5.5(b).

Brillouin zone is shown in Fig. 5.6(a). Note that the presence of displacement boundary conditions on the top and bottom faces of the negative stiffness chain eliminates “plane wave” modes that propagate down to zero frequency. The transverse mode, which is highlighted in Fig. 5.6(a) and repeated with an enlarged view in Fig. 5.6(b), is first investigated in the present work. The vertical dashed lines and numbers in Fig. 5.6(b) represent the Brillouin zones of the supercell shown in Fig. 5.2(a), which will aid in the interpretation of the band-folded supercell results detailed below.

Next, the frequency-wavenumber spectrum is obtained for modulation of the external pre-strain in space only by setting  $\omega_m = 0$  and  $\Delta\beta =$

$0.3\beta_0$  in Eq. (5.15). The results of this case are shown in Fig. 5.7(a). The frequency-wavenumber spectrum of the transverse mode in a spatially-modulated negative stiffness chain is nearly identical to the folded frequency-wavenumber spectrum of the static pre-strain case shown in Fig. 5.6(b), with band gaps forming near 990 Hz and 1410 Hz at the edge of the supercell Brillouin zone due to Bragg scattering from the spatial periodicity. Finally, the frequency-wavenumber spectrum of the transverse mode in the spatiotemporally-modulated pre-strain case with eight of the generated harmonics present ( $P = 4$ ) is shown in Fig. 5.7(b) with  $c_m = 0.02c_s$ . The transverse mode fundamental branch is similar to the results from the spatially-modulated negative stiffness chain except at frequencies near the band gaps. Here, directional band gaps are now present in the spatiotemporally-modulated negative stiffness chain and are highlighted with shaded boxes in Fig. 5.7(b).

The approximate dispersion relation derived in Sec. 3.4.2, Eq. (3.97), is used to obtain the lowest directional bandgap in Fig. 5.7(b), which is shown in Fig. 5.8. This is computed by considering the coupling of the mode that exists on the dispersion branch that passes through the bandgap (red dashed line in Fig. 5.8) and the mode on the next branch in ascending frequency (orange dashed line in Fig. 5.8). A large amount of coupling between these two mode exist at the wavenumber where the two branches are separated by  $f_m = \omega_m/(2\pi)$ . The approximate dispersion curve agrees well with the frequency-wavenumber results from Fig. 5.7(b) at the bandgap and in the  $+k$  region, and is less accurate in the  $-k$  region. This is most likely attributed to

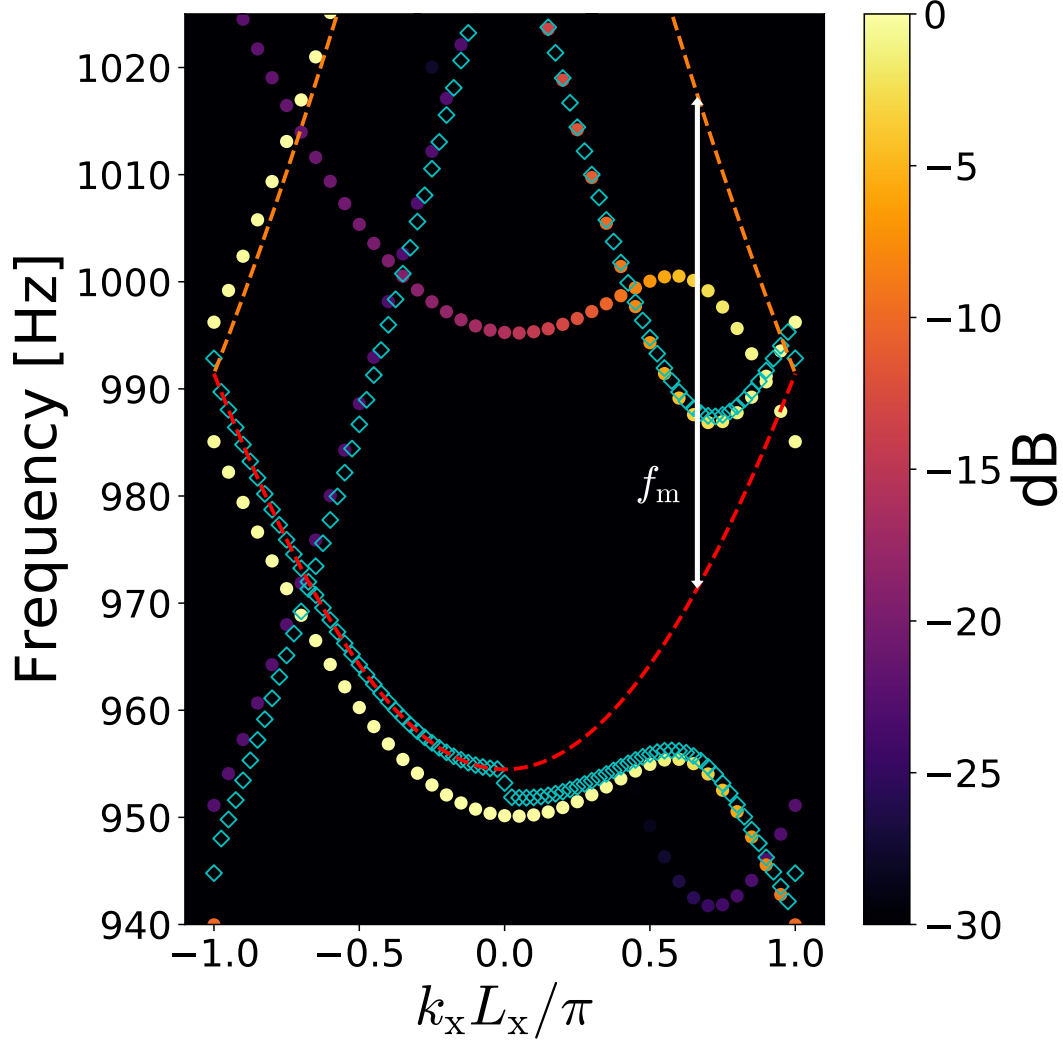


Figure 5.8: Comparison of the approximate dispersion relation, Eq. (3.97), (open diamonds) with the frequency-wavenumber spectrum of the transverse mode from Fig. 5.7. The red dashed line represents the reference eigenvalue branch, which is the solution to Eq. (3.89), and the orange dashed line represents the coupling branch. The two modes exhibit strong coupling at the wavenumber where the two curves are separated by  $f_m$ .

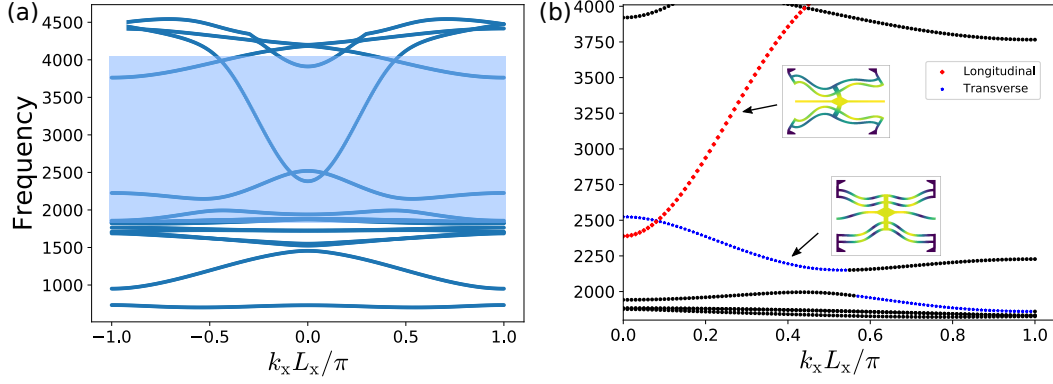


Figure 5.9: (a) Dispersion of the negative stiffness chain with a static pre-strain of  $\beta_0 = 0.01$ . A region that contains the longitudinal and a higher-order transverse mode is highlighted. (b) Zoom-in plot of the shaded region in (a), where the longitudinal and transverse modes are identified using the modal filter technique discussed in Sec. 4.3.1. The respective mode shapes are shown in the inset image.

the approximation of the mode eigenvector.

Another frequency region of interest is highlighted in Fig. 5.9(a), which shows the unit cell response of the negative stiffness chain with a static pre-strain of  $\beta_0 = 0.01$ . A longitudinal and higher-order transverse mode exists in this range, and is shown in Fig. 5.9(b) using the modal filter technique discussed in Sec. 4.3.1. Note that this is the lowest-order longitudinal mode due to the displacement boundary conditions. This region is investigated using identical modulation parameters of the previous case ( $\Delta\beta = 0.3\beta_0$  and  $c_m = 0.02c_s$ ). The resulting frequency-wavenumber spectrum is shown in Fig. 5.10, along with the dispersion curves that result from the spatial modulation of the pre-strain. Three frequency ranges of interest are highlighted

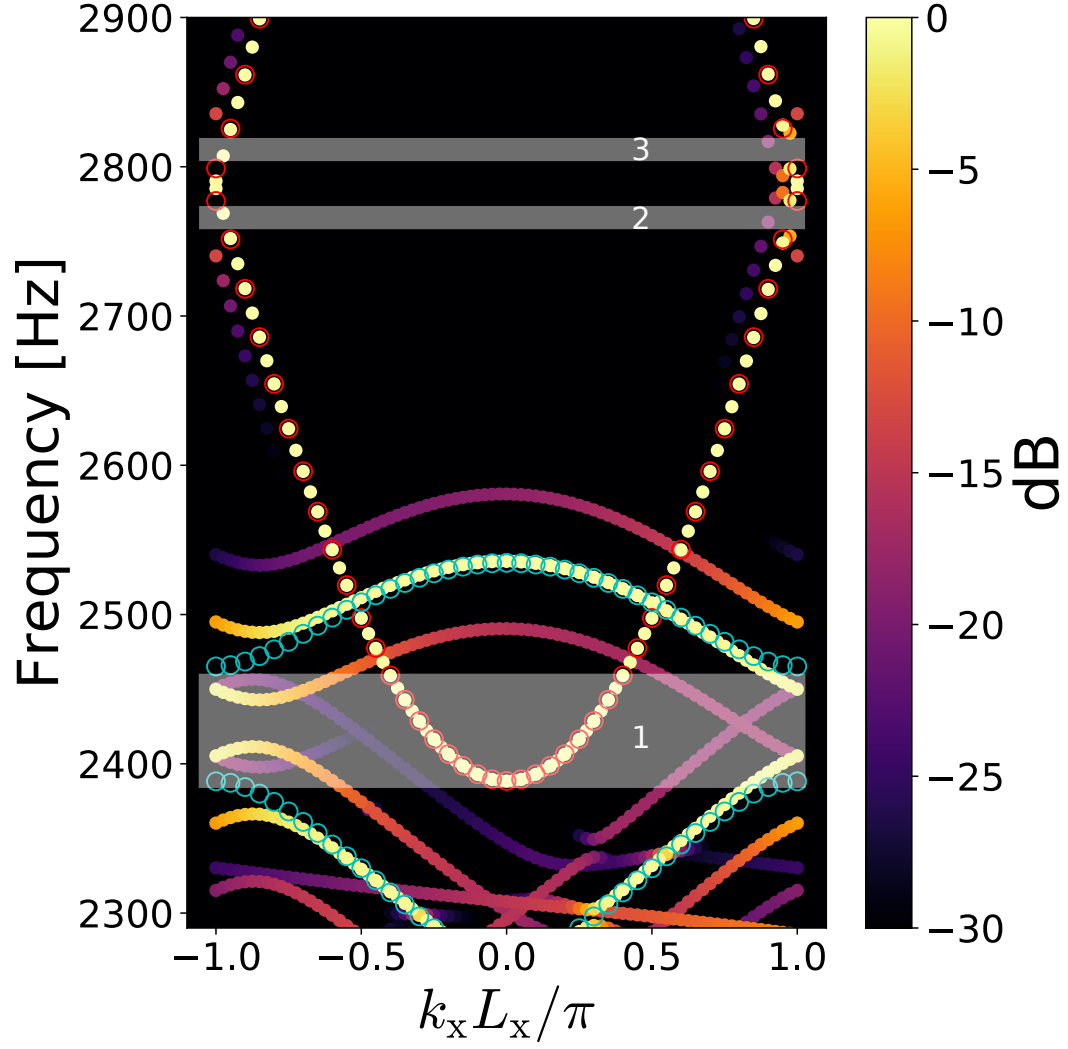


Figure 5.10: Frequency-wavenumber spectrum of the region highlighted in Fig. 5.9(a). The dispersion curves of the transverse mode (blue open circles) and the longitudinal mode (red open circles) for a spatial modulation of the pre-strain are also plotted.

in Fig. 5.10. Region 1 shows that the transverse mode displays a large degree of non-reciprocity, while the longitudinal mode is mostly identical to the case of space-only modulation of the pre-strain and therefore exhibits only a small degree of non-reciprocity. These results are in agreement with the conclusions made in Chapter 4, where the transverse mode is very sensitive to variations of the pre-strain while the longitudinal mode is considerably less sensitive. This property gives the flexibility to tune the degree of non-reciprocity, including directional bandgap locations, of the transverse mode without affecting the longitudinal mode. The longitudinal mode exhibits non-reciprocity in a narrow frequency band highlighted in regions 2 and 3 of Fig. 5.10, where directional bandgaps form. The effect of increasing the modulation speed to  $c_m = 0.04c_s$  while maintaining the modulation depth is shown in Fig. 5.11. In region 1, the increase in the modulation speed further shears the frequency-wavenumber spectrum of the transverse mode, while the frequency-wavenumber spectrum of the longitudinal mode remains the same. The change in the modulation speed however can be used to tune the frequency ranges of the longitudinal mode directional bandgaps in regions 2 and 3. Specifically, increasing the modulation speed results in region 2 shifting down in frequency and region 3 shifting up in frequency. The width of the bandgap, however, does not change significantly.

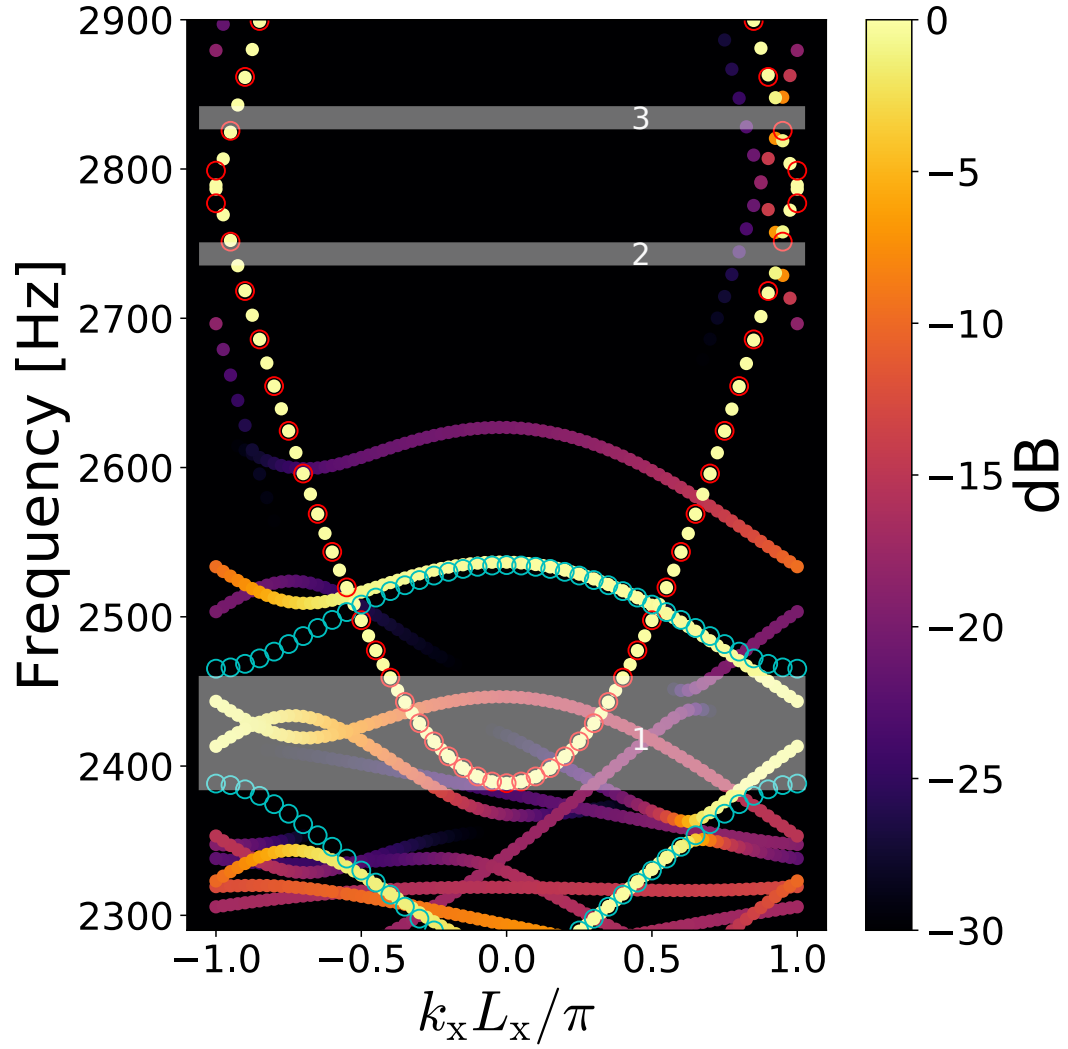


Figure 5.11: Frequency-wavenumber spectrum of the region highlighted in Fig. 5.9(a) for a modulation speed of  $c_m = 0.04c_s$ . The highlighted regions and spatial-only modulation results are identical to Fig. 5.10.

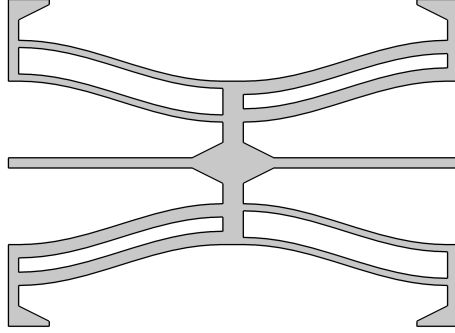


Figure 5.12: Chiral configuration of the negative stiffness element with a beam thickness change of 10% (geometry is exaggerated for visualization purposes).

#### 5.4.3 Geometric Asymmetry

One of the primary advantages of the finite element framework developed here is that changes in the geometry can be accounted for without significant difficulty. The ability to modify the unit cell geometry results in a large design space to tailor the degree of non-reciprocity, including directional bandgaps, for each mode of interest. As an illustrative example, consider the modified negative stiffness element shown in Fig. 5.12, where the thickness of the pre-curved beams in the top-left and bottom-right quadrants are decreased by 10% (a higher value is used in Fig. 5.12 for ease of visualization), and the thickness of the pre-curved beams in the top-right and bottom-left quadrants are increased by 10%. This unit cell displays chirality, i.e. mirror symmetry about the horizontal and vertical axes is broken while retaining  $180^\circ$  rotational symmetry. The dispersion curves for the transverse and longitudinal modes in a chain composed of the chiral negative stiffness element in Fig. 5.12 for a



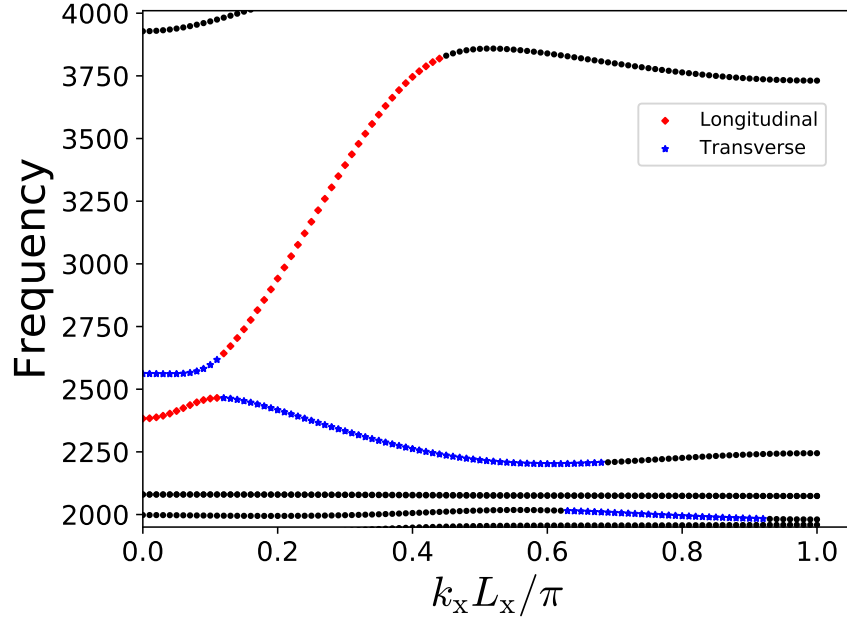


Figure 5.13: Transverse and longitudinal modes of the chiral negative stiffness chain with a static pre-strain of  $\beta = 0.01$ .

static pre-strain of  $\beta_0 = 0.01$  are shown in Fig. 5.13. Compared to Fig. 5.9, the chiral asymmetry causes the transverse and longitudinal modes to couple, resulting in a bandgap around 2500 Hz. This coupling is due to the introduction of a rotational motion of the center of the unit cell brought on by the differences of the force responses of the two different sets of pre-curved beams, which is present in both modes. The frequency-wavenumber spectrum of the chiral negative stiffness chain with space-only and spatiotemporal modulation of the pre-strain with modulation parameters  $\Delta\beta = 0.3\beta_0$ ,  $c_m = 0.04c_s$  is shown in Fig. 5.14(a). The longitudinal mode bandgaps in regions 2 and 3 from Fig. 5.11 remain mostly unaltered. However, the longitudinal mode now shows a greater sensitivity to the pre-strain modulation in the region shown in

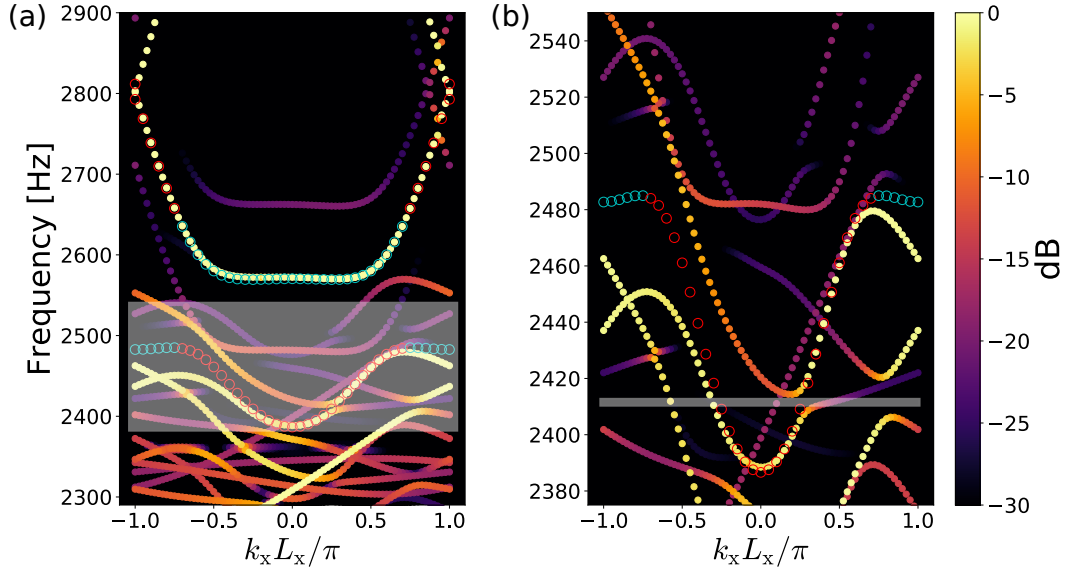


Figure 5.14: (a) Frequency-wavenumber spectrum of the chiral negative stiffness chain for a modulation speed of  $c_m = 0.04c_s$ . The dispersion curves of the transverse mode (blue open circles) and longitudinal mode (red open circles) for the space-only modulation of the pre-strain are also shown. (b) Zoom-in of the highlighted region in (a). The longitudinal mode directional bandgap is highlighted.

Fig. 5.14(b) compared to the symmetric geometry case in Fig. 5.11. Specifically, an additional directional bandgap in the longitudinal mode now appears, which is highlighted in Fig. 5.14(b). Though the uni-directional bandgap is very narrow for this specific geometry, this simple example illustrates that chiral asymmetry can be used as a means to increase the degree of non-reciprocity of the longitudinal mode.

## 5.5 Conclusion

In this chapter, the finite element approach developed in Chapter 4, along with the numerical approach discussed in Chapter 3, was generalized to study non-reciprocal elastic wave propagation in a pre-strained elastic metamaterial. A quasi-one dimensional chain that resembles the negative stiffness honeycomb studied in Chapter 4 was investigated as an example metamaterial that displays a large degree of non-reciprocity for small external pre-strain modulations in time and space. The utility of this finite element approach was further demonstrated by investigating a modified version of the negative stiffness chain with unit cell chirality. In general, this model can be used to study any sub-wavelength geometries or modulations that are difficult or impossible to model with analytic techniques. Therefore, this approach can be used to design and optimize realistic devices that benefit from a large degree of non-reciprocity, such as acoustic communication devices with increased data throughput and improved vibration isolation devices.

# Chapter 6

## Conclusion

### 6.1 Summary and Contributions

Acoustic and elastic wave metamaterials have received significant attention as a means to directly control the propagation of waves through a synthetic elastic material. However, current metamaterial designs suffer from a few drawbacks that limit their usefulness. Specifically, passive metamaterials that rely on subwavelength resonances show high performance behavior only at narrow bands of frequency and are limited by the presence of absorption. Furthermore, their dynamic properties cannot be altered after construction. It is therefore highly desirable to study metamaterials that show extraordinary effective behavior in a wide frequency band without relying on resonances that can also be tuned to exhibit high performance at a desired frequency range. Tunable elastic metamaterials that exhibit large changes in the effective stiffness via geometric nonlinearity from an applied external pre-strain shows promise in overcoming these limitations, and is therefore the main study of this work.

Recently, research on using metamaterials as a non-reciprocal medium has enabled even greater control over the propagation direction of waves, in-

cluding the ability to generate conditions for one-way wave propagation. This work focused on modulating the material properties of a metamaterial in space and time using mechanical deformation to induce non-reciprocity, which has been unexplored. This dissertation therefore also studied the adaptation of tunable elastic materials for the creation of nonreciprocal elastic metamaterials.

In order to unify the present studies of tunable and non-reciprocal metamaterials, a negative stiffness honeycomb (NSH) was used as a representative metamaterial. Negative stiffness honeycombs exhibit non-monotonic force-displacement response when subjected to an externally-applied pre-strain. Previous studies have made use of NSH for vibration isolation and impact absorption. However, the strong geometric nonlinearity present in NSH suggest that linear elastic wave propagation in this structure exhibit a strong dependence on the externally-imposed pre-strain. The effect of a static pre-strain on the dispersive wave behavior in NSH was therefore studied in this work, as well as the non-reciprocal effects that arise when modulating the pre-strain imposed on the NSH as a function of space and time.

In Chapter 1, two research questions were posed as the motivation of this work. Each of these questions are now addressed along with the contributions of this dissertation.

# **1. How are the bandgaps and anisotropic properties of the transverse and longitudinal waves in a metamaterial with**

**strong geometric nonlinearity affected by an externally-applied static pre-strain?**

To begin answering this question, a modeling approach must be derived that includes geometric nonlinearity and the effect of the resulting deformation on the superimposed propagating elastic waves. The complex geometry present in unit cells that exhibit large geometric nonlinearity severely limits any analytical study, which necessarily motivates the development of a computational technique. The finite element method (FEM) is the numerical method of choice due to its numerical accuracy in solving the equations of motion as well as its ability to handle complex geometries.

In this dissertation, the small-on-large approximation was introduced and derived in Chapter 4, which decomposes the solution for the total displacement in an elastic metamaterial structure into a nonlinear finite element model which captures the large deformation from an external pre-strain, and an elastic wave finite element model linearized about the deformation. The Bloch wave formalism introduced in Chapter 3 was then utilized on the resulting linear elastic wave equations to formulate an eigenvalue problem to calculate the dispersion curves and mode shapes, as well as the group velocity to study the anisotropic wave propagation behavior. The contributions from this particular work with respect to the numerical modeling include a systematic procedure to model both the nonlinear deformation and elastic Bloch wave problems in an open-source computational environment. Further, a mode filtering technique was implemented that uses modal information in the long-wavelength

regime to identify modes of interest on the dispersion curves at higher Bloch wavelengths. This was shown to be particularly useful in identifying modal bandgaps as well as the correct slowness curves for determining the anisotropic propagation behavior of each mode.

These numerical tools were then used to answer question 1 for NSH. In particular it was found that there exists a frequency region where there is only longitudinal wave propagation, which can be tuned by applying an external pre-strain. In general, the dispersion and slowness curves for the transverse mode displayed significant tunability given a small amount of pre-strain. In addition, the transverse mode was observed to be highly directional, and the direction of propagation can be tuned by changing the pre-strain amount. Conversely, the longitudinal mode propagates in all directions and is significantly less sensitive to the pre-strain than the transverse modes. This work therefore contributes to current metamaterials research by demonstrating that NSH is a versatile metamaterial that can be used in numerous applications, such as transformation acoustics or as an elastic gradient index lens.

## **2. What non-reciprocal effects are observed when the external pre-strain imposed on a metamaterial with strong geometric nonlinearity is modulated in space and time?**

Currently, there is a significant need for numerical tools to study non-reciprocal wave dispersion behavior in a spatiotemporally-modulated elastic media. In Chapter 3, the wave phenomena present when the modulus of a

medium is varied in space and time individually, and simultaneously in space and time was discussed. The mathematical and computational techniques used to solve each of these pre-strain modulation cases, which includes the finite element method, were derived in a geometrically simple one-dimensional setting which was then generalized to the general elastodynamic case in multiple dimensions in Chapter 5. The small-on-large approximation introduced in Chapter 4 was revisited to include the effects of a spatiotemporally-varying pre-strain. A quadratic eigenvalue problem was then derived to generate the frequency-wavenumber spectrum. This computational approach is one of the main contributions of this dissertation, which now enables researchers to further study and design non-reciprocal metamaterials for practical applications when considering arbitrarily complex unit cell and super cell geometries.

The spatiotemporal finite element approach was used to answer question 2 for a negative stiffness chain, which is a quasi-one-dimensional version of NSH. In particular, the transverse modes exhibit a high degree of non-reciprocity for a small amount of pre-strain modulation, including the formation of several directional bandgaps. Conversely, the longitudinal mode displayed a small degree of non-reciprocity except for two narrow frequency bands of directional bandgaps. The utility of the finite element approach was further demonstrated by investigating a modification of the negative stiffness chain with chiral geometric asymmetry. It was shown that the longitudinal mode is more sensitive to the pre-strain modulation for the case of a chiral unit cell, and exhibits an additional directional bandgap that is lower in



frequency than the two that existed in the symmetric unit cell case. This investigation contributes to current work in non-reciprocal wave propagation by demonstrating a mechanical metamaterial that displays a high degree of non-reciprocity given a small amount of externally-modulated pre-strain, and that geometric asymmetry can be used to couple longitudinal and transverse wave motion and thereby increase the degree of non-reciprocity of the longitudinal and transverse modes.

## 6.2 Future Work

The computational approaches developed in this dissertation provide a means to study elastic wave propagation in a general pre-strained medium. While these methods were successfully implemented and used to study wave propagation in NSH, further work is necessary in exploring the further utility of these computational methods and NSH. Below are a few suggestions for further research:

- 1. Unit Cell Design:** The finite element approach derived in this work opens a large design space to create optimal or tailored non-reciprocal elastic wave devices. Specifically, the constituent material properties and the geometric parameters of the unit cell can all be varied to yield designs that exhibit directional bandgaps at target frequency ranges of interest. Therefore, this finite element approach, in addition to the approximate dispersion relation derived in Chapter 3, can be used with design algorithms to investigate the design space for specific applications of interest.

**2. Experimental Validation:** While the finite element approaches derived in this work all numerically solve the equations of motion to a high degree of accuracy, ultimately all of the results in this dissertation on the strain-modulated negative stiffness honeycomb must be experimentally verified. In particular, the effects of a finite lattice on measuring the frequency-wavenumber spectrum needs to be investigated. Ultimately, the design of a successful experiment presents its own challenges and opportunities and will require a significant effort for completion.

**3. Negative Stiffness Honeycomb Metamaterial:** The results presented in this dissertation show that the negative stiffness honeycomb geometry exhibits many useful dynamic properties in addition to its ability to absorb impacts. Specific examples include the meta-fluid region reported here and the ability to independently control the propagation of transverse and longitudinal modes. Applications where this metamaterial can be integrated to meet the challenges of transformation elastodynamics, such as acoustic cloaking and meta-lens, are therefore of significant interest.

## Bibliography

- [1] Z. Liu, X. Zhang, Y. Mao, Y. Zhu, Z. Yang, C. T. Chan, and P. Sheng, “Locally resonant sonic materials,” *Science*, vol. 289, no. 5485, pp. 1734–1736, 2000.
- [2] N. Fang, D. Xi, J. Xu, M. Ambati, W. Srituravanich, C. Sun, and X. Zhang, “Ultrasonic metamaterials with negative modulus,” *Nat. Mater.*, vol. 5, no. 6, pp. 452–456, 2006.
- [3] J. Li and C. T. Chan, “Double-negative acoustic metamaterial,” *Phys. Rev. E*, vol. 70, no. 5, p. 055602, 2004.
- [4] J. B. Pendry, “Negative refraction makes a perfect lens,” *Phys. Rev. Lett.*, vol. 85, no. 18, p. 3966, 2000.
- [5] C. M. Park, J. J. Park, S. H. Lee, Y. M. Seo, C. K. Kim, and S. H. Lee, “Amplification of acoustic evanescent waves using metamaterial slabs,” *Phys. Rev. Lett.*, vol. 107, no. 19, p. 194301, 2011.
- [6] V. M. García-Chocano, J. Christensen, and J. Sánchez-Dehesa, “Negative refraction and energy funneling by hyperbolic materials: An experimental demonstration in acoustics,” *Phys. Rev. Lett.*, vol. 112, no. 14, p. 144301, 2014.

- [7] M. Ambati, N. Fang, C. Sun, and X. Zhang, “Surface resonant states and superlensing in acoustic metamaterials,” *Phys. Rev. B*, vol. 75, no. 19, p. 195447, 2007.
- [8] K. Deng, Y. Ding, Z. He, H. Zhao, J. Shi, and Z. Liu, “Theoretical study of subwavelength imaging by acoustic metamaterial slabs,” *J. Appl. Phys.*, vol. 105, no. 12, p. 124909, 2009.
- [9] J. J. Park, C. M. Park, K. Lee, and S. H. Lee, “Acoustic superlens using membrane-based metamaterials,” *Appl. Phys. Lett.*, vol. 106, no. 5, p. 051901, 2015.
- [10] A. N. Norris, “Acoustic cloaking theory,” *Proc. R. Soc. A*, vol. 464, no. 2097, pp. 2411–2434, 2008.
- [11] S. A. Cummer and D. Schurig, “One path to acoustic cloaking,” *New J. Phys.*, vol. 9, no. 3, p. 45, 2007.
- [12] M. D. Guild, M. R. Haberman, and A. Alù, “Plasmonic-type acoustic cloak made of a bilaminate shell,” *Phys. Rev. B*, vol. 86, no. 10, p. 104302, 2012.
- [13] V. Leroy, A. Strybulevych, M. Lanoy, F. Lemoult, A. Tourin, and J. H. Page, “Superabsorption of acoustic waves with bubble metascreens,” *Phys. Rev. B*, vol. 91, no. 2, p. 020301, 2015.

- [14] S. Koo, C. Cho, J.-h. Jeong, and N. Park, “Acoustic omni meta-atom for decoupled access to all octants of a wave parameter space,” *Nat. Commun.*, vol. 7, 2016.
- [15] Z. Liang and J. Li, “Extreme acoustic metamaterial by coiling up space,” *Phys. Rev. Lett.*, vol. 108, no. 11, p. 114301, 2012.
- [16] Y. Xie, B.-I. Popa, L. Zigoneanu, and S. A. Cummer, “Measurement of a broadband negative index with space-coiling acoustic metamaterials,” *Phys. Rev. Lett.*, vol. 110, no. 17, p. 175501, 2013.
- [17] Z. Liang, T. Feng, F. L. Shukin Lok, K. B. Ng, C. H. Chan, J. Wang, S. Han, S. Lee, and J. Li, “Space-coiling metamaterials with double negativity and conical dispersion,” *Sci. Rep.*, vol. 3, 2013.
- [18] M. R. Haberman and M. D. Guild, “Acoustic metamaterials,” *Phys. Today*, vol. 69, no. 6, pp. 42–48, 2016.
- [19] S. A. Cummer, J. Christensen, and A. Alù, “Controlling sound with acoustic metamaterials,” *Nat. Rev. Mater.*, vol. 1, p. 16001, 2016.
- [20] G. Ma and P. Sheng, “Acoustic metamaterials: From local resonances to broad horizons,” *Sci. Adv.*, vol. 2, no. 2, p. e1501595, 2016.
- [21] A. N. Norris and M. R. Haberman, “Introduction to the special issue on acoustic metamaterials,” *J. Acoust. Soc. A.*, vol. 132, no. 4, pp. 2783–2783, 2012.

- [22] X. Su, A. N. Norris, C. W. Cushing, M. R. Haberman, and P. S. Wilson, “Broadband focusing of underwater sound using a transparent pentamode lens,” *J. Acoust. Soc. A.*, vol. 141, no. 6, pp. 4408–4417, 2017.
- [23] C. L. Scandrett, J. E. Boisvert, and T. R. Howarth, “Acoustic cloaking using layered pentamode materials,” *J. Acoust. Soc. A.*, vol. 127, no. 5, pp. 2856–2864, 2010.
- [24] W. Akl and A. Baz, “Active acoustic metamaterial with simultaneously programmable density and bulk modulus,” *J. Vib. Acoust.*, vol. 135, no. 3, p. 031001, 2013.
- [25] A. Kutsenko, A. Shuvalov, O. Poncelet, and A. Darinskii, “Tunable effective constants of the one-dimensional piezoelectric phononic crystal with internal connected electrodes,” *J. Acoust. Soc. A.*, vol. 137, no. 2, pp. 606–616, 2015.
- [26] K. Bertoldi and M. C. Boyce, “Wave propagation and instabilities in monolithic and periodically structured elastomeric materials undergoing large deformations,” *Phys. Rev. B*, vol. 78, no. 18, p. 184107, 2008.
- [27] P. Wang, F. Casadei, S. Shan, J. C. Weaver, and K. Bertoldi, “Harnessing buckling to design tunable locally resonant acoustic metamaterials,” *Phys. Rev. Lett.*, vol. 113, no. 1, p. 014301, 2014.
- [28] S. G. Konarski, M. R. Haberman, and M. F. Hamilton, “Frequency-dependent behavior of media containing pre-strained nonlinear inclu-

- sions: Application to nonlinear acoustic metamaterials,” *J. Acoust. Soc. A.*, vol. 144, no. 5, pp. 3022–3035, 2018.
- [29] N. Swintek, S. Matsuo, K. Runge, J. Vasseur, P. Lucas, and P. A. Deymier, “Bulk elastic waves with unidirectional backscattering-immune topological states in a time-dependent superlattice,” *J. Appl. Phys.*, vol. 118, no. 6, p. 063103, 2015.
- [30] R. Fleury, D. L. Sounas, C. F. Sieck, M. R. Haberman, and A. Alù, “Sound isolation and giant linear nonreciprocity in a compact acoustic circulator,” *Science*, vol. 343, pp. 516–519, jan 2014.
- [31] G. Trainiti and M. Ruzzene, “Non-reciprocal elastic wave propagation in spatiotemporal periodic structures,” *New J. Phys.*, vol. 18, no. 8, p. 083047, 2016.
- [32] H. Nassar, H. Chen, A. Norris, M. Haberman, and G. Huang, “Non-reciprocal wave propagation in modulated elastic metamaterials,” *Proc. R. Soc. A*, vol. 473, no. 2202, p. 20170188, 2017.
- [33] R. Fleury, D. Sounas, M. R. Haberman, and A. Alu, “Nonreciprocal Acoustics,” *Acoustics Today*, vol. 2, no. 15, pp. 14–21, 2015.
- [34] S. A. Cummer, J. Christensen, and A. Alù, “Controlling sound with acoustic metamaterials,” *Nat. Rev. Mater.*, vol. 1, p. 16001, 2016.

- [35] F. Casadei, T. Delpero, A. Bergamini, P. Ermanni, and M. Ruzzene, “Piezoelectric resonator arrays for tunable acoustic waveguides and metamaterials,” *J. Appl. Phys.*, vol. 112, p. 064902, sep 2012.
- [36] Y. Y. Chen, G. L. Huang, and C. T. Sun, “Band gap control in an active elastic metamaterial with negative capacitance piezoelectric shunting,” *J. Vib. Acoust.*, vol. 136, p. 061008, sep 2014.
- [37] Y. Y. Chen, R. Zhu, M. V. Barnhart, and G. L. Huang, “Enhanced flexural wave sensing by adaptive gradient-index metamaterials,” *Sci. Rep.*, vol. 6, p. 35048, dec 2016.
- [38] K. Danas, S. Kankanala, and N. Triantafyllidis, “Experiments and modeling of iron-particle-filled magnetorheological elastomers,” *J. Mech. Phys. Solids*, vol. 60, pp. 120–138, jan 2012.
- [39] Y. Wang, B. Yousefzadeh, H. Chen, H. Nassar, G. Huang, and C. Daraio, “Observation of nonreciprocal wave propagation in a dynamic phononic lattice,” *Phys. Rev. Lett.*, vol. 121, p. 194301, Nov 2018.
- [40] M. S. Gockenbach, *Understanding and Implementing the Finite Element Method*. Siam, 2006.
- [41] B. R. Mace and E. Manconi, “Wave motion and dispersion phenomena: Veering, locking and strong coupling effects,” *J. Acoust. Soc. A.*, vol. 131, no. 2, pp. 1015–1028, 2012.



- [42] L. Wang and K. Bertoldi, “Mechanically tunable phononic band gaps in three-dimensional periodic elastomeric structures,” *Int. J. Solids Struct.*, vol. 49, no. 19-20, pp. 2881–2885, 2012.
- [43] D. Bruno, F. Greco, P. Lonetti, P. N. Blasi, and G. Sgambitterra, “An investigation on microscopic and macroscopic stability phenomena of composite solids with periodic microstructure,” *Int. J. Solids Struct.*, vol. 47, no. 20, pp. 2806–2824, 2010.
- [44] S. P. Wallen and M. R. Haberman, “Nonreciprocal wave phenomena in spring-mass chains with effective stiffness modulation induced by geometric nonlinearity,” *Phys. Rev. E*, vol. 99, p. 013001, Jan 2019.
- [45] J. Vila, R. K. Pal, M. Ruzzene, and G. Trainiti, “A bloch-based procedure for dispersion analysis of lattices with periodic time-varying properties,” *J. Sound Vib.*, vol. 406, pp. 363–377, 2017.
- [46] G. Renaud, S. Callé, and M. Defontaine, “Remote dynamic acoustoelastic testing: Elastic and dissipative acoustic nonlinearities measured under hydrostatic tension and compression,” *Appl. Phys. Lett.*, vol. 94, p. 011905, jan 2009.
- [47] Y. Zhang, V. Tournat, O. Abraham, O. Durand, S. Letourneur, A. Le Duff, and B. Lascoup, “Nonlinear mixing of ultrasonic coda waves with lower frequency-swept pump waves for a global detection of defects in multiple scattering media,” *J. Appl. Phys.*, vol. 113, p. 064905, feb 2013.

- [48] B. M. Goldsberry and M. R. Haberman, “Negative stiffness honeycombs as tunable elastic metamaterials,” *J. Appl. Phys.*, vol. 123, no. 9, p. 091711, 2018.
- [49] A. Amendola, A. Krushynska, C. Daraio, N. M. Pugno, and F. Fraternali, “Tuning frequency band gaps of tensegrity mass-spring chains with local and global prestress,” *Int. J. Solids Struct.*, vol. 155, pp. 47–56, 2018.
- [50] A. N. Norris and W. J. Parnell, “Hyperelastic cloaking theory: transformation elasticity with pre-stressed solids,” *Proc. R. Soc. A*, vol. 468, no. 2146, pp. 2881–2903, 2012.
- [51] P. Zhang and W. J. Parnell, “Soft phononic crystals with deformation-independent band gaps,” *Proc. R. Soc. A*, vol. 473, no. 2200, p. 20160865, 2017.
- [52] L. Airolidi and M. Ruzzene, “Design of tunable acoustic metamaterials through periodic arrays of resonant shunted piezos,” *New J. Phys.*, vol. 13, no. 11, p. 113010, 2011.
- [53] Z. Chen, C. Xue, L. Fan, S.-y. Zhang, X.-j. Li, H. Zhang, and J. Ding, “A tunable acoustic metamaterial with double-negativity driven by electromagnets,” *Sci. Rep.*, vol. 6, p. 30254, 2016.
- [54] D. M. Kochmann and K. Bertoldi, “Exploiting microstructural instabilities in solids and structures: From metamaterials to structural transitions,” *Appl. Mech. Rev.*, vol. 69, p. 050801, oct 2017.

- [55] M. J. Frazier and D. M. Kochmann, “Band gap transmission in periodic bistable mechanical systems,” *J. Sound Vib.*, vol. 388, pp. 315–326, 2017.
- [56] N. Nadkarni, A. F. Arrieta, C. Chong, D. M. Kochmann, and C. Daraio, “Unidirectional transition waves in bistable lattices,” *Phys. Rev. Lett.*, vol. 116, no. 24, p. 244501, 2016.
- [57] N. Nadkarni, C. Daraio, and D. M. Kochmann, “Dynamics of periodic mechanical structures containing bistable elastic elements: From elastic to solitary wave propagation,” *Phys. Rev. E*, vol. 90, no. 2, p. 023204, 2014.
- [58] R. K. Pal, J. Rimoli, and M. Ruzzene, “Effect of large deformation pre-loads on the wave properties of hexagonal lattices,” *Smart Mater. Struct.*, vol. 25, no. 5, p. 054010, 2016.
- [59] J. Meaud and K. Che, “Tuning elastic wave propagation in multistable architected materials,” *Int. J. Solids Struct.*, vol. 122, pp. 69–80, 2017.
- [60] P. Wang, J. Shim, and K. Bertoldi, “Effects of geometric and material nonlinearities on tunable band gaps and low-frequency directionality of phononic crystals,” *Phys. Rev. B*, vol. 88, no. 1, p. 014304, 2013.
- [61] J. Shim, P. Wang, and K. Bertoldi, “Harnessing instability-induced pattern transformation to design tunable phononic crystals,” *Int. J. Solids Struct.*, vol. 58, pp. 52–61, 2015.

- [62] H. Chen and C. T. Chan, “Acoustic cloaking and transformation acoustics,” *J. Phys. D*, vol. 43, no. 11, p. 113001, 2010.
- [63] J. W. Strutt, “Some general theorems relating to vibrations,” *P. Lond. Math Soc.*, vol. s1-4, pp. 357–368, nov 1871.
- [64] J. Achenbach, *Reciprocity in Elastodynamics*. Cambridge University Press, 2003.
- [65] H. von Helmholtz, *Theorie der Luftschwingungen in Röhren mit offenen Enden*. No. 80, W. Engelmann, 1896.
- [66] H. Lamb, “On reciprocal theorems in dynamics,” *P. Lond. Math Soc.*, vol. 1, no. 1, pp. 144–151, 1887.
- [67] A. Merkel, M. Willatzen, and J. Christensen, “Dynamic nonreciprocity in loss-compensated piezophononic media,” *Phys. Rev. Appl.*, vol. 9, p. 034033, mar 2018.
- [68] O. A. Godin, “Reciprocity and energy theorems for waves in a compressible inhomogeneous moving fluid,” *Wave Motion*, vol. 25, no. 2, pp. 143–167, 1997.
- [69] O. A. Godin, “Recovering the acoustic green’s function from ambient noise cross correlation in an inhomogeneous moving medium,” *Phys. Rev. Lett.*, vol. 97, no. 5, p. 054301, 2006.

- [70] L. M. Nash, D. Kleckner, A. Read, V. Vitelli, A. M. Turner, and W. T. M. Irvine, “Topological mechanics of gyroscopic metamaterials,” *Proc. Natl. Acad. Sci. U.S.A.*, vol. 112, pp. 14495–500, nov 2015.
- [71] P. Wang, L. Lu, and K. Bertoldi, “Topological phononic crystals with one-way elastic edge waves,” *Phys. Rev. Lett.*, vol. 115, p. 104302, 2015.
- [72] N. Boechler, G. Theocharis, and C. Daraio, “Bifurcation-based acoustic switching and rectification,” *Nat. Mater.*, vol. 10, pp. 665–668, sep 2011.
- [73] Z. Zhang, I. Koroleva, L. I. Manevitch, L. A. Bergman, and A. F. Vakakis, “Nonreciprocal acoustics and dynamics in the in-plane oscillations of a geometrically nonlinear lattice,” *Phys. Rev. E*, vol. 94, p. 032214, 2016.
- [74] J. Bunyan, K. J. Moore, A. Mojahed, M. D. Fronk, M. Leamy, S. Tawfick, and A. F. Vakakis, “Acoustic nonreciprocity in a lattice incorporating nonlinearity, asymmetry, and internal scale hierarchy: Experimental study,” *Phys. Rev. E*, vol. 97, no. 5, p. 052211, 2018.
- [75] E. Cassedy and A. Oliner, “Dispersion relations in time-space periodic media: part I—stable interactions,” *Proc. IEEE*, vol. 51, no. 10, pp. 1342–1359, 1963.
- [76] E. Cassedy, “Dispersion relations in time-space periodic media part II—unstable interactions,” *Proc. IEEE*, vol. 55, no. 7, pp. 1154–1168, 1967.

- [77] H. Nassar, H. Chen, A. N. Norris, M. R. Haberman, and G. L. Huang, “Non-reciprocal wave propagation in modulated elastic metamaterials,” *Proc. R. Soc. A*, vol. 473, p. 20170188, jun 2017.
- [78] H. Nassar, X. Xu, A. Norris, and G. Huang, “Modulated phononic crystals: Non-reciprocal wave propagation and willis materials,” *J. Mech. Phys. Solids*, vol. 101, pp. 10–29, jan 2017.
- [79] H. Nassar, H. Chen, A. N. Norris, and G. L. Huang, “Quantization of band tilting in modulated phononic crystals,” *Phys. Rev. B*, vol. 97, p. 014305, jan 2018.
- [80] D. M. Correa, T. Klatt, S. Cortes, M. Haberman, D. Kovar, and C. Seepersad, “Negative stiffness honeycombs for recoverable shock isolation,” *Rapid Prototyp. J.*, vol. 21, no. 2, pp. 193–200, 2015.
- [81] B. A. Fulcher, D. W. Shahan, M. R. Haberman, C. C. Seepersad, and P. S. Wilson, “Analytical and experimental investigation of buckled beams as negative stiffness elements for passive vibration and shock isolation systems,” *J. Vib. Acoust.*, vol. 136, no. 3, p. 031009, 2014.
- [82] D. M. Correa, C. C. Seepersad, and M. R. Haberman, “Mechanical design of negative stiffness honeycomb materials,” *Integr. Mater. Manuf. Innov.*, vol. 4, no. 1, pp. 1–11, 2015.
- [83] J. Qiu, J. H. Lang, and A. H. Slocum, “A curved-beam bistable mechanism,” *J. Microelectromech. Syst.*, vol. 13, no. 2, pp. 137–146, 2004.

- [84] A. S. Phani, J. Woodhouse, and N. Fleck, “Wave propagation in two-dimensional periodic lattices,” *J. Acoust. Soc. A.*, vol. 119, no. 4, pp. 1995–2005, 2006.
- [85] C. Kittel, *Elementary Solid State Physics: A Short Course*. Wiley, 1962.
- [86] L. Brillouin, *Wave Propagation in Periodic Structures: Electric Filters and Crystal Lattices*. Courier Corporation, 2003.
- [87] M. I. Hussein, M. J. Leamy, and M. Ruzzene, “Dynamics of phononic materials and structures: Historical origins, recent progress, and future outlook,” *Appl. Mech. Rev.*, vol. 66, no. 4, p. 040802, 2014.
- [88] S. D. Adams, R. V. Craster, and S. Guenneau, “Bloch waves in periodic multi-layered acoustic waveguides,” *Proc. R. Soc. A*, vol. 464, no. 2098, pp. 2669–2692, 2008.
- [89] E. B. Becker, G. F. Carey, and J. T. Oden, *Finite Elements, An Introduction: Volume I*. 1981.
- [90] P. Langlet, A.-C. Hladky-Hennion, and J.-N. Decarpigny, “Analysis of the propagation of plane acoustic waves in passive periodic materials using the finite element method,” *J. Acoust. Soc. A.*, vol. 98, no. 5, pp. 2792–2800, 1995.
- [91] M. I. Hussein, “Reduced bloch mode expansion for periodic media band structure calculations,” *Proc. R. Soc. A*, vol. 465, no. 2109, pp. 2825–2848, 2009.

- [92] S. Degraeve, C. Granger, B. Dubus, J.-O. Vasseur, M. Pham Thi, and A.-C. Hladky-Hennion, “Bragg band gaps tunability in an homogeneous piezoelectric rod with periodic electrical boundary conditions,” *J. Appl. Phys.*, vol. 115, no. 19, p. 194508, 2014.
- [93] P. A. Deymier, *Acoustic Metamaterials and Phononic Crystals*, vol. 173. Springer Science & Business Media, 2013.
- [94] F. Tisseur and K. Meerbergen, “The quadratic eigenvalue problem,” *SIAM Rev.*, vol. 43, no. 2, pp. 235–286, 2001.
- [95] D. Torrent, W. J. Parnell, and A. N. Norris, “Loss compensation in time-dependent elastic metamaterials,” *Phys. Rev. B*, vol. 97, no. 1, p. 014105, 2018.
- [96] H. Nassar, X. Xu, A. Norris, and G. Huang, “Modulated phononic crystals: Non-reciprocal wave propagation and willis materials,” *J. Mech. Phys. Solids*, vol. 101, pp. 10–29, 2017.
- [97] R. Fleury, D. L. Sounas, C. F. Sieck, M. R. Haberman, and A. Alù, “Sound isolation and giant linear nonreciprocity in a compact acoustic circulator,” *Science*, vol. 343, no. 6170, pp. 516–519, 2014.
- [98] M. S. Alnæs, J. Blechta, J. Hake, A. Johansson, B. Kehlet, A. Logg, C. Richardson, J. Ring, M. E. Rognes, and G. N. Wells, “The fenics project version 1.5,” *Archive of Numerical Software*, vol. 3, no. 100, 2015.



- [99] A. Logg, K.-A. Mardal, G. N. Wells, *et al.*, *Automated Solution of Differential Equations by the Finite Element Method*. Springer, 2012.
- [100] E. B. Tadmor, R. E. Miller, and R. S. Elliott, *Continuum Mechanics and Thermodynamics: From Fundamental Concepts to Governing Equations*. Cambridge University Press, 2012.
- [101] K. D. Hjelmstad, *Fundamentals of Structural Mechanics*. Springer Science & Business Media, 2007.
- [102] J. E. Roman, C. Campos, E. Romero, and A. Tomas, “SLEPc users manual,” Tech. Rep. DSIC-II/24/02 - Revision 3.10, D. Sistemes Informàtics i Computació, Universitat Politècnica de València, 2018.
- [103] S. Finnveden, “Evaluation of modal density and group velocity by a finite element method,” *J. Sound Vib.*, vol. 273, no. 1, pp. 51–75, 2004.
- [104] L.-Y. Zheng, H. Pichard, V. Tournat, G. Theocharis, and V. Gusev, “Zero-frequency and slow elastic modes in phononic monolayer granular membranes,” *Ultrasonics*, vol. 69, pp. 201–214, 2016.
- [105] R. W. Ogden, “Incremental statics and dynamics of pre-stressed elastic materials,” in *Waves in Nonlinear Pre-stressed Materials*, pp. 1–26, Springer, 2007.
- [106] V. Varadan, A. Lakhtakia, and V. Varadan, “Geometry can be the basis for acoustic activity (a la optical activity) in composite media,” *J. Wave Mater. Interact*, vol. 1, p. 315, 1986.

- [107] G. W. Milton and J. R. Willis, “On modifications of newton’s second law and linear continuum elastodynamics,” *Proc. R. Soc. A*, vol. 463, no. 2079, pp. 855–880, 2007.
- [108] M. B. Muhlestein, C. F. Sieck, P. S. Wilson, and M. R. Haberman, “Experimental evidence of willis coupling in a one-dimensional effective material element,” *Nat. Commun.*, vol. 8, 2017.
- [109] C. F. Sieck, A. Alù, and M. R. Haberman, “Origins of willis coupling and acoustic bianisotropy in acoustic metamaterials through source-driven homogenization,” *Phys. Rev. B*, vol. 96, no. 10, p. 104303, 2017.
- [110] T. P. Martin, C. N. Layman, K. M. Moore, and G. J. Orris, “Elastic shells with high-contrast material properties as acoustic metamaterial components,” *Phys. Rev. B*, vol. 85, no. 16, p. 161103, 2012.
- [111] A. S. Titovich, A. N. Norris, and M. R. Haberman, “A high transmission broadband gradient index lens using elastic shell acoustic metamaterial elements,” *J. Acoust. Soc. A.*, vol. 139, no. 6, pp. 3357–3364, 2016.
- [112] A. Marzo, A. Ghobrial, L. Cox, M. Caleap, A. Croxford, and B. Drinkwater, “Realization of compact tractor beams using acoustic delay-lines,” *Appl. Phys. Lett.*, vol. 110, no. 1, p. 014102, 2017.
- [113] G. Memoli, M. Caleap, M. Asakawa, D. R. Sahoo, B. W. Drinkwater, and S. Subramanian, “Metamaterial bricks and quantization of meta-surfaces,” *Nat. Commun.*, vol. 8, p. 14608, 2017.

- [114] G. W. Milton and A. V. Cherkhev, “Which elasticity tensors are realizable?,” *J. Eng. Mater. Tech.*, vol. 117, no. 4, pp. 483–493, 1995.
- [115] M. Kadic, T. Bückmann, N. Stenger, M. Thiel, and M. Wegener, “On the practicability of pentamode mechanical metamaterials,” *Appl. Phys. Lett.*, vol. 100, no. 19, p. 191901, 2012.
- [116] M. Kadic, T. Bückmann, R. Schittny, and M. Wegener, “On anisotropic versions of three-dimensional pentamode metamaterials,” *New J. Phys.*, vol. 15, no. 2, p. 023029, 2013.
- [117] Y. Zhang, V. Tournat, O. Abraham, O. Durand, S. Letourneur, A. Le Duff, and B. Lascoup, “Nonlinear mixing of ultrasonic coda waves with lower frequency-swept pump waves for a global detection of defects in multiple scattering media,” *J. Appl. Phys.*, vol. 113, no. 6, p. 064905, 2013.
- [118] G. Renaud, S. Callé, and M. Defontaine, “Remote dynamic acoustoelastic testing: Elastic and dissipative acoustic nonlinearities measured under hydrostatic tension and compression,” *Appl. Phys. Lett.*, vol. 94, no. 1, p. 011905, 2009.
- [119] C. Coullais, D. Sounas, and A. Alù, “Static non-reciprocity in mechanical metamaterials,” *Nature*, vol. 542, no. 7642, pp. 461–464, 2017.
- [120] S. Shan, S. H. Kang, J. R. Raney, P. Wang, L. Fang, F. Candido, J. A. Lewis, and K. Bertoldi, “Multistable architected materials for trapping

- elastic strain energy,” *Adv. Mater.*, vol. 27, no. 29, pp. 4296–4301, 2015.
- [121] D. Restrepo, N. D. Mankame, and P. D. Zavattieri, “Phase transforming cellular materials,” *Extreme Mech. Lett.*, vol. 4, pp. 52–60, 2015.
- [122] R. Lakes, “Extreme damping in composite materials with a negative stiffness phase,” *Phys. Rev. Lett.*, vol. 86, no. 13, p. 2897, 2001.
- [123] R. S. Lakes, T. Lee, A. Bersie, and Y. Wang, “Extreme damping in composite materials with negative-stiffness inclusions,” *Nature*, vol. 410, no. 6828, pp. 565–567, 2001.
- [124] T. Klatt and M. R. Haberman, “A nonlinear negative stiffness metamaterial unit cell and small-on-large multiscale material model,” *J. Appl. Phys.*, vol. 114, no. 3, p. 033503, 2013.
- [125] S. Cortes, J. Allison, C. Morris, M. Haberman, C. Seepersad, and D. Kovar, “Design, manufacture, and quasi-static testing of metallic negative stiffness structures within a polymer matrix,” *Exp. Mech.*, pp. 1–9, 2017.
- [126] R. K. Pal, M. Ruzzene, and J. J. Rimoli, “A continuum model for nonlinear lattices under large deformations,” *Int. J. Solids Struct.*, vol. 96, pp. 300–319, 2016.
- [127] M. Ruzzene, F. Scarpa, and F. Soranna, “Wave beaming effects in two-dimensional cellular structures,” *Smart Mater. Struct.*, vol. 12, no. 3, p. 363, 2003.

- [128] K. Che, C. Yuan, J. Wu, H. J. Qi, and J. Meaud, “Three-dimensional-printed multistable mechanical metamaterials with a deterministic deformation sequence,” *J. Appl. Mech.*, vol. 84, no. 1, p. 011004, 2017.
- [129] J. R. Willis, “Dynamics of composites,” in *Continuum Micromechanics*, pp. 265–290, Springer, 1997.
- [130] B. Liang, X. Guo, J. Tu, D. Zhang, and J. Cheng, “An acoustic rectifier,” *Nat. Mater.*, vol. 9, no. 12, p. 989, 2010.
- [131] N. Swintek, S. Matsuo, K. Runge, J. Vasseur, P. Lucas, and P. A. Deymier, “Bulk elastic waves with unidirectional backscattering-immune topological states in a time-dependent superlattice,” *J. Appl. Phys.*, vol. 118, no. 6, p. 063103, 2015.
- [132] R. K. Pal and M. Ruzzene, “Edge waves in plates with resonators: an elastic analogue of the quantum valley hall effect,” *New J. Phys.*, vol. 19, p. 025001, feb 2017.
- [133] K. Bertoldi, V. Vitelli, J. Christensen, and M. van Hecke, “Flexible mechanical metamaterials,” *Nat. Rev. Mater.*, vol. 2, p. 17066, oct 2017.
- [134] K. Yi, M. Collet, and S. Karkar, “Frequency conversion induced by time-space modulated media,” *Phys. Rev. B*, vol. 96, 2017.

- [135] R. K. Pal, M. Schaeffer, and M. Ruzzene, “Helical edge states and topological phase transitions in phononic systems using bi-layered lattices,” *J. Appl. Phys.*, vol. 119, p. 084305, feb 2016.
- [136] M. J. Ablowitz, *Nonlinear Dispersive Waves*. Cambridge: Cambridge University Press, 2011.
- [137] S. H. Strogatz, *Nonlinear Dynamics and Chaos : With Applications to Physics, Biology, Chemistry, and Engineering*. Cambridge: Perseus Books Publishing, LLC, may 1994.
- [138] A. H. Nayfeh and D. T. Mook, *Nonlinear Oscillations*. Wiley, 1979.
- [139] D. Torrent, O. Poncelet, and J.-C. Batsale, “Nonreciprocal thermal material by spatiotemporal modulation,” *Phys. Rev. Lett.*, vol. 120, 2018.
- [140] J. Vila, R. K. Pal, and M. Ruzzene, “Observation of topological valley modes in an elastic hexagonal lattice,” *Phys. Rev. B*, vol. 96, p. 134307, 2017.
- [141] F. Fraternali, G. Carpentieri, and A. Amendola, “On the mechanical modeling of the extreme softening/stiffening response of axially loaded tensegrity prisms,” *J. Mech. Phys. Solids*, vol. 74, pp. 136–157, jan 2015.
- [142] M. Attarzadeh, H. Al Ba’ba’a, and M. Nouh, “On the wave dispersion and non-reciprocal power flow in space-time traveling acoustic metamaterials,” *Appl. Acoust.*, vol. 133, pp. 210–214, apr 2018.

- [143] J. R. Raney and J. A. Lewis, “Printing mesoscale architectures,” *MRS Bull.*, vol. 40, pp. 943–950, nov 2015.
- [144] A. Maznev, A. Every, and O. Wright, “Reciprocity in reflection and transmission: What is a ‘phonon diode’?,” *Wave Motion*, vol. 50, no. 4, pp. 776–784, 2013.
- [145] R. Chaunsali, F. Li, and J. Yang, “Stress wave isolation by purely mechanical topological phononic crystals,” *Sci. Rep.*, vol. 6, p. 30662, nov 2016.
- [146] P. A. Deymier, V. Gole, P. Lucas, J. O. Vasseur, and K. Runge, “Tailoring phonon band structures with broken symmetry by shaping spatiotemporal modulations of stiffness in a one-dimensional elastic waveguide,” *Phys. Rev. B*, vol. 96, no. 064304, 2017.
- [147] P. A. Deymier, V. Gole, P. Lucas, J. O. Vasseur, and K. Runge, “Tailoring phonon band structures with broken symmetry by shaping spatiotemporal modulations of stiffness in a one-dimensional elastic waveguide,” *Phys. Rev. B*, vol. 96, no. 064304, 2017.
- [148] J. R. Willis, “Variational principles for dynamic problems for inhomogeneous elastic media,” *Wave Motion*, vol. 3, no. 1, pp. 1–11, 1981.
- [149] H. Nassar, Q.-C. He, and N. Auffray, “Willis elastodynamic homogenization theory revisited for periodic media,” *J. Mech. Phys. Solids*, vol. 77, pp. 158–178, 2015.

- [150] M. B. Muhlestein, C. F. Sieck, P. S. Wilson, and M. R. Haberman, “Experimental evidence of willis coupling in a one-dimensional effective material element,” *Nat. Commun.*, vol. 8, p. 15625, 2017.
- [151] M. B. Muhlestein, C. F. Sieck, A. Alù, and M. R. Haberman, “Reciprocity, passivity and causality in willis materials,” *Proc. R. Soc. A*, vol. 472, no. 2194, p. 20160604, 2016.
- [152] C. F. Sieck, A. Alù, and M. R. Haberman, “Origins of willis coupling and acoustic bianisotropy in acoustic metamaterials through source-driven homogenization,” *Phys. Rev. B*, vol. 96, no. 10, p. 104303, 2017.